THE UNIVERSITY OF CHICAGO

ENERGY BALANCE AND LAPSE RATE REGIMES IN THE MODERN CLIMATE

AND THEIR RESPONSE TO WARMING

A DISSERTATION SUBMITTED TO

THE FACULTY OF THE DIVISION OF THE PHYSICAL SCIENCES

IN CANDIDACY FOR THE DEGREE OF

DOCTOR OF PHILOSOPHY

DEPARTMENT OF THE GEOPHYSICAL SCIENCES

BY

OSAMU MIYAWAKI

CHICAGO, ILLINOIS

DECEMBER 2022

"Concision in style, precision in thought, decision in life."

— Victor Hugo

Table of Contents

iv

List of Figures

xv

List of Tables

ACKNOWLEDGMENTS

ABSTRACT

In response to anthropogenic forcing, climate models project tropical amplification of warming aloft and Arctic amplification of surface warming. The vertical and latitudinal structure of warming has important implications for the response of tropical and extratropical storms and the mean circulation to climate change. While previous studies have shown that key features of the tropical and polar warming response can be qualitatively understood from simple column models of temperature, namely Radiative-Convective Equilibrium (RCE) and Radiative-Advective Equilibrium (RAE) in the tropics and poles, we currently do not have a complete quantitative understanding of the spatio-temporal structure of RCE and RAE (energy balance regimes) and their connection to the vertical structure of warming (lapse rate regimes). Improving our understanding by linking theory and models of varying complexity increases our confidence in climate change projections, which exhibit structural and parameter uncertainty.

In this thesis, I contribute to our understanding of Earth's vertical and latitudinal temperature structure and its response to anthropogenic forcing. I use theory to define energy balance regimes and show that they provide a useful guide for the vertical warming response projected by state-of-the-art climate models. I use idealized models to show that surface heat capacity controls RCE in the midlatitudes and sea ice controls RAE in the polar regions in the modern climate. Quantitatively, however, the RCE warming response (moist adiabatic adjustment) overpredicts the amplification of tropical warming aloft. I quantify the contribution of mechanisms not included in the moist adiabat (surface heterogeneity, the direct CO_2 effect, and convective entrainment) on this overprediction. Finally, I show a new energy balance regime emerges in the Arctic by the year 2100, coinciding with the emergence of convective activity, vanishing surface inversion, and melting sea ice. Together the results improve our understanding of and confidence in the warming response projected by comprehensive climate model projections.

CHAPTER 1

INTRODUCTION

State-of-the-art general circulation models (GCMs) robustly project that the tropospheric warming response to anthropogenic forcing is amplified aloft in the tropics and amplified at the surface in the Arctic (Manabe and Wetherald, 1975; Held, 1993; Vallis et al., 2015). Understanding the vertical and latitudinal temperature structure of Earth's atmosphere and its response to climate change has important implications for our understanding of climate. For example, the vertical and latitudinal gradients of atmospheric temperature impact theories of convective instability (Singh and O'Gorman, 2013; Seeley and Romps, 2015), mean circulation (Held and Hou, 1980; Held, 2000; Schneider, 2006), and baroclinic instability (Chang et al., 2002; Shaw et al., 2016). The magnitude of surface warming in response to anthropogenic forcing depends on the vertical structure of atmospheric warming through the lapse rate feedback (Popke et al., 2013; Po-Chedley et al., 2018).

State-of-the-art GCMs are designed to capture the full complexity of the real world. The inclusion of detailed processes of the whole Earth system makes GCMs valuable for quantitative projections and identifying the emergence of robust responses to climate change. This inherent complexity along with structural and parameter uncertainty also makes comprehensive GCMs a difficult tool to build our physical understanding of climate. Thus, we build understanding by reducing the model complexity to include only the essential ingredients necessary to explain the phenomenon of interest (Held, 2005).

The simplest model for studying Earth's vertical temperature structure and its response to radiative forcings was introduced by the pioneering work of Manabe and Strickler (1964). In their model, the temperature profile of a single atmospheric column is influenced by radiative and convective heat fluxes. The effect of convection is parameterized by a hard adjustment of unstable lapse rates to one that is neutrally stable to convection. The column-integrated energy budget is thus maintained by a balance between radiative cooling and convective heating, so-called Radiative-Convective Equilibrium (RCE).

RCE is an excellent model for the global mean temperature structure because the advective heat flux exactly integrates to zero in the global mean. However, its usefulness is limited by the infeasibility of deriving a globally-averaged convective lapse rate from first principles because deep convection does not occur everywhere on Earth. The dynamics that influence the vertical temperature profile vary significantly as a function of latitude (vertical mixing by deep convection in the tropics to isentropic mixing by baroclinic eddies in the extratropics).

This motivated an extension of the column energy balance framework as a tool for understanding the temperature profile not just for the global mean. Specifically, RCE has become a common assumption for tropical energy balance, including its application to theory (Emanuel and Bister, 1996; Nilsson and Emanuel, 1999; Romps et al., 2014; Singh and O'Gorman, 2015) and idealized models (Wing et al., 2018b). In the tropics, where the dynamics are dominated by deep convection, a convectively neutral lapse rate can be derived analytically, the simplest of which being the moist adiabat. Key features of the tropical stratification and its response to anthropogenic forcing are captured by moist adiabatic adjustment, namely the amplified warming in the upper troposphere in response to anthropogenic forcing (Held, 1993).

In the polar regions, the column energy budget is maintained by a balance between radiative cooling and advective heating from lower latitudes (Nakamura and Oort, 1988), so-called Radiative-Advective Equilibrium (RAE, Cronin and Jansen, 2016). By combining the two-stream Schwarzchild equation for gray radiative transfer with an advective heating profile that assumes a power law vertical structure, Cronin and Jansen (2016) derived an analytic model for the temperature profile of a column in RAE. RAE temperature profiles exhibit key features of the observed temperature profile in Earth's polar regions including a strong surface inversion and a surface amplified warming response to radiative forcing (Payne et al., 2015). Thus, energy balance regimes (RCE and RAE) provide a promising framework to develop our understanding of the maintenance of Earth's temperature structure (lapse rate regimes) in the modern climate and its response to climate change.

However, few studies to date have quantified the spatio-temporal structure of energy balance regimes in the modern climate and its response to anthropogenic forcing. Jakob et al. (2019) investigated the spatial and temporal scales where RCE is valid in the tropics. However, the seasonal and latitudinal structure of RCE and energy balance regimes in general (i.e. RCE and RAE) have not been investigated. Quantifying the spatio-temporal structure of energy balance regimes is important to precisely define where and when RCE and RAE, including their implications for the warming response, are expected to apply. Additionally, the link between energy balance and lapse rate regimes has not been investigated using state-of-the-art reanalyses or GCMs. Quantitatively demonstrating that this link holds through the hierarchy of model complexity is important to establish the robustness and usefulness of the energy balance framework for understanding Earth's temperature structure.

In this thesis, I combine theory and models of varying complexity to improve our understanding of Earth's warming response to anthropogenic forcing. I introduce a new metric to quantitatively test the usefulness of theory (energy balance regimes) for understanding climate model warming projections. I use idealized models to test mechanisms that control energy balance regime transitions through the seasonal cycle and in response to anthropogenic forcing.

In Chapter 2, I introduce a nondimensional number R_1 that quantifies energy balance regimes using the moist static energy budget framework. I use R_1 to quantify the latitudinal structure and seasonal cycle of energy balance and lapse rate regimes in the modern climate and their response to anthropogenic forcing. I show that surface heat capacity and sea ice control the existence of seasonal energy balance regime transitions in the Northern Hemisphere midlatitudes and high latitudes, respectively. The work presented in this chapter is published in Miyawaki et al. (2022).

In Chapter 3, I test the quantitative link between RCE and the convective lapse rate regime in the tropics. The link implies the upper troposphere amplified warming response to anthropogenic forcing can be understood as a moist adiabatic adjustment to a warmer

surface temperature. I assess how well moist adiabatic adjustment predicts the tropical warming response in state-of-the-art GCMs. I quantify the contribution of processes not included in moist adiabat adjustment — surface heterogeneity, the direct effect of CO_2, and convective entrainment — on the discrepancy between the warming response predicted by moist adiabatic adjustment and projected from GCMs. The work presented in this chapter is published in Miyawaki et al. (2020).

In Chapter 4, I show that Arctic climate change under anthropogenic forcing is associated with an energy balance regime transition from RAE in the modern climate to one where convective heating is important in the future climate. I show sea-ice melting is the key mechanism that controls the existence of the regime transition. I identify implications of the energy balance regime transition on the emergence of convective precipitation.

Lastly, I conclude and discuss the scientific and broader impacts of this research in Chapter 5.

CHAPTER 2

QUANTIFYING ENERGY BALANCE REGIMES IN THE MODERN CLIMATE, THEIR LINK TO LAPSE RATE REGIMES, AND THEIR RESPONSE TO WARMING

2.1 Introduction

Earth's modern climate is maintained by three types of energy transfer: advection, radiation, and surface turbulent fluxes (e.g., see Ch. 6.2 in Hartmann, 2016). These energy transfer types can be most easily defined using the vertically-integrated, zonal-mean, annual-mean moist static energy (MSE) budget:

$$\underbrace{\langle \partial_y \overline{[vm]} \rangle}_{\text{advection}} = \underbrace{\overline{[R_a]}}_{\text{radiation}} + \underbrace{\overline{[\text{LH}]} + \overline{[\text{SH}]}}_{\text{surface turbulence}} , \tag{2.1}$$

where $m = c_p T + gz + Lq$ is MSE, $\overline{(\cdot)}$ is the annual mean, $[\cdot]$ is the zonal mean, and $\langle \cdot \rangle$ is the mass-weighted vertical integral (Neelin and Held, 1987). Advection corresponds to the meridional divergence $(\partial_y(\cdot) \equiv \frac{1}{r \cos \phi} \partial_\phi ((\cdot) \cos \phi)$ is the meridional divergence in spherical coordinates, where ϕ is latitude and r is the radius of Earth) of MSE flux (vm where v is meridional velocity) and represents the energy transported by the atmospheric circulation, such as the Hadley cell and storm tracks. Radiation (R_a) corresponds to atmospheric radiative cooling, which is the difference of the top-of-atmosphere and surface radiative fluxes. Finally, surface turbulent fluxes correspond to surface latent (LH) and sensible (SH) heat flux.

In the annual mean, the dominant types of energy transfer depend on latitude (e.g., see Fig. 6.1 in Hartmann, 2016). In the low latitudes, atmospheric radiative cooling is primarily balanced by surface turbulent fluxes (Riehl and Malkus, 1958), which destabilize

---

The content of this chapter is published in Miyawaki et al. (2022). Tiffany A. Shaw and Malte F. Jansen contributed as co-authors of this chapter. © American Meteorological Society. Used with permission.

the column to convection by supplying moist, warm air to the boundary layer. The dominant balance between radiative cooling and surface turbulent fluxes is consistent with Radiative-Convective Equilibrium (RCE, Wing et al., 2018b). In the high latitudes, atmospheric radiative cooling is primarily balanced by advection from lower latitudes (Nakamura and Oort, 1988) consistent with Radiative-Advective Equilibrium (RAE, Cronin and Jansen, 2016). Finally in the midlatitudes, all three types of energy transfer are important; thus, I introduce the term Radiative-Convective-Advective Equilibrium (RCAE). In this way, three energy balance regimes qualitatively characterize the low, mid, and high latitude regions of Earth's modern climate.

Annual mean lapse rate regimes also qualitatively characterize the low, mid, and high latitude regions of Earth's modern climate. The low latitudes exhibit a moist adiabatic lapse rate regime (Stone and Carlson, 1979; Betts, 1982; Xu and Emanuel, 1989; Williams and Renno, 1993; Korty and Schneider, 2007). The high latitudes exhibit a surface inversion lapse rate regime (e.g., see Fig. 1.3 in Hartmann, 2016). Finally, the midlatitudes are a mixed regime, which is more stable than a moist adiabat (Stone and Carlson, 1979; Korty and Schneider, 2007) with no surface inversion.

The lapse rate regime varies through the seasonal cycle in the Northern Hemisphere. For example, the midlatitudes exhibit a moist adiabatic regime in summer and a mixed regime in winter (Stone and Carlson, 1979; Korty and Schneider, 2007). The Northern Hemisphere high latitudes exhibit a mixed regime in summer and a surface inversion regime in winter (Bradley et al., 1992; Tjernström and Graversen, 2009; Devasthale et al., 2010; Zhang and Stone, 2011; Cronin and Jansen, 2016).

While energy balance and lapse rate regimes qualitatively characterize the low, mid, and high latitudes of Earth's modern climate, few studies to date have quantified the latitudinal and seasonal dependence of observed energy balance regimes and their link to lapse rate regimes in reanalyses and general circulation models (GCMs).

Quantifying the latitudinal and seasonal dependence of observed energy balance regimes

would allow us to assess where and when idealized models that assume RCE or RAE hold. This would be useful for several reasons. First, the results of many studies investigating the tropical climate (precipitation, cloud, and circulation) and its response to warming use models that assume RCE (e.g., Romps, 2011; Popke et al., 2013; Pendergrass et al., 2016; Merlis and Held, 2019). Quantifying the latitudinal and seasonal dependence of RCE in the modern climate can guide where and when these insights are applicable. Jakob et al. (2019) took a first step in this direction by quantifying the spatial and temporal scales that satisfy RCE in the tropics. However, they did not examine the possible occurrence of RCE outside of the tropics or energy balance regimes more generally (RAE and RCAE).

Second, knowledge of energy balance regimes for the modern climate could provide a useful guide for interpreting the vertical structure of the warming response latitudinally and seasonally. For regions that are in RCE in the modern climate and remain in RCE in the future, the expectation is that warming maximizes aloft (Held, 1993; Romps, 2011). For regions that are in RAE in the modern climate and remain in RAE in the future, the expectation is that warming maximizes at the surface (assuming that the radiative forcing dominates over changes in surface or advective heat flux, Held, 1993; Cronin and Jansen, 2016). However, it is an open question whether energy balance regimes in the modern climate provide a useful guide to the vertical structure of the warming response latitudinally and seasonally.

Here I seek to answer the following questions. Where and when do energy balance regimes (RCE, RAE, and RCAE) occur in Earth's modern climate? How closely are they linked to lapse rate regimes (moist adiabatic, surface inversion, and mixed)? Do energy balance regimes in the modern climate provide a useful guide for interpreting the vertical structure of the warming response? To answer these questions, I develop a nondimensional number based on the MSE budget to quantify energy balance regimes (Section 2.2.1). I use this nondimensional number to quantify where and when energy balance regimes occur latitudinally and seasonally in Earth's modern climate using reanalysis and Coupled Model

Intercomparison Project Phase 5 (CMIP5) data. I quantify the connection between energy balance and lapse rate regimes (Section 2.3) and use idealized climate models to formulate and test hypotheses that explain the seasonality of energy balance regime transitions in the Northern Hemisphere (Section 2.4). Finally, I investigate whether energy balance regimes in the modern climate are a useful guide to the vertical structure of the warming response in CMIP5 models (Section 2.5). The results are summarized and discussed in Section 2.6.

2.2   Methods

2.2.1   Defining energy balance regimes using the nondimensionalized MSE budget

In order to define energy balance regimes seasonally, I begin with the vertically-integrated, zonal-mean MSE equation:

$$\langle [\partial_t m] \rangle + \langle \partial_y [vm] \rangle = [R_a] + [\text{LH}] + [\text{SH}] , \tag{2.2}$$

where $\langle [\partial_t m] \rangle$ represents atmospheric MSE storage. In order to nondimensionalize equation (2.2), I divide by radiative cooling R_a, which is sign definite for the modern climate:

$$\underbrace{\frac{\partial_t m + \partial_y(vm)}{R_a}}_{R_1} = 1 + \underbrace{\frac{\text{LH} + \text{SH}}{R_a}}_{R_2} , \tag{2.3}$$

where R_1 and R_2 are nondimensional numbers and the $[\cdot]$ and $\langle \cdot \rangle$ have been dropped for brevity.

In the strictest sense, RCE is a steady-state equilibrium where radiation balances surface turbulent fluxes $(R_1 = 0)$. As this is exactly satisfied only in the global mean, I define RCE as $R_1 \leq \varepsilon$, where ε is a small number. This definition includes regions of vertically-integrated MSE flux divergence $(R_1 < 0$, where convective heating is balanced by both radiative and

advective cooling) and weak convergence ($0 < R_1 \leq \varepsilon$) because temperature profiles in regions of divergence are set by convective adjustment (Warren et al., 2020).

RAE as defined in Cronin and Jansen (2016) requires surface turbulent fluxes to be negligibly small ($R_2 = 0$ or equivalently $R_1 = 1$). Although exact RAE further requires atmospheric storage to be small ($\partial_t m = 0$), the framework developed by Cronin and Jansen (2016) could readily be generalized to account for the time tendency term, which would add to the advective tendency. To be consistent with the definition of RCE, I define RAE as regions where surface turbulent fluxes are small or directed from the atmosphere to the surface ($R_2 \geq -\varepsilon$ or equivalently $R_1 \geq 1 - \varepsilon$).

In order to choose the value for ε, I examine the deviation of the zonal-mean, annual-mean lapse rate from the moist adiabatic lapse rate binned by the value of R_1 using reanalysis data (Fig. 2.1). The lapse rate deviation is plotted in sigma coordinates to ensure that surface inversions are properly represented (see Appendix 2.A for more details). The tropospheric lapse rate deviation is nearly a monotonic function of R_1 (especially above $\sigma = 0.7$ and below $\sigma = 0.9$), demonstrating the quantitative link between energy balance and lapse rate regimes. The surface inversion lapse rate regime occurs for $R_1 \geq 0.9$ and thus I define the RAE regime as $R_1 \geq 1 - \epsilon = 0.9$ (thick blue line, Fig. 2.1). Consistently, I define the RCE regime as $R_1 \leq \varepsilon = 0.1$. Where $R_1 \leq 0.1$, the free tropospheric lapse rate (vertically averaged from $\sigma = 0.7$ to 0.3) is in the moist adiabatic lapse rate regime (i.e., it deviates from the moist adiabatic lapse rate by less than 13%, thick orange line in Fig. 2.1). Finally, I define the RCAE regime as where $0.1 < R_1 < 0.9$, where it corresponds to the mixed lapse rate regime (i.e., $> 13\%$ more stable than a moist adiabatic lapse rate but does not exhibit a surface inversion).

2.2.2   Reanalysis data

I consider three reanalysis datasets from 1980 through 2005: ERA5 (Hersbach et al., 2020), MERRA2 (Gelaro et al., 2017), and JRA55 (Kobayashi et al., 2015). I focus on the energy
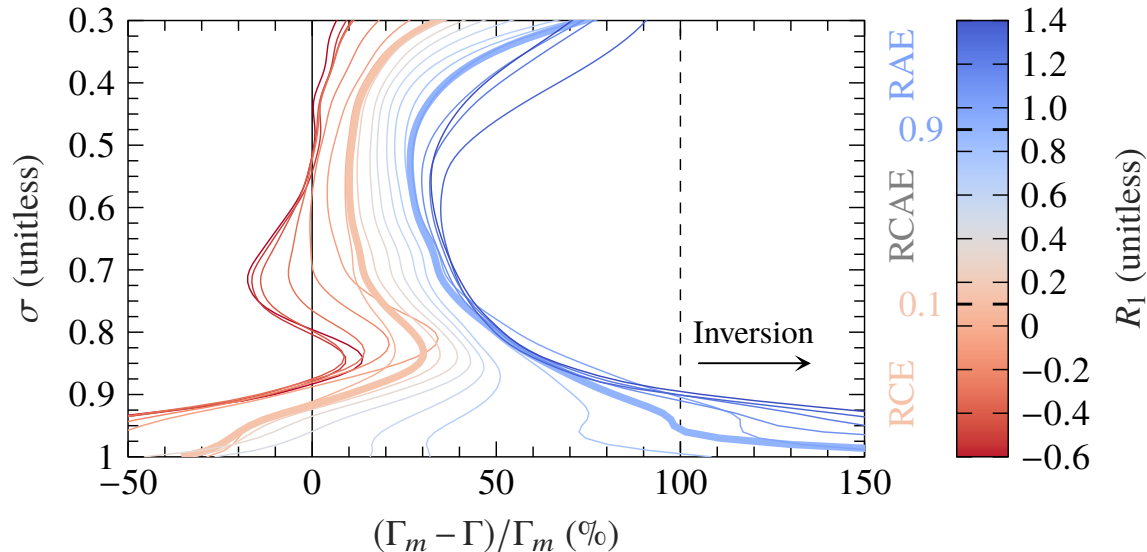
Figure 2.1: The zonal-mean, annual-mean percent deviation of the lapse rate from the moist adiabatic lapse rate binned by R_1 (bin widths are 0.1) for the reanalysis mean. Thick blue and orange lines correspond to $R_1 = 0.9$ and $R_1 = 0.1$, respectively. A 100% deviation from the moist adiabat denotes an isothermal atmosphere and hence marks the threshold for an inversion.

balance and lapse rate regimes for the multi-reanalysis mean and show the spread as the range across the three reanalyses. Atmospheric storage ($\partial_t m$) is computed by taking the finite difference of MSE using monthly temperature, specific humidity, and geopotential data, following Donohoe and Battisti (2013). Additionally, I use the monthly radiative (R_a) and surface turbulent (LH and SH) fluxes and infer the advective flux ($\partial_y(vm)$) as the residual. I choose to infer advection as the residual because the mass-correction technique for directly computing the MSE flux divergence in reanalysis data is known to produce unphysical results in the high latitudes (Porter et al., 2010).

2.2.3   CMIP5 simulations

I consider the r1i1p1 historical simulation averaged over 1980 through 2005 and the r1i1p1 RCP8.5 simulation averaged over 2070 through 2099 for 36 CMIP5 models (Table 2.B.2, Taylor et al., 2012). I show the energy balance and lapse rate regimes for the multimodel

mean and show the spread as the interquartile range across the models. Consistent with the reanalysis products, I compute R_1 using monthly $\partial_t m$, R_a, LH, and SH, and infer $\partial_y(vm)$ as the residual.

2.2.4   Idealized climate models

I use two idealized climate models to understand the seasonal changes in energy balance regimes. At intermediate complexity, I examine seasonal changes in the ECHAM6 slab ocean aquaplanet model (Stevens et al., 2013), hereafter referred to as AQUA. AQUA simulations are configured with a seasonal cycle, no ocean heat transport, modern greenhouse gas concentrations, and with or without thermodynamic sea ice following Shaw and Graham (2020).

Thermodynamic sea ice in AQUA is based on the zero-layer Semtner model (Semtner, 1976). Sea-ice fraction in a grid box is either entirely covered in sea ice (100% concentration) or is open ocean (0% concentration). The surface albedo over an open ocean is 0.07. The surface albedo over sea ice varies between 0.55–0.80 as a function of temperature and snow depth. Additional details of the thermodynamic sea ice model in ECHAM6 are provided in Giorgetta et al. (2013).

In order to explore the seasonal variation in energy balance regimes, I vary the mixed layer depth in AQUA from 3 to 50 m without sea ice and 25 to 50 m with sea ice following previous work (Donohoe et al., 2014; Barpanda and Shaw, 2020; Shaw and Graham, 2020). Shaw and Graham (2020) showed that AQUA enters a Snowball Earth regime for mixed layer depths below 20 m; hence, 25 m is the minimum mixed layer depth for AQUA with ice considered here. A monthly climatology is obtained by averaging the last 20 years of the 40 year simulation except for the 3 m configuration, where the last 5 years of a 15 year simulation are averaged due to the faster equilibration. Consistent with the reanalysis products and the CMIP5 simulations, I compute R_1 using the monthly $\partial_t m$, R_a, LH, and SH, and infer $\partial_y(vm)$ as the residual.

At the simple end, I use the EBM of Rose et al. (2017). The EBM is an equation for the zonal-mean surface temperature:

$$\rho c_w d \, \partial_t T_s = aQ - (A + BT_s) + \frac{D}{\cos\phi} \partial_\phi \left(\partial_\phi T_s \, \cos\phi \right) , \qquad (2.4)$$

where ρ is the density of water, c_w is the specific heat capacity of liquid water, d is the mixed layer depth, T_s is the zonal-mean surface temperature, a is the co-albedo, Q is insolation, $A + BT_s$ is outgoing longwave radiation where A and B are constant coefficients, ϕ is latitude, and D is the diffusivity, which is assumed to be a constant. I set $A = -410$ W m^{-2}, $B = 2.33$ W m^{-2} K^{-1}, $D = 0.90$ W m^{-2} K^{-1}, and $a = 0.72$, which are obtained from best fits to AQUA configured with a 25 m mixed layer depth and without sea ice. Best fits of A and B are obtained by taking the least squares linear regression of the zonal-mean OLR and T_s. The best fit of D is obtained similarly by taking the least squares linear regression of $\partial_y (vm)$ and $\frac{1}{\cos\phi} \partial_\phi \left(\partial_\phi T_s \, \cos\phi \right)$ for latitudes poleward of 25°. Lastly, a is computed as the globally-averaged diagnosed planetary co-albedo.

2.3 Energy balance regimes in reanalysis data

2.3.1 Annual-mean energy balance regimes

In the annual mean, the RCE regime, defined by $R_1 \leq 0.1$, extends from the deep tropics to $\approx 40°$ (black line overlapping orange region in Fig. 2.2a). The moist adiabatic lapse rate regime occurs in the same region. In particular, the free tropospheric lapse rate, defined as the vertically-averaged lapse rate from $\sigma = 0.7$ to 0.3, closely follows R_1 (compare orange and black lines in Fig. 2.2a) and deviates -3% to $+13\%$ from a moist adiabat where $R_1 \leq 0.1$.

The RAE regime, defined by $R_1 \geq 0.9$, occurs poleward of $\approx 80°$N and $\approx 70°$S in the annual mean (black line overlapping blue region in Fig. 2.2b). The reanalysis spread in the high latitudes is large in both hemispheres due to high uncertainty in the estimation of

surface turbulent fluxes (Tastula et al., 2013; Graham et al., 2019). The largest values of R_1 are found over Antarctica whereas R_1 is close to the RCAE threshold in the Arctic. The RAE regime coincides with a surface inversion lapse rate regime. Specifically, the region where $R_1 \geq 0.9$ exhibits $> 100\%$ deviation from a moist adiabat indicating a surface inversion (blue line in Fig. 2.2b).

Lastly, the RCAE regime, defined by $0.1 < R_1 < 0.9$, occurs between 40 to 80°N and 40 to 70°S in the annual mean (black line overlapping the white region in Fig. 2.2a). The RCAE regime coincides with the mixed lapse rate regime, where the lapse rate is more stable than a moist adiabat and does not exhibit a surface inversion. Specifically, the free tropospheric lapse rate in the region where $0.1 < R_1 < 0.9$ deviates $+13\%$ to $+35\%$ from a moist adiabat.

2.3.2 Seasonality of energy balance regimes

The seasonality of R_1 is weak in the Southern Hemisphere, such that the latitudinal extent of RCE (equatorward of 40°S), RAE (poleward of 70°S), and RCAE regimes (between 40 to 70°S) is largely the same throughout the year (Fig. 2.3a). Consistently, the midlatitudes exhibit a mixed lapse rate regime (Fig. 2.3b) and the high latitudes exhibit a surface inversion year round (Fig. 2.3c).

In the Northern Hemisphere, the RCE regime occurs year round equatorward of 40°N and expands poleward to 70°N during June (region equatorward of the thick orange contour in Fig. 2.3a). The seasonality of the moist adiabatic lapse rate regime similiarly expands poleward during summertime (e.g., see the 15% deviation contour in Fig. 2.3b). However, there is a phase shift between the seasonality of energy balance and lapse rate regimes in the midlatitudes. The Northern midlatitudes are in the RCE regime from April to July but in the moist adiabatic lapse rate regime from June to September (compare solid black and orange lines in Fig. 2.4a). This lag is associated with the seasonality of atmospheric storage. When atmospheric storage is excluded from R_1, there is closer agreement in the phase of the energy balance and lapse rate seasonality (compare dashed black and orange lines in
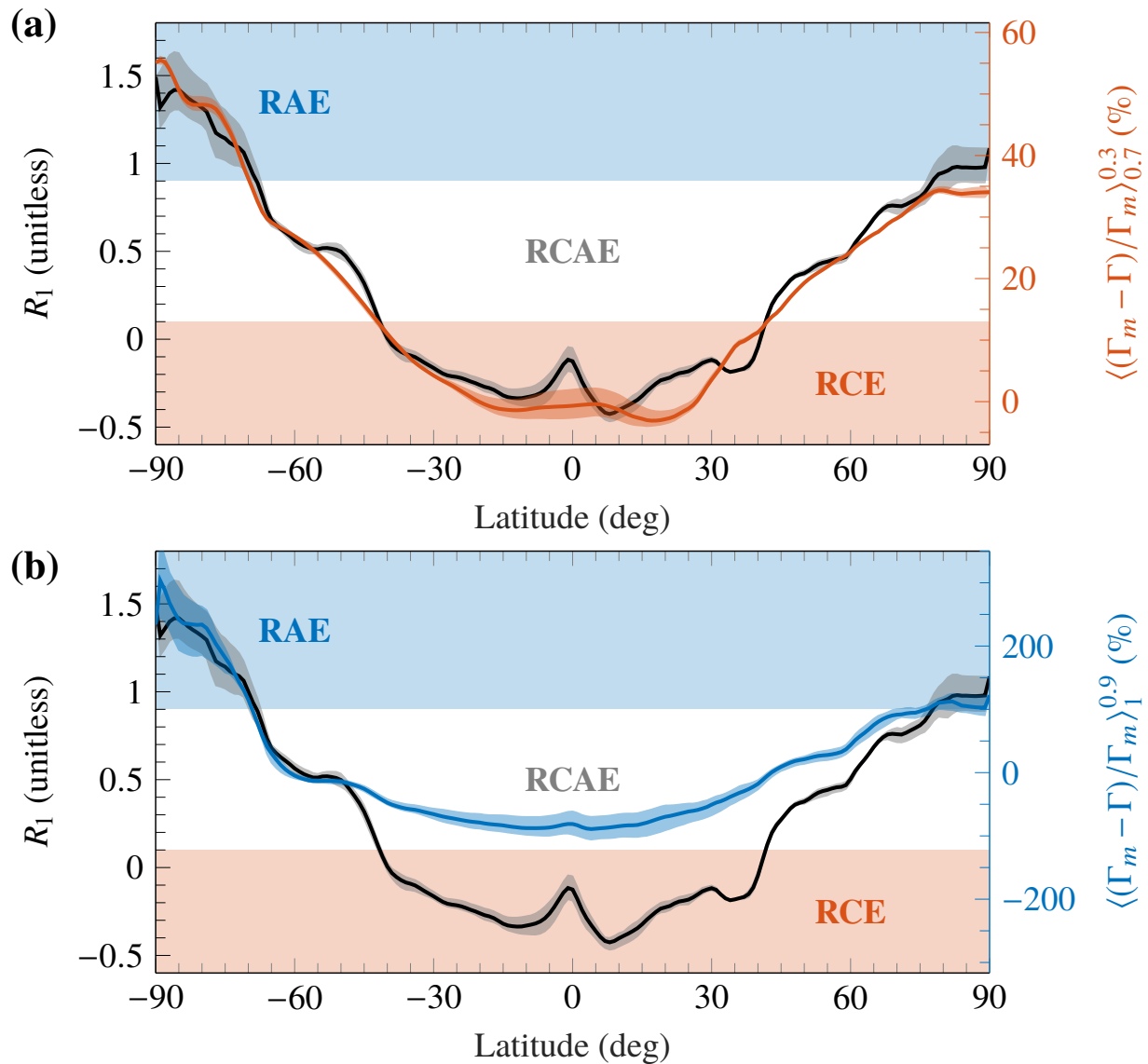
Figure 2.2: (a) The zonal-mean, annual-mean structure of R_1 (black line, left axis) and the vertically-averaged free tropospheric ($\sigma = 0.7$ to 0.3) lapse rate deviation from the moist adiabatic lapse rate (orange line, right axis) for the reanalysis mean. Orange, white, and blue regions indicate RCE, RCAE, and RAE, respectively. (b) The zonal-mean, annual-mean structure of R_1 (black line, left axis) and the vertically-averaged boundary layer ($\sigma = 1$ to 0.9) lapse rate deviation from the moist adiabatic lapse rate (blue line, right axis) for the reanalysis mean. The shading over the lines indicates the range across the reanalyses.
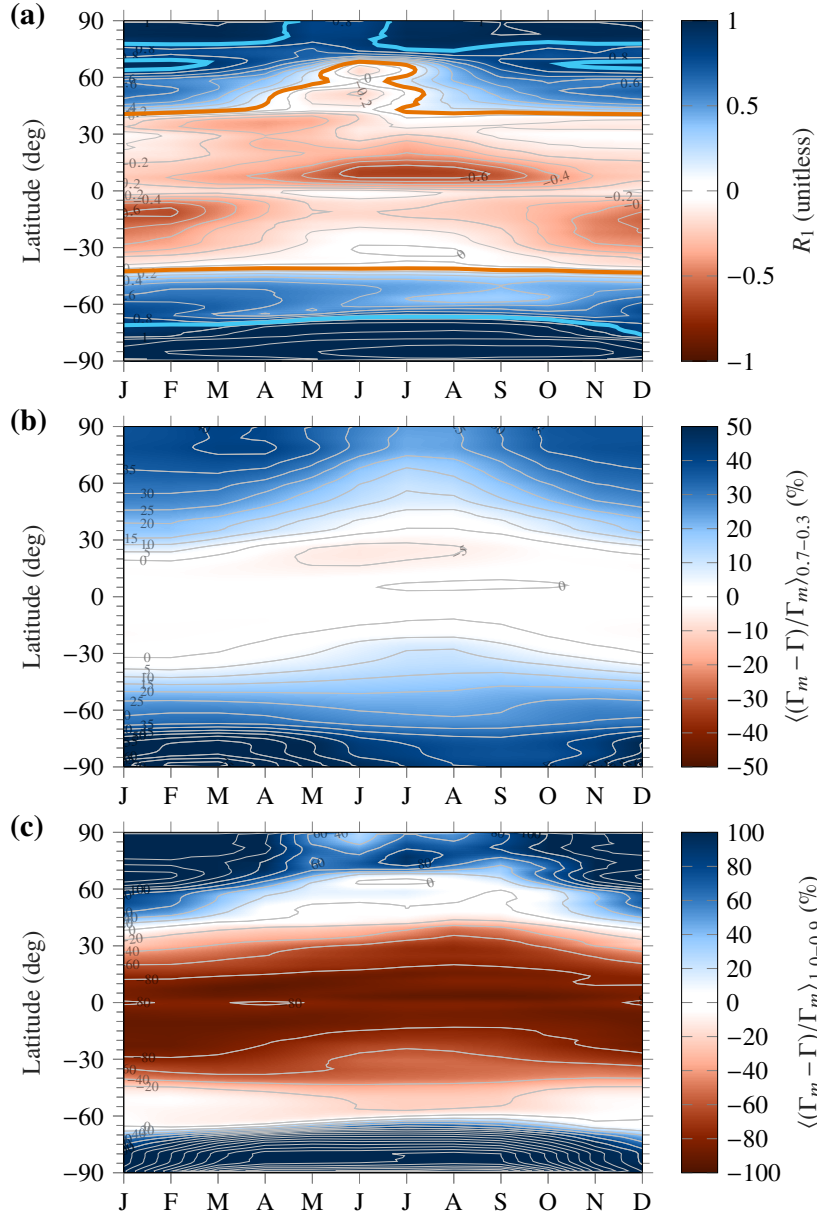
Figure 2.3: (a) The seasonality of R_1 (contour interval is 0.1) for the reanalysis mean. The thick orange contour indicates the RCE/RCAE boundary ($R_1 = 0.1$) and the thick blue contour indicates the RAE/RCAE boundary ($R_1 = 0.9$). (b) The spatio-temporal structure of the free tropospheric (vertically averaged from $\sigma = 0.7$ to 0.3) lapse rate deviation from a moist adiabat for the reanalysis mean (contour interval is 5%). (c) The spatio-temporal structure of the boundary layer (vertically averaged from $\sigma = 1$ to 0.9) lapse rate deviation from the moist adiabatic lapse rate for the reanalysis mean (contour interval is 20%).

(a) Northern Hemisphere Midlatitudes

(b) Northern Hemisphere High Latitudes

Legend:
$$\frac{\partial_t m + \partial_y(vm)}{R_a} \qquad \frac{\partial_y(vm)}{R_a}$$
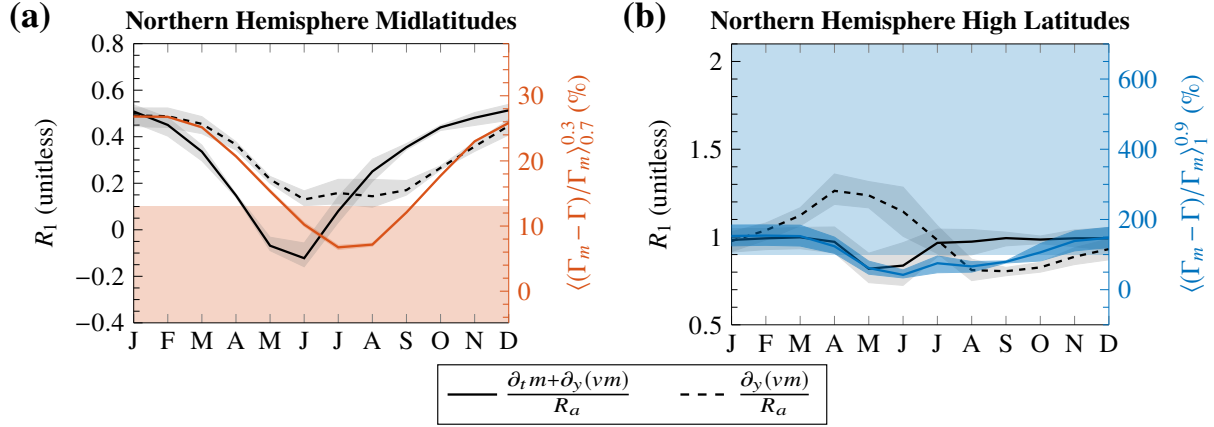
Figure 2.4: The seasonality of R_1 with (solid black) and without (dashed black) atmospheric storage is compared to the lapse rate seasonality in the free troposphere (orange line) and near the surface (blue line) for the Northern Hemisphere (a) midlatitudes (40 to 60°N) and (b) high latitudes (80 to 90°N) for the reanalysis mean. The shading over the lines indicates the range across the reanalyses. The orange and blue regions indicate RCE and RAE regimes, respectively.

Fig. 2.4a).

The Northern Hemisphere RAE regime occurs poleward of 80°N with the exception of May and June (region poleward of the thick blue contour in Fig. 2.3a). Consistently, the mixed lapse rate regime occurs during May and June (Fig. 2.3c), but persists through September despite being in a state of RAE (compare solid black and blue lines in Fig. 2.4b). The atmospheric storage term again plays an important role in the seasonal atmospheric MSE budget (compare solid and dashed black lines in Fig. 2.4b). However, unlike in the midlatitudes, the discrepancy in the timing of the energy balance and lapse rate regimes in the high latitudes cannot be directly related to the seasonality of atmospheric storage (compare dashed black and blue lines in Fig. 2.4b).

16

2.3.3   Decomposition of seasonal energy balance regime transitions

In order to diagnose the physical mechanisms responsible for the seasonal energy balance regime transitions in the Northern Hemisphere, I decompose the seasonality of R_1 as follows:

$$\Delta R_1 = \overline{R_1} \left(\frac{\Delta(\partial_t m + \partial_y(vm))}{\overline{\partial_t m + \partial_y(vm)}} - \frac{\Delta R_a}{\overline{R_a}} \right) + \text{Residual} , \qquad (2.5)$$

where $\Delta(\cdot)$ is the deviation from the annual mean and $\overline{(\cdot)}$ is the annual mean. The advective component [first term on the right hand side of equation (2.5)] quantifies the importance of advection plus atmospheric storage, and the radiative component [second term on the right hand side of equation (2.5)] quantifies the importance of radiative cooling. Lastly, the residual quantifies the importance of higher-order terms.

The RCAE to RCE regime transition in the Northern midlatitudes (where the solid black line intersects the orange region in Fig. 2.5a) closely follows the advective component (compare black and red lines in Fig. 2.5a) whereas the other terms are small (gray and dash-dot line in Fig. 2.5a). The RCE regime corresponds to the time when advection plus atmospheric storage are small (sum of black and red lines in Fig. 2.5b). In the Southern Hemisphere, the advective and radiative components are of similar magnitude and partially compensate, leading to relatively small seasonality in R_1 (Fig. 2.5c). The radiative components are similar between the two hemispheres (compare gray lines in Fig. 2.5a and 2.5c). Thus, there is no midlatitude regime transition to RCE in the Southern Hemisphere because the advective component is small, which is consistent with the small seasonality of advection plus storage (black and red lines in Fig. 2.5d).

The RAE to RCAE regime transition in the Northern high latitudes is the outcome of opposing advective and radiative components (Fig. 2.6a). Since $\overline{R_1} = \overline{\partial_t m + \partial_y(vm)}/\overline{R_a} \approx 1$
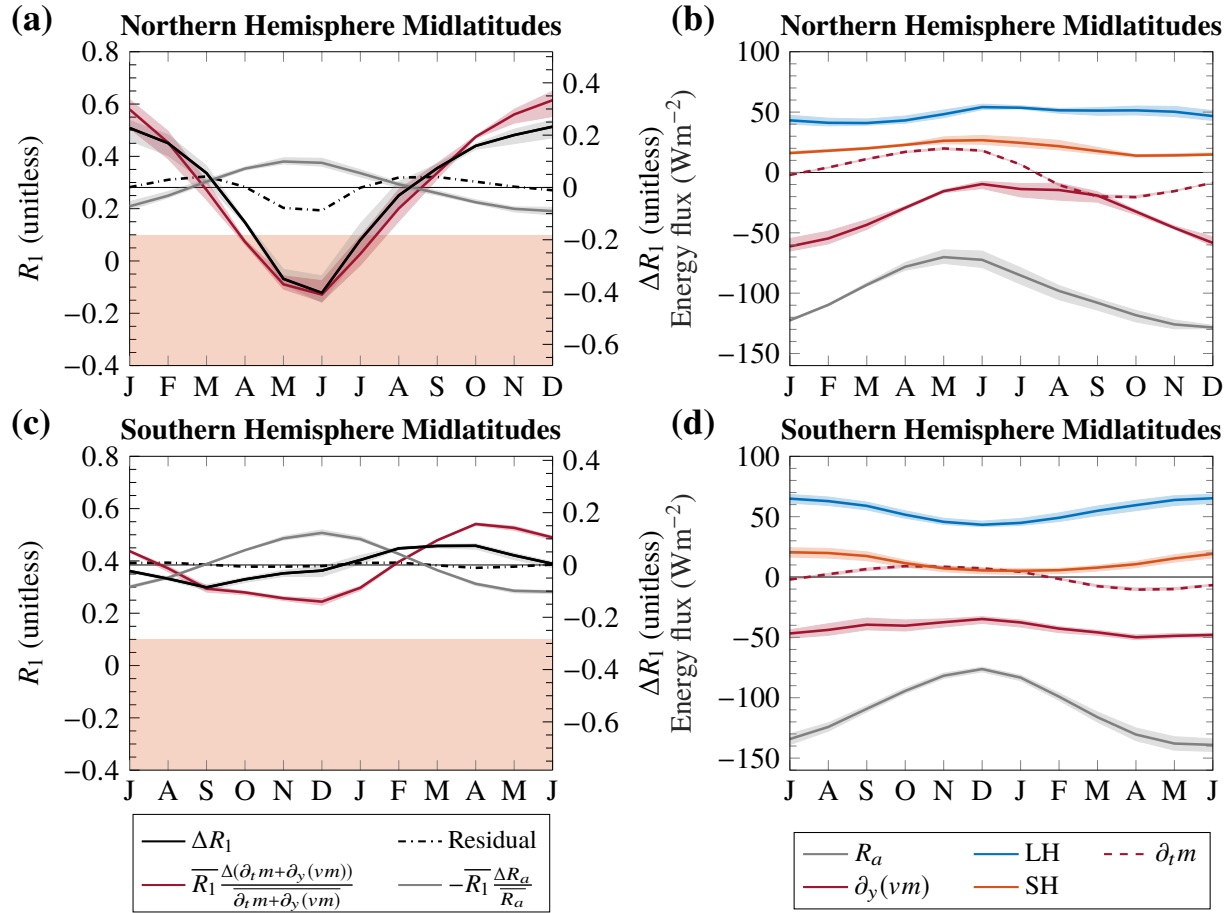
Figure 2.5: The seasonality of R_1 in the midlatitudes (40 to 60°, thick black line, left axis) and its deviation from the annual mean (horizontal black line), ΔR_1 (right axis), are shown for the (a) Northern and (c) Southern Hemisphere for the reanalysis mean. The orange shading indicates the RCE regime. ΔR_1 is decomposed into the advective (red line) and radiative (gray line) components according to equation (2.5). The seasonality of the MSE budget terms in the midlatitudes are shown for the (b) Northern and (d) Southern Hemisphere. The shading over the lines indicates the range across the reanalyses.

in the Northern high latitudes (see black line in Fig. 2.2), equation (2.5) simplifies to:

$$\Delta R_1 \approx \frac{1}{\overline{R_a}}\left(\Delta(\partial_t m + \partial_y(vm)) - \Delta R_a\right) + \text{Residual} \qquad (2.6)$$

$$= \frac{1}{\overline{R_a}}\Delta(\text{LH} + \text{SH}) + \text{Residual}\,, \qquad (2.7)$$

where I have used the MSE budget [equation (2.2)]. Thus, the regime transition in the Northern high latitudes is connected to the seasonality of surface turbulent fluxes, which is dominated by an increase in latent heat flux from May to September (blue line, Fig. 2.6b).

In the Southern high latitudes, the seasonality of surface turbulent fluxes and thus ΔR_1 is comparable to that of the Northern high latitudes (compare Fig. 2.6a,b and 2.6c,d). However, there is no regime transition in the Southern high latitudes because annual-mean R_1 is farther from the regime transition threshold for RAE ($\overline{R_1} = 1.36$). The larger annual-mean R_1 is associated with smaller radiative cooling and a persistent downward sensible heat flux (gray and orange lines in Fig. 2.6d).

While the results above focused on the reanalysis mean, similar seasonality is found in the CMIP5 historical simulations (Fig. 2.B.14–2.B.19). In particular, CMIP5 models capture the regime transition in the Northern midlatitudes and its connection to the large seasonality of advection plus storage (Fig. 2.B.18). CMIP5 models also capture the regime transition in the Northern high latitudes and its connection to a summertime increase in latent heat flux (Fig. 2.B.19). Some small differences between the reanalysis and CMIP5 mean are discussed in Appendix 2.B.

(a) Northern Hemisphere High Latitudes

(b) Northern Hemisphere High Latitudes

(c) Southern Hemisphere High Latitudes

(d) Southern Hemisphere High Latitudes

Legend for (a) and (c):
- ΔR_1
- Residual
- $\overline{R_1}\frac{\Delta(\partial_t m + \partial_y(vm))}{\partial_t m + \partial_y(vm)}$
- $-\overline{R_1}\frac{\Delta R_a}{R_a}$

Legend for (b) and (d):
- R_a
- LH
- $\partial_t m$
- $\partial_y(vm)$
- SH
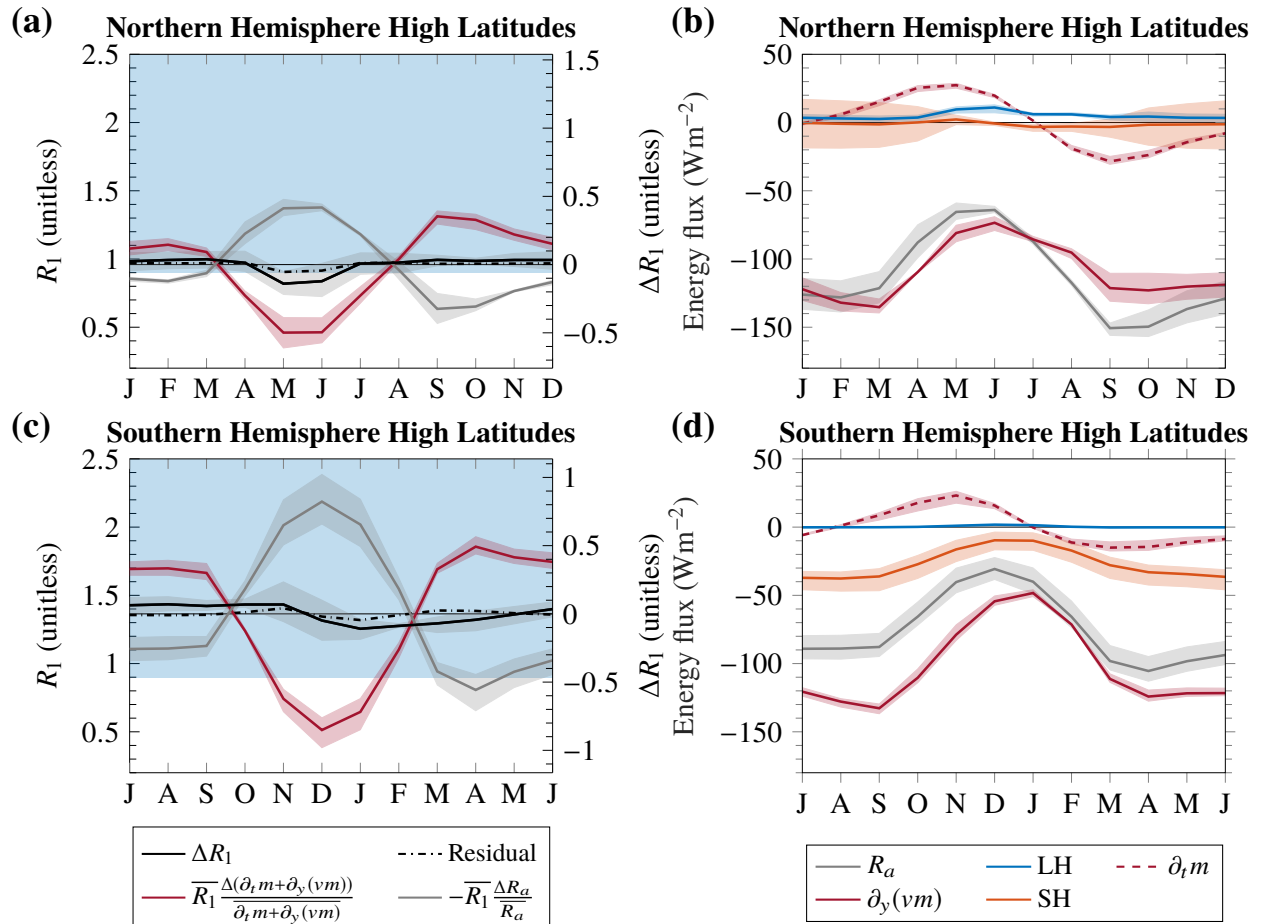
Figure 2.6: Same as Fig. 2.5 but averaged over the high latitudes (80 to 90°).

20

2.4 Testing hypotheses to explain seasonal energy balance regime transitions

2.4.1 Midlatitude regime transition

Previous studies have found that surface heat capacity controls the seasonality of various climate phenomena, such as surface temperature (Donohoe et al., 2014), Intertropical Convergence Zone (Bordoni and Schneider, 2008), and storm track intensity and position (Barpanda and Shaw, 2020), due to its effect on the seasonality of surface energy fluxes. Thus, I hypothesize that surface heat capacity controls the existence of midlatitude energy balance regime transitions. In order to connect the seasonality of R_1 to surface heat capacity, I begin by rewriting the atmospheric MSE budget in terms of top-of-the-atmosphere (F_{TOA}) and surface (F_{SFC}) fluxes following Barpanda and Shaw (2020):

$$\Delta\left(\partial_t m + \partial_y(vm)\right) = \Delta F_{\text{TOA}} - \Delta F_{\text{SFC}} . \tag{2.8}$$

I can write the seasonality of surface fluxes using the surface energy budget of a mixed layer ocean:

$$\Delta F_{\text{SFC}} = \rho c_w d \Delta\left(\partial_t T_s\right) + \Delta(\partial_y F_O) \approx \rho c_w d \Delta\left(\partial_t T_s\right) , \tag{2.9}$$

where ρ is the density of water, c_w is the specific heat capacity of liquid water, d is the mixed layer depth, and $\Delta(\partial_y F_O)$ is the seasonality of meridional ocean heat flux divergence, which I neglect because it is small (Roberts et al., 2017). Finally, I divide by $\overline{R_a}$ and combine equations (2.5), (2.8), and (2.9) to obtain an equation for the seasonality of R_1:

$$\Delta R_1 \approx \frac{\Delta\left(\partial_t m + \partial_y(vm)\right)}{\overline{R_a}} = \frac{1}{\overline{R_a}}\left(\Delta F_{\text{TOA}} - \rho c_w d \Delta\left(\partial_t T_s\right)\right) , \tag{2.10}$$

where the radiative component is assumed to be negligible, consistent with the Northern midlatitudes where the regime transition occurs (see Fig. 2.5a). In order to close equa-

tion (2.10), which depends on the unknown surface temperature tendency, I make use of the EBM (see Section 2.2.4 and Appendix 2.C for more details). Using the analytic EBM, equation (2.10) becomes

$$\Delta R_1 = \frac{Q^*}{R_a} \frac{2D}{(B + 2D)^2 + (\rho c_w d\omega)^2} \left[(B + 2D) \cos(\omega t) + \rho c_w d\omega \sin(\omega t) \right] , \qquad (2.11)$$

where Q^* is the seasonal amplitude of insolation and $\omega = 2\pi$ yr^{-1}. The EBM predicts that the seasonality of R_1 is large for shallow mixed layer depths and small for deep mixed layer depths (black line, Fig. 2.7a). It also predicts that R_1 is in phase with insolation for shallow mixed layer depths and in quadrature with insolation for deep mixed layer depths.

The dependence of the amplitude of ΔR_1 on mixed layer depth in AQUA is qualitatively consistent with the EBM prediction (compare stars to solid black line in Fig. 2.7a). Both AQUA and EBM agree that the midlatitude regime transition from RCAE to RCE only occurs for shallow mixed layer depths. The regime transition occurs in the EBM for $d \leq 16$ m and in AQUA for $d \leq 20$ m (intersection of the line and stars with the orange region in Fig. 2.7a). This is consistent with the observed hemispheric asymmetry in the midlatitude regime transition. The regime transition is absent in the ocean-dominated (deep mixed layer) Southern midlatitudes (Fig. 2.5c) whereas the regime transition occurs in the Northern midlatitudes (Fig. 2.5a), where the land fraction is higher (shallower mixed layer depth).

The phase of R_1 is also a function of the mixed layer depth in AQUA (Fig. 2.7b). The seasonal minimum of R_1 occurs as early as June in AQUA with a 3 m mixed layer depth and as late as September with a 50 m mixed layer depth. While AQUA with a 3 m mixed layer depth captures the phase of R_1 in the Northern midlatitudes in reanalysis data, it overpredicts the amplitude by a factor of three (compare cyan line in Fig. 2.7b with black line in Fig. 2.5a). This suggests that the seasonality in the Northern Hemisphere may be the result of zonal variations in surface heat capacity (land vs ocean).

When AQUA is configured with a mixed layer depth of 15 m, the amplitude of the R_1
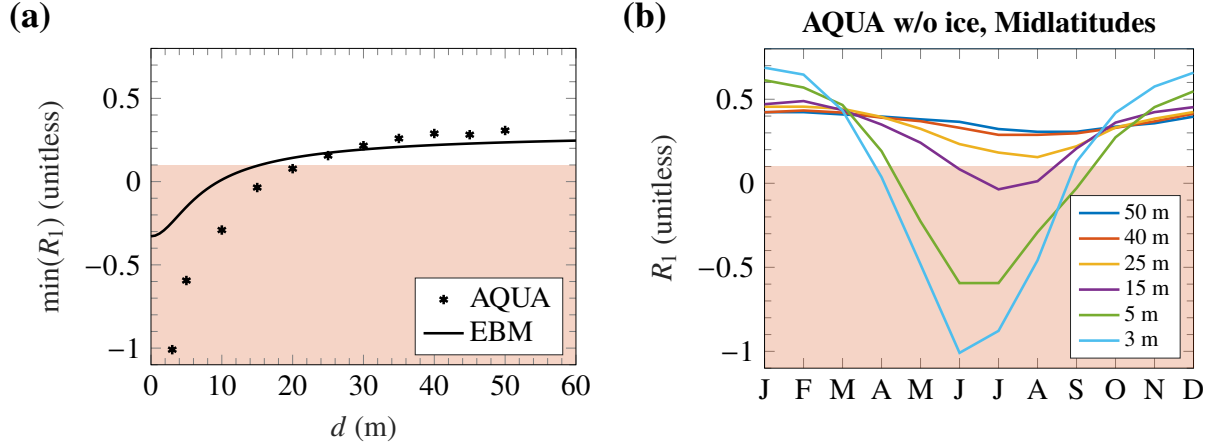
Figure 2.7: (a) Midlatitude ($40°$ to $60°$) R_1 seasonality measured by the minimum value of R_1 predicted by the EBM (solid black line) and simulated by AQUA (stars). (b) Seasonality of midlatitude ($40°$ to $60°$) R_1 for various mixed layer depths in AQUA without sea ice. The orange region denotes the RCE regime.

seasonality closely resembles the Northern midlatitudes (compare Fig. 2.8a and Fig. 2.5a). However, the regime transition in AQUA with a 15 m mixed layer depth lags that in reanalysis data as discussed above. The regime transition in AQUA is associated with a large seasonality of advection plus atmospheric storage, consistent with the Northern midlatitudes in reanalysis data (compare Fig. 2.8b to 2.5b).

When AQUA is configured with a 40 m mixed layer depth, ΔR_1 closely resembles the Southern midlatitudes; namely, there is no regime transition (compare Fig. 2.8c and Fig. 2.5c). The persistence of the RCAE regime throughout the seasonal cycle in the 40 m aquaplanet simulation can be attributed to the weak seasonality of advection plus atmospheric storage, consistent with the results for the Southern midlatitudes in reanalysis data (compare Fig. 2.8d and 2.5d).

2.4.2 High-latitude regime transition

The polar regions on Earth are fundamentally different in that the Northern Hemisphere has a polar ocean whereas the Southern Hemisphere has a polar continent. Given these differences, I quantify the importance of the following mechanisms for the energy balance
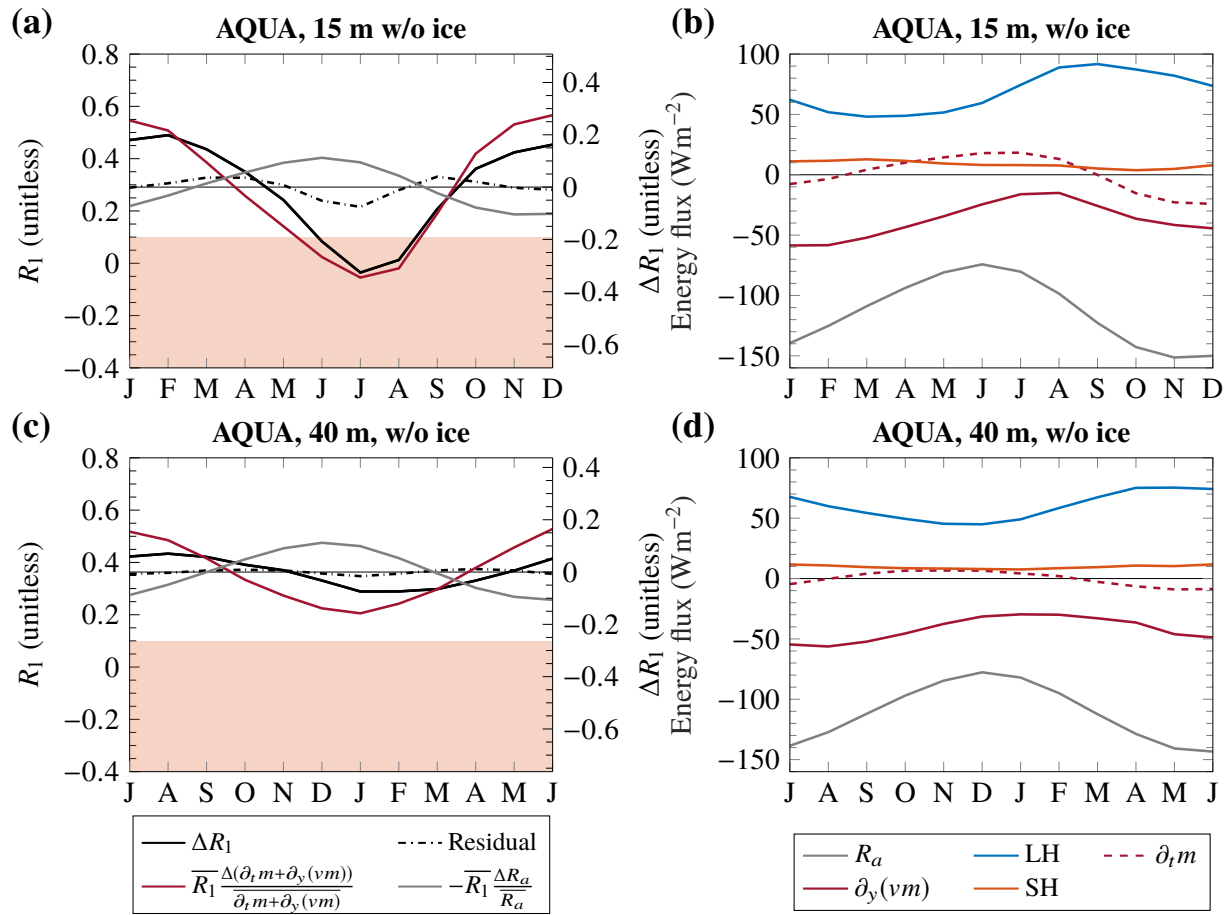
Figure 2.8: Same as Fig. 2.5 but for AQUA without sea ice for (a,b) 15 m and (c,d) 40 m mixed layer depth.

Table 2.1: Annual-mean, high latitude (80°–90°) R_1 and energy balance regimes for varied mixed layer depths (d) in AQUA with and without thermodynamic sea ice.

AQUA without ice	d (m)	$\overline{R_1}$	Regime
	5	0.74	RCAE
	10	0.80	RCAE
	15	0.79	RCAE
	25	0.76	RCAE
	40	0.77	RCAE
	50	0.76	RCAE
AQUA with ice			
	25	1.03	**RAE**
	30	0.95	**RAE**
	35	0.94	**RAE**
	40	0.94	**RAE**
	45	0.88	RCAE
	50	0.86	RCAE

regime seasonality in the high latitudes: 1) sea ice in the Arctic and 2) topography in the Antarctic.

Sea ice in the Arctic affects the surface heat capacity, surface albedo, and surface turbulent fluxes (Andreas et al., 1979; Maykut, 1982). I therefore expect sea ice to play a key role in the seasonality of energy balance regimes in the Northern high latitudes. I test the importance of sea ice using mechanism-denial experiments where AQUA is configured with and without thermodynamic sea ice for various mixed layer depths (Section 2.2.4).

Without sea ice, AQUA has a fixed surface albedo of the ocean (0.07) and in the annual mean, the high latitudes are in the RCAE and mixed lapse rate regime for all mixed layer depths (Table 2.1 and Fig. 2.9a,b). Thus, the low surface heat capacity effect of sea ice alone cannot account for the occurence of annual-mean RAE in the Northern high latitudes.

With sea ice, the annual-mean high latitudes in AQUA are in the RAE and surface inversion lapse rate regime for 25 through 40 m mixed layer depths (Table 2.1 and Fig. 2.9c,d). For deeper mixed layer depths, the high latitudes are in RCAE. Thus, sea ice is a necessary but not a sufficient condition for obtaining annual-mean RAE in the Northern high latitudes.
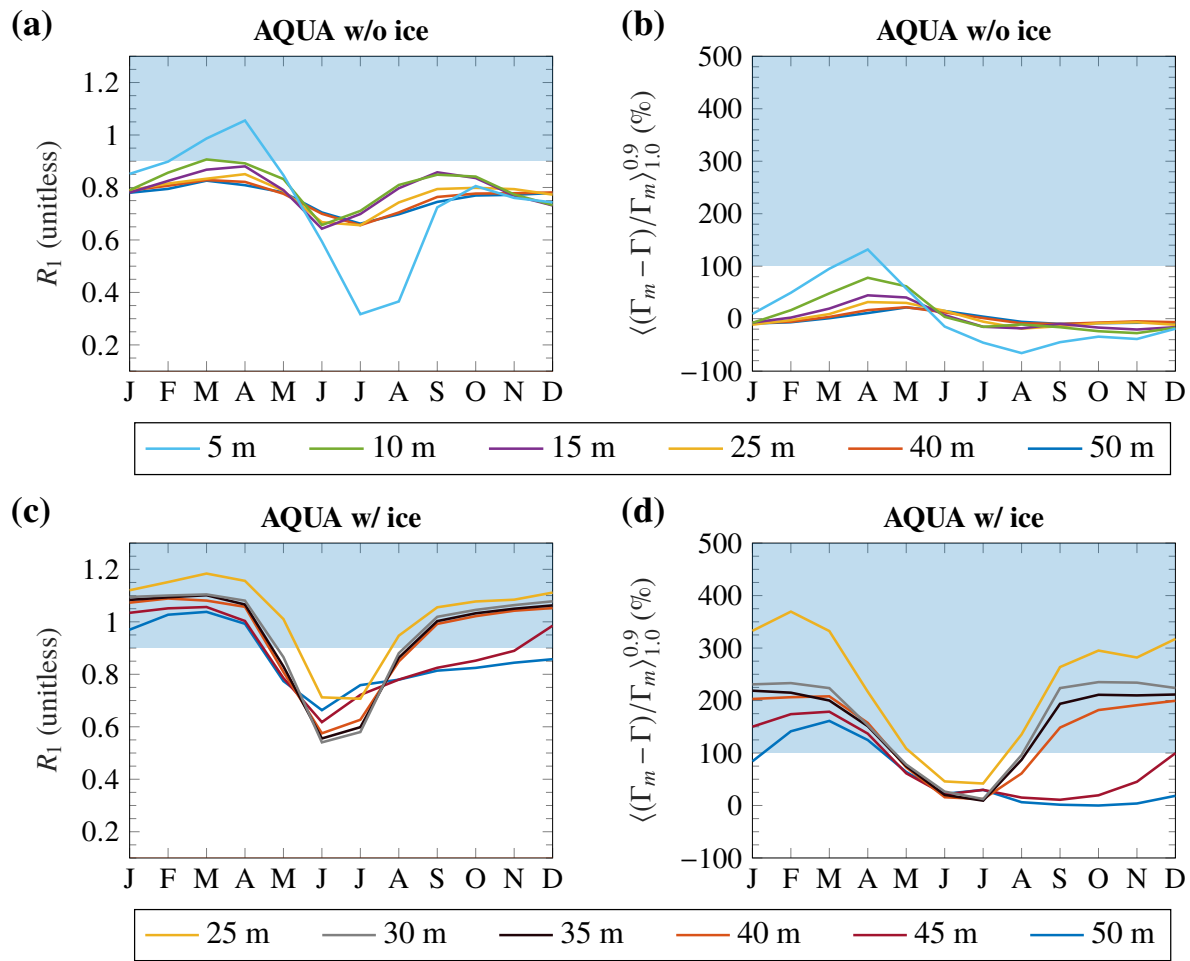
Figure 2.9: (a) Seasonality of high latitude (80° to 90°) R_1 and (b) the boundary layer lapse rate deviation from a moist adiabat for various mixed layer depths in AQUA without sea ice. (c,d) Similar, but for AQUA with sea ice.

Without sea ice, the high latitudes in AQUA do not exhibit a seasonal regime transition from RCAE to RAE across most mixed layer depths (10 to 50 m, see Fig. 2.9a). The exception is the shallowest mixed layer depth (5 m), which exhibits a transition to RAE from March to May (Fig. 2.9a). However, the timing of the regime transition is not consistent with reanalysis data (Fig. 2.6a).

With sea ice, the high latitudes in AQUA exhibit a seasonal regime transition from RCAE to RAE across all mixed layer depths (25 to 50 m, Fig. 2.9c,d). For shallower mixed layer depths (25 to 40 m), the RAE and surface inversion regime occur from September to April (Fig. 2.9c,d). For deeper mixed layer depths (45 and 50 m), the RAE regime only occurs from December to April (Fig. 2.9c,d). The timing of energy balance and lapse rate regime transitions coincides in AQUA with ice (compare Fig. 2.9c and 2.9d). In contrast, the timing of the energy balance and lapse rate regimes exhibit a discrepancy in the reanalysis data (Fig. 2.4b). The summertime energy balance regime transition in the reanalysis data is better represented by AQUA with shallower mixed layer depths (compare solid black line in Fig. 2.4b and 25 to 40 m lines in Fig. 2.9c). On the other hand, the extended lapse rate regime transition in the reanalysis data is better represented by AQUA with deeper mixed layer depths (compare blue line in Fig. 2.4b to 45 and 50 m lines in Fig. 2.9d).

The different timing of the seasonal RCAE to RAE regime transition in the high latitudes in AQUA with sea ice coincides with different sea-ice fraction and depth during fall (Fig. 2.10). For shallower mixed layer depths (25 to 40 m), the high latitudes are in RAE in fall, which is associated with full coverage (Fig. 2.10b) of thick sea ice (Fig. 2.10c) and a high surface albedo (Fig. 2.10c). For deeper mixed layer depths (45 and 50 m), the high latitudes are in RCAE in the fall, which is associated with partial coverage (Fig. 2.10b) of thin sea ice (Fig. 2.10c) and lower albedo (Fig. 2.10a). These results suggest that sea ice impacts the timing of high latitude regime transitions through the combined effect of surface albedo and effective surface heat capacity, which themselves depend on the mixed layer depth in AQUA.

In the Antarctic, the annual-mean value of R_1 is larger than in the Arctic and there

27
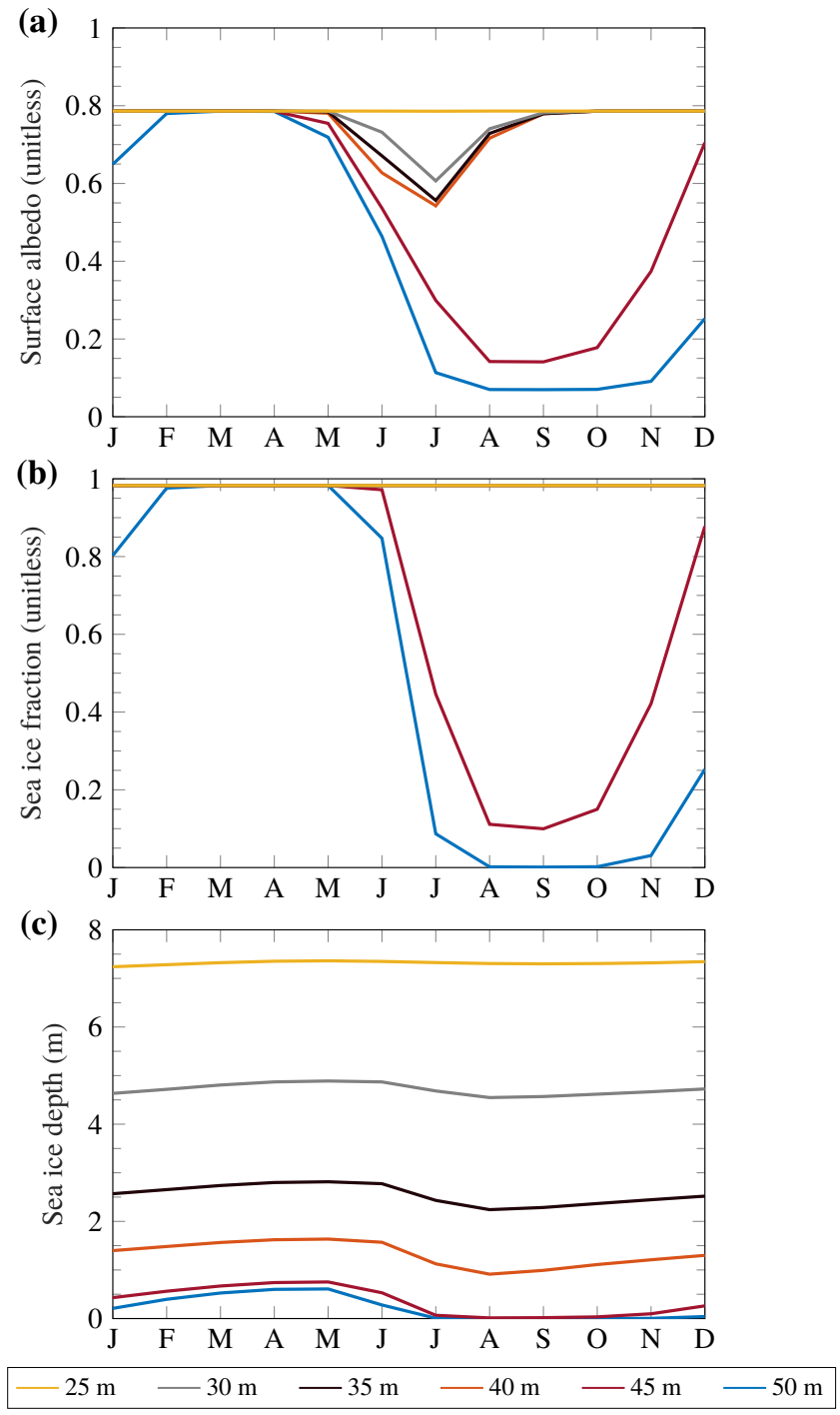
Figure 2.10: Seasonality of high latitude (80° to 90°) (a) surface albedo, (b) sea-ice fraction, and (c) sea-ice depth for various mixed layer depths in AQUA with sea ice.

is no regime transition from RAE to RCAE. In the presence of Antarctic topography, the atmosphere is optically thinner, so that I expect atmospheric radiative cooling to be weaker (Jeevanjee and Romps, 2018), and thus $R_1 = (\partial_t m + \partial_y(vm))/R_a$ to be larger. I therefore investigate the impact of Antarctic topography on the seasonality of energy balance regimes using mechanism-denial experiments. In particular, I use the CESM simulations configured with and without Antarctic topography by Hahn et al. (2020).

The control CESM simulation with Antarctic topography captures the seasonality of R_1 in the reanalyses and CMIP5 historical runs. In particular, the Northern high latitudes undergo a RAE to RCAE regime transition in June (solid line intersects the white region in Fig. 2.11a) while the Southern high latitudes remain in RAE year round (dashed line remains in the blue region in Fig. 2.11a). Without Antarctic topography, $\overline{R_1}$ decreases from 1.30 to 1.12 in the Southern high latitudes (compare Fig. 2.11a to 2.11b). However, because topography does not significantly affect summertime R_1, the Southern high latitudes without Antarctic topography continue to remain in RAE year round (dashed line remains in the blue region in Fig. 2.11b). Thus, while Antarctic topography partially explains the large hemispheric asymmetry in annual-mean R_1, it does not explain the lack of an energy balance regime transition in Antarctica.

The hemispheric asymmetry in energy balance regimes also cannot be solely explained by the near-constant high surface albedo in Antarctica, since an energy balance regime transition occurs in the presence of a seasonally invariant high surface albedo in AQUA (see 25 m simulation in Fig. 2.9c). Thus, multiple mechanisms may need to be considered together to understand the seasonality of energy balance regimes in Antarctica.

(a) CESM Control AA, $\phi = 80°$ **to** $90°$ **(b)** CESM Flat AA, $\phi = 80°$ **to** $90°$

—— Northern Hemisphere   ······ Southern Hemisphere (shifted by 6 months)
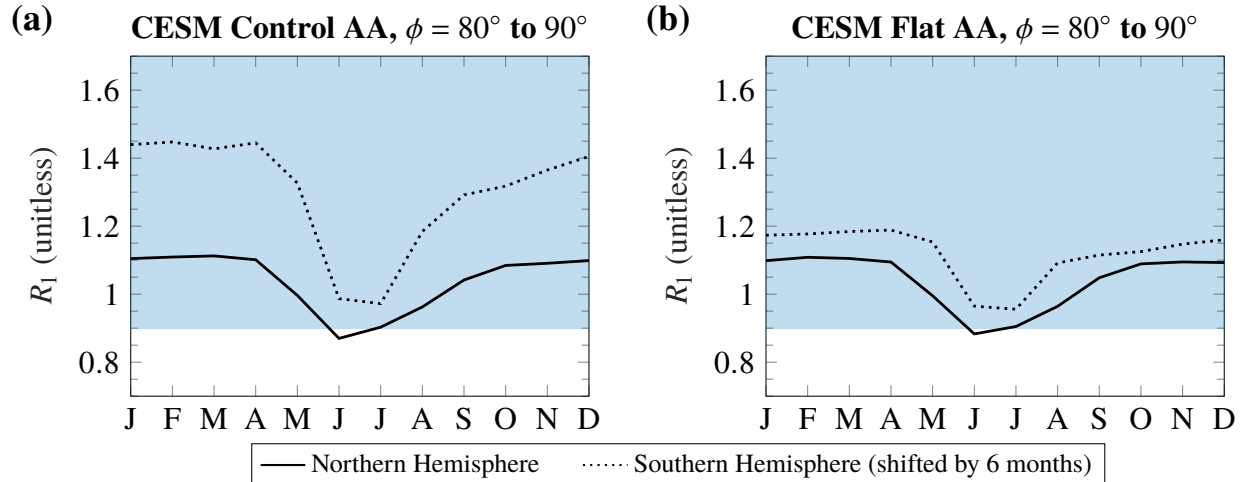
Figure 2.11: Seasonality of R_1 in the CESM simulations performed by Hahn et al. (2020) in the Northern (solid line) and Southern (dotted line) high latitudes for the (a) control simulation with Antarctic topography and (b) flattened Antarctic topography simulation. The Southern Hemisphere seasonality is shifted by 6 months.

2.5 Connecting energy balance regimes in the modern climate to the vertical structure of the warming response

Here I quantify whether energy balance regimes in the modern climate provide a useful guide to the vertical, latitudinal, and seasonal structure of the warming response. For regions of RCE in the modern climate that stay in RCE in the future, the expectation is that warming maximizes aloft (Held, 1993; Romps, 2011; Miyawaki et al., 2020). On the other hand, for regions of RAE in the modern climate that stay in RAE in the future, the expectation is that warming maximizes at the surface, assuming that the change in advective heat flux is negligible (Held, 1993; Payne et al., 2015).

In the annual mean, the CMIP5 multimodel mean latitudinal structure of energy balance regimes remains unchanged by the end of the century with the exception of a small region between 75°–80°N (compare solid and dashed lines in Fig. 2.12a). Consistently, regions of RCE in the modern climate exhibit amplified warming aloft (red lines, $R_1 \leq 0.1$ in Fig. 2.12b) and regions of RAE in the modern climate exhibit amplified warming at the surface (blue lines, $R_1 \geq 0.9$ in Fig. 2.12b). Thus, energy balance regimes defined using R_1 in the modern

climate can be used to interpret the vertical structure of the annual-mean warming response.

The seasonality of energy balance regimes in the tropics and Southern high latitudes is largely unchanged in response to warming (compare dashed and solid thick contours in Fig. 2.13). Consistently, the tropics, which are a region of RCE in the modern climate and stay in RCE in the future, exhibit amplified warming aloft throughout the seasonal cycle (red-filled contours in Fig. 2.13). Furthermore, the Southern high latitudes, which are a region of RAE in the modern climate and stay in RAE in the future, exhibit amplified surface warming throughout the seasonal cycle (blue-filled contours in Fig. 2.13). Thus, energy balance regimes in the modern climate can also be used to interpret the vertical structure of the warming response seasonally in the tropics and Southern high latitudes.

In the Northern Hemisphere mid and high latitudes, energy balance regimes in the modern climate are less directly related to the vertical structure of the warming response. In the Northern midlatitudes, there is a phase shift between the seasonality of energy balance regimes in the modern climate and the seasonality of the lapse rate change (compare thick orange line to filled contours in Fig. 2.13). This discrepancy is similar to the phase shift between the seasonality of energy balance and lapse rate regimes in the modern climate (compare Fig. 2.3a and 2.3b). This suggests that seasonal atmospheric heat storage may again be playing a role in delaying the seasonality of the lapse rate change relative to that of energy balance regimes.

The Northern high latitudes exhibit significant changes in energy balance regimes in response to warming (compare solid and dashed blue lines in Fig. 2.13), which coincide with significant changes in the advective heat flux into the Arctic, especially during summertime (not shown). Thus, the assumptions required for using energy balance regimes in the modern climate to interpret the warming response are not satisfied in the Arctic.
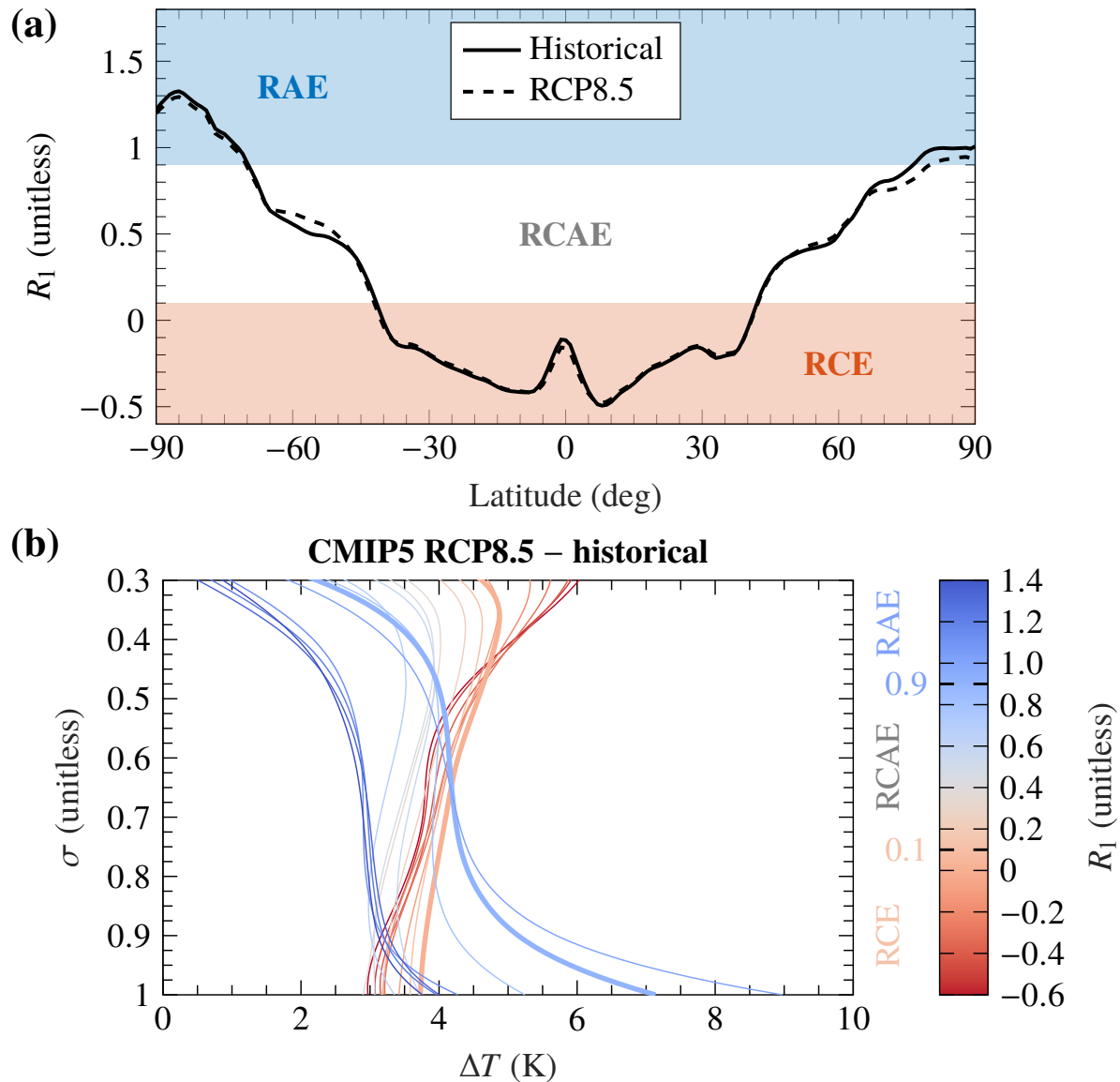
Figure 2.12: (a) The zonal-mean, annual-mean structure of R_1 for the historical (solid black line) and RCP8.5 (dashed black line) CMIP5 multimodel mean. Orange, white, and blue regions indicate RCE, RCAE, and RAE, respectively. (b) The projected end of century temperature response to increased CO_2 binned by R_1 in the modern climate (bin widths are 0.1) for the CMIP5 multimodel mean. Thick blue and orange lines correspond to $R_1 = 0.9$ and $R_1 = 0.1$, respectively.
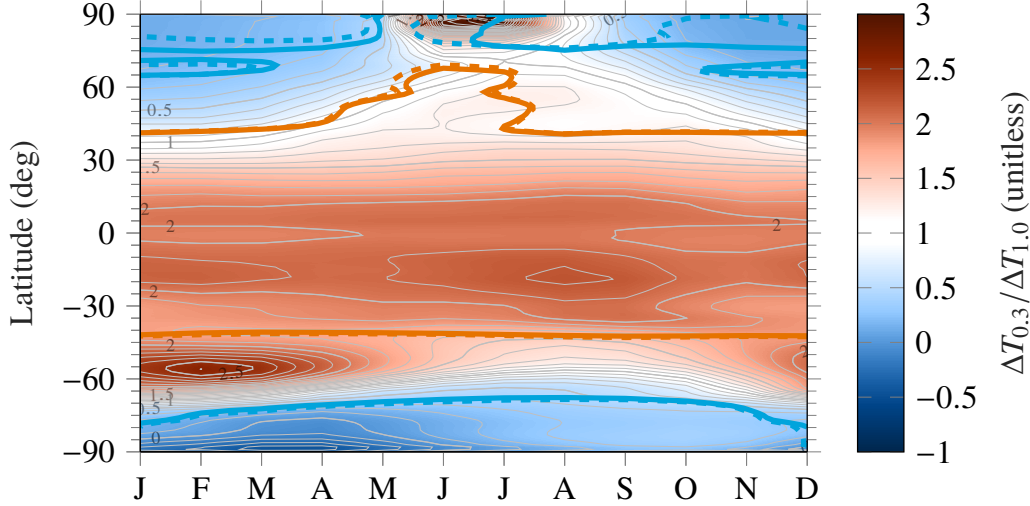
Figure 2.13: The ratio of the temperature response to increased CO_2 in the upper troposphere ($\sigma = 0.3$) and the surface ($\sigma = 1.0$) are shown as filled contours (contour interval is 0.1) for the CMIP5 multimodel mean. The RCE/RCAE boundary is shown as a thick orange contour and the RAE/RCAE boundary is shown as a thick blue contour (solid for historical, dashed for RCP8.5).

2.6   Summary and Discussion

2.6.1   Summary

I quantified energy balance regimes in the modern climate, their link to lapse rate regimes, and their response to warming. I used the vertically-integrated moist static energy budget to define a nondimensional number $R_1 = (\partial_t m + \partial_y(vm))/R_a$ that quantifies regions of RCE ($R_1 \leq 0.1$), RAE ($R_1 \geq 0.9$), and RCAE ($0.1 < R_1 < 0.9$). In the annual mean, the RCE regime occurs equatorward of $40°$, consistent with the occurence of the moist adiabatic lapse rate regime. The RAE regime occurs poleward of $80°$N and $70°$S, consistent with the occurence of the surface inversion lapse rate regime. Lastly, the RCAE regime occurs between 40 to $70°$S and 40 to $80°$N, consistent with the occurence of the mixed lapse rate regime (more stable than a moist adiabat but does not exhibit a surface inversion).

Energy balance and lapse rate regimes in the modern climate exhibit weak seasonality in the Southern Hemisphere. In the Northern Hemisphere, regime transitions occur from RCAE to RCE in the midlatitudes and from RAE to RCAE in the high latitudes. The lapse

rate also shows seasonal regime transitions in the Northern mid and high latitudes, but there is a phase shift relative to the energy balance regime transition by 1 to 3 months. In the Northern midlatitudes, this phase shift is associated with the seasonality of atmospheric storage.

A linear decomposition of the R_1 seasonality shows that the regime transition in the Northern Hemisphere midlatitudes is associated with the large seasonality of advection plus atmospheric storage. I hypothesized using an EBM that surface heat capacity controls the amplitude of advection plus storage and thus the seasonal regime transition in the Northern midlatitudes. The hypothesis was confirmed by varying the mixed layer depth in aquaplanet simulations. As predicted by the EBM, aquaplanet simulations show that the amplitude of the R_1 seasonality increases as the mixed layer depth decreases. The midlatitude regime transition occurs for mixed layer depths less than 20 m in the aquaplanet. The phase of R_1 is also a function of the mixed layer depth in the aquaplanet, where the RCE regime transition occurs earlier in the season for shallower mixed layer depths. The importance of surface heat capacity on the seasonal amplitude of advection plus storage in the midlatitudes is consistent with Barpanda and Shaw (2020).

To understand the seasonality of energy balance regimes in the high latitudes, I tested the importance of sea ice for a polar ocean (Arctic) and topography for a polar continent (Antarctica) using mechanism-denial experiments. In the annual mean, the RAE regime only occurs over a polar ocean when thermodynamic sea ice is enabled. The energy balance regime seasonality depends on the seasonality of sea ice, which itself depends on the mixed layer depth in the aquaplanet. For shallower (25 to 40 m) mixed layer depths, RAE occurs from September to April when sea-ice fraction, thickness, and surface albedo are large year round. For deeper (45 and 50 m) mixed layer depths, RAE disappears in the fall when sea-ice fraction, thickness, and surface albedo are small. Using the CESM experiments conducted by Hahn et al. (2020), I found that Antarctic topography alone cannot explain the lack of a high latitude regime transition over Antarctica.

Finally, I showed that energy balance regimes in the modern climate can be used to interpret the vertical structure of the warming response in the annual mean, and seasonally in the tropics and the Southern high latitudes. In the annual mean, regions of RCE in the modern climate that remain in RCE in the future exhibit amplified warming aloft. Regions of RAE in the modern climate that remain in RAE in the future exhibit amplified warming at the surface. Similar results hold seasonally in the tropics and the Southern high latitudes. However, in the Northern Hemisphere mid and high latitudes, the seasonality of energy balance regimes in the modern climate is less directly related to the warming response due to the role of atmospheric heat storage in the midlatitudes and large changes in energy balance regimes in the Arctic.

2.6.2   Discussion

These findings are consistent with Jakob et al. (2019), who showed that the tropics are close to RCE over large temporal (>daily) and spatial scales (> 5000 km, achieved here through taking the zonal mean). Jakob et al. (2019) use the DSE budget to define RCE and primarily focus on the implications of the validity of RCE in the context of CRM configurations and convective aggregation in the tropics. This work focuses on the nondimensional MSE budget, which has the advantage that it can be used as a more general criterion for defining energy balance regimes outside the tropics and in climates different from Earth's modern climate.

The energy balance regimes defined here were based on the vertically-integrated MSE budget. The vertically-integrated budget is useful but it may have limitations when the vertical structure of advection, atmospheric storage, and radiation are important. For example, the discrepancy between the seasonality of energy balance and lapse rate regimes in the Northern high latitudes may be related to different vertical structures of advection and atmospheric storage. Extending the RAE model of Cronin and Jansen (2016) to explicitly include atmospheric storage would be helpful for understanding the discrepancy.

While the mechanism-denial experiments involving sea ice show that sea ice is a neces-

sary condition to reproduce the seasonality of energy balance regimes in the Northern high latitudes, further experiments are necessary to 1) understand the discrepancy between the timing of energy balance and lapse rate regimes in the reanalysis data and 2) isolate the importance of the seasonally varying effective surface heat capacity and surface albedo effect of sea ice. Progress on 1) can be made by increasing the complexity of the sea ice representation (e.g., adding zonal asymmetry, sea ice dynamics) until the discrepancy in the timing of energy balance and lapse rate regimes can be reproduced. Progress on 2) can be made by running experiments with sea ice where the surface albedo is prescribed.

Our understanding of the Southern high latitude energy balance regime seasonality remains incomplete. In particular, experiments involving topography and a seasonally invariant high albedo were not successful in explaining the lack of a summertime regime transition in the Southern high latitudes. Future work could test the sensitivity of the results to variations in surface albedo beyond the range explored here, the role of alternative mechanisms such as clouds and the large-scale circulation, or the confluence of multiple mechanisms.

The connection between energy balance regimes in the modern climate and the vertical structure of the global warming response demonstrated here using state-of-the-art GCMs complements the findings of Payne et al. (2015). However, a complete understanding of the latitudinal and seasonal structure of the vertical temperature response in the Northern Hemisphere mid and high latitudes and Southern Hemisphere midlatitudes requires further investigation. Previous studies show the vertical structure of the warming response in the RAE model is sensitive to the type of forcing (Payne et al., 2015; Cronin and Jansen, 2016). Thus, decomposing the change in R_1 into advective and radiative components and investigating their link to the warming response may be a fruitful direction for future work.

The framework I introduced for quantifying energy balance regimes can be used to explore many interesting areas for future work. The framework can be extended to study the zonal structure of energy balance regimes. The role of zonal variations in surface heat capacity (land versus ocean) may be explored for the timing and amplitude of the Northern Hemi-

sphere regime transitions. The framework can also be applied to quantify energy balance regime transitions in various paleoclimates. Previous studies suggest that high latitudes during warm epochs, such as the Eocene, may have been close to RCE (Abbot and Tziperman, 2008a) whereas RAE was more widespread during Snowball Earth (Pierrehumbert, 2005). These are all exciting areas for future work.

2.A   Appendix A: Lapse rate deviation from the moist adiabat

I use a centered finite difference of monthly pressure level temperature and geopotential data to compute the lapse rate and convert to sigma coordinates by masking out the data below surface pressure and taking a cubic spline interpolation. I perform this conversion for every latitude and longitude grid point.

Following Stone and Carlson (1979), I define the deviation of the lapse rate from the moist adiabatic lapse rate as the fractional difference:

$$\delta_c = \frac{\Gamma_m - \Gamma}{\Gamma_m} \tag{2.12}$$

where Γ is the actual lapse rate in the reanalysis or GCM and Γ_m is the moist adiabatic lapse rate as defined in equation (3) in Stone and Carlson (1979).

2.B   Appendix B: Differences between the CMIP5 historical multimodel mean and the reanalysis mean

In the reanalysis mean, there is a location of anomalously stable stratification between $\sigma = 0.9$ to 0.7 for $R_1 = 0$ (Fig. 2.1). This leads to a nonmonotonic relationship between the lapse rate deviation and R_1 in the vicinity of $\sigma = 0.8$. In comparison, the lower tropospheric stability does not show a similarly pronounced peak and the lapse rate deviation is monotonic with respect to R_1 for the CMIP5 multimodel mean (Fig. 2.B.14).
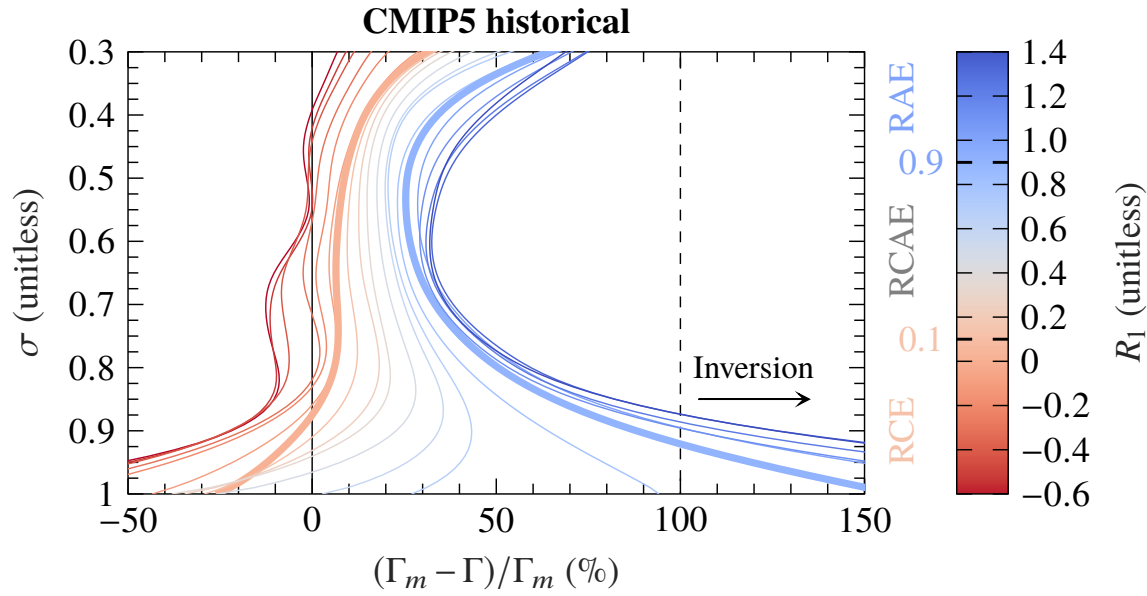
Figure 2.B.14: Same as Fig. 2.1 but for the CMIP5 historical multimodel mean.

In the reanalysis mean, there is a clear hemispheric asymmetry in the high latitude R_1 seasonality (compare Fig. 2.6a and 2.6c). In addition, there is a corresponding asymmetry in the seasonality of the boundary layer lapse rate, where the lapse rate deviation in the Northern high latitudes indicates that the inversion vanishes during summertime whereas the inversion persists year round in the Southern high latitudes (Fig. 2.3c). The asymmetry differs somewhat in the CMIP5 multimodel mean. Notably, R_1 exhibits stronger seasonality in the Southern Hemisphere and approaches the margin of the RCAE regime during summertime (compare Fig. 2.B.19c and 2.6c). Consistent with an energy balance state on the margin of RCAE, the inversion vanishes in the Southern high latitudes during summertime (Fig. 2.B.16c).

Table 2.B.2: List of the 36 models that comprise the CMIP5 multimodel mean of the historical and RCP8.5 runs.

Models
ACCESS1-0
ACCESS1-3
bcc-csm1-1
bcc-csm1-1-m
BNU-ESM
CanESM2
CCSM4
CESM1-BGC
CESM1-CAM5
CMCC-CESM
CMCC-CM
CNRM-CM5
CSIRO-Mk3-6-0
FGOALS-g2
GFDL-CM3
GFDL-ESM2G
GFDL-ESM2M
GISS-E2-H
GISS-E2-H-CC
GISS-E2-R
GISS-E2-R-CC
HadGEM2-CC
HadGEM2-ES
inmcm4
IPSL-CM5A-LR
IPSL-CM5A-MR
IPSL-CM5B-LR
MIROC5
MIROC-ESM
MIROC-ESM-CHEM
MPI-ESM-LR
MPI-ESM-MR
MRI-CGCM3
MRI-ESM1
NorESM1-M
NorESM1-ME
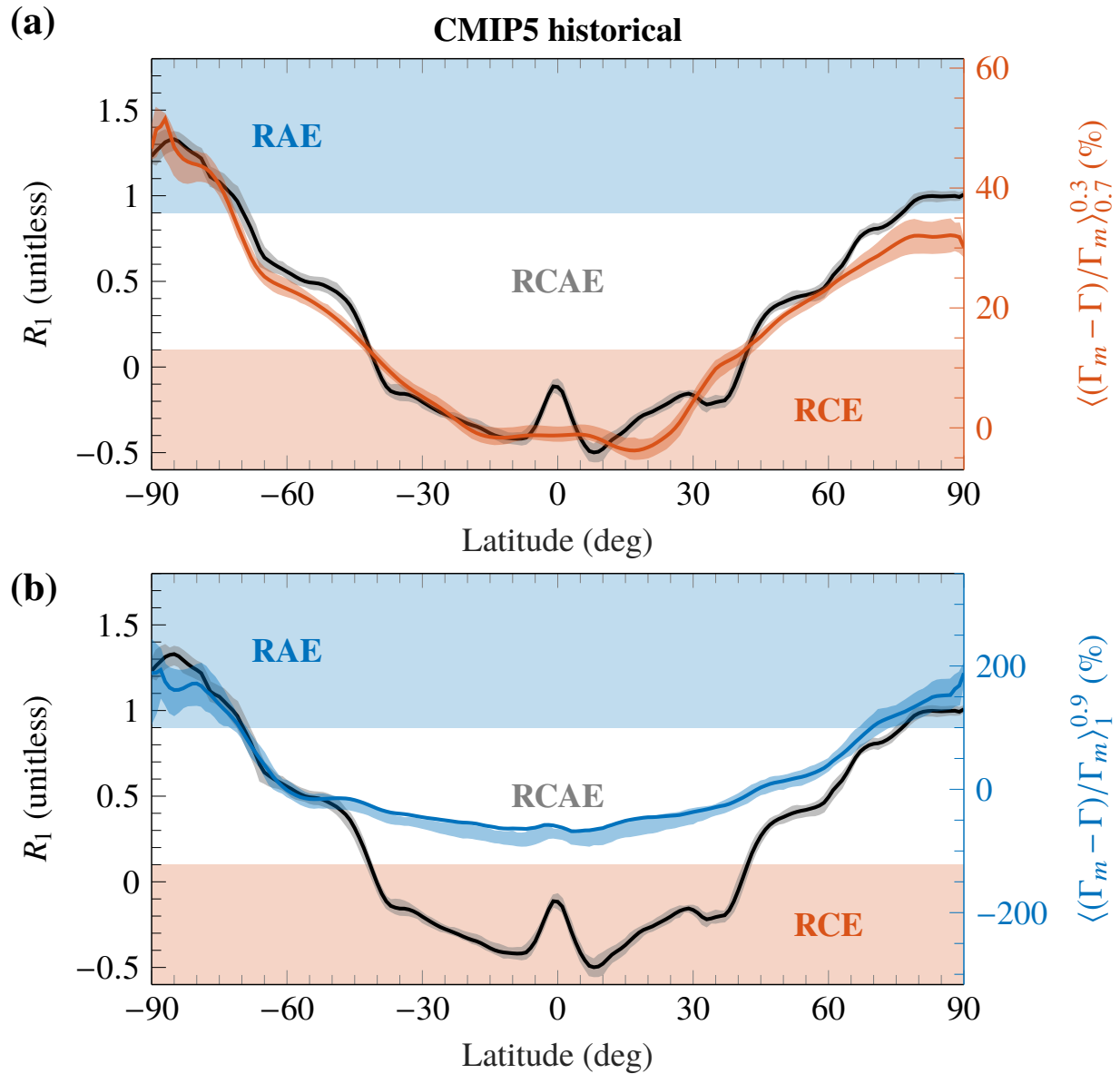
Figure 2.B.15: Same as Fig. 2.2 but for the CMIP5 historical multimodel mean. The shading indicates the interquartile range.
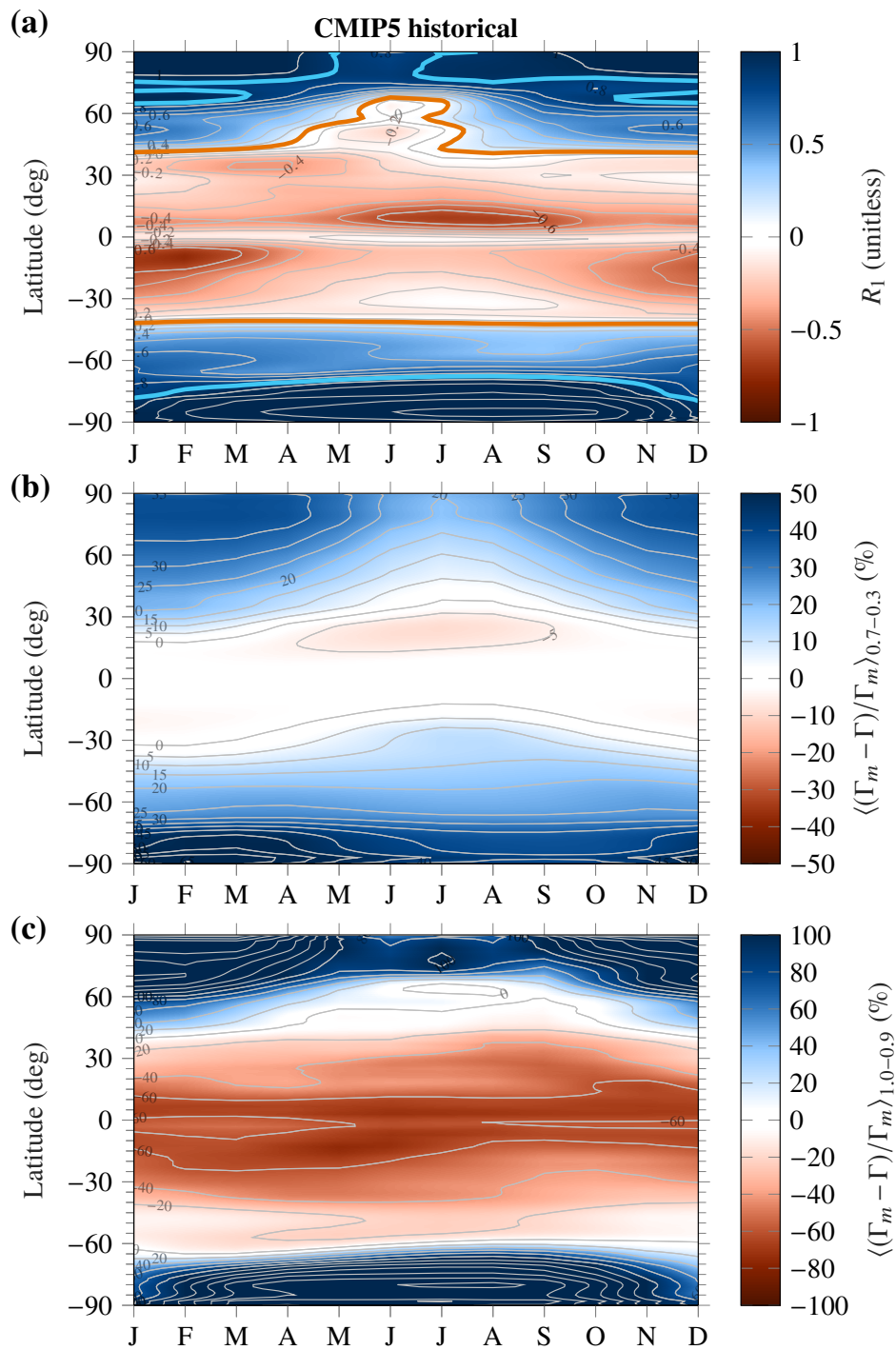
Figure 2.B.16: Same as Fig. 2.3 but for the CMIP5 historical multimodel mean.

(a) CMIP5 historical, NH Midlatitudes

(b) CMIP5 historical, NH High Latitudes

$$\frac{\partial_t m + \partial_y(vm)}{R_a} \qquad \frac{\partial_y(vm)}{R_a}$$
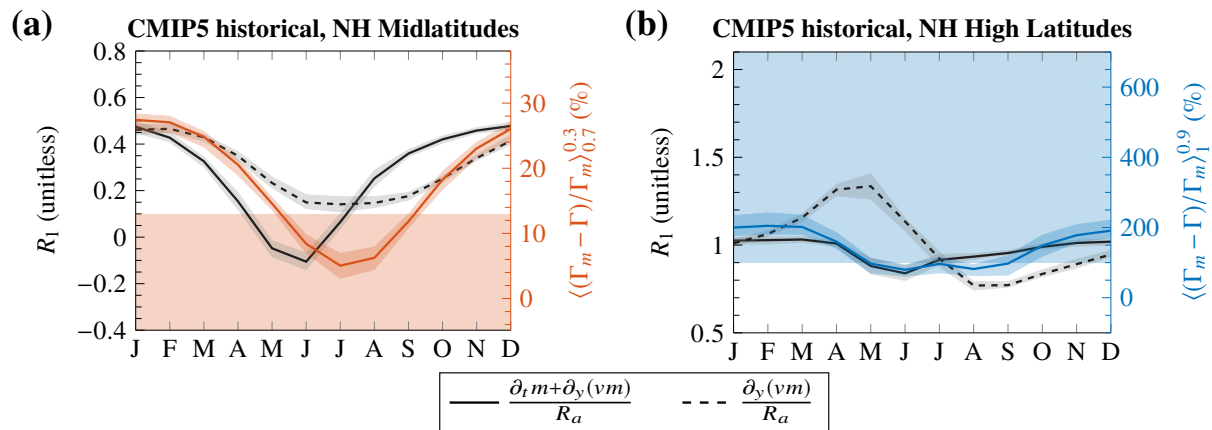
Figure 2.B.17: Same as Fig. 2.4 but for the CMIP5 historical multimodel mean. The shading indicates the interquartile range.

(a) CMIP5 historical, NH Midlatitudes

(b) CMIP5 historical, NH Midlatitudes

(c) CMIP5 historical, SH Midlatitudes

(d) CMIP5 historical, SH Midlatitudes

$$\Delta R_1 \qquad \text{Residual}$$
$$\overline{R_1}\frac{\Delta(\partial_t m + \partial_y(vm))}{\partial_t m + \partial_y(vm)} \qquad -\overline{R_1}\frac{\Delta R_a}{R_a}$$

$$R_a \qquad \text{LH} \qquad \partial_t m$$
$$\partial_y(vm) \qquad \text{SH}$$
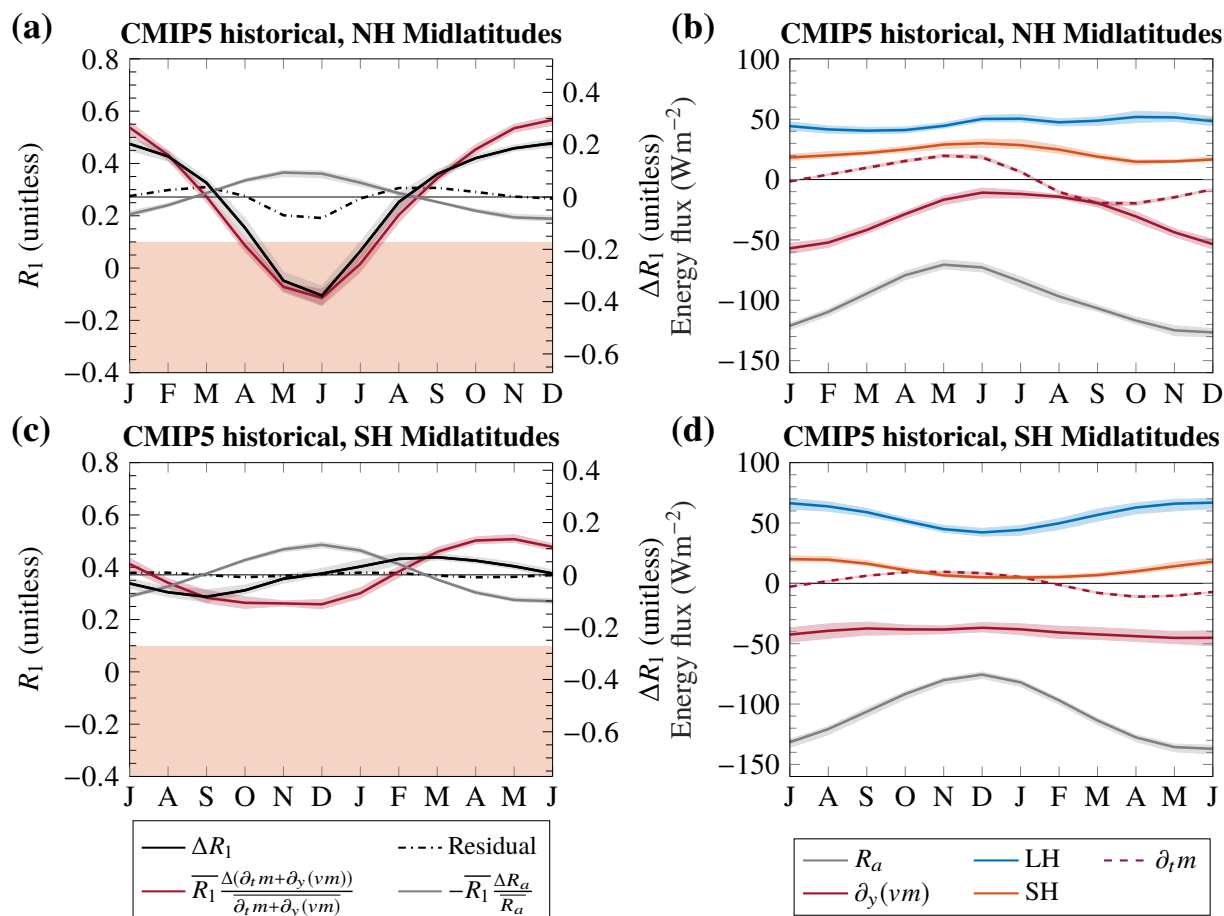
Figure 2.B.18: Same as Fig. 2.5 but for the CMIP5 historical multimodel mean. The shading indicates the interquartile range.

42
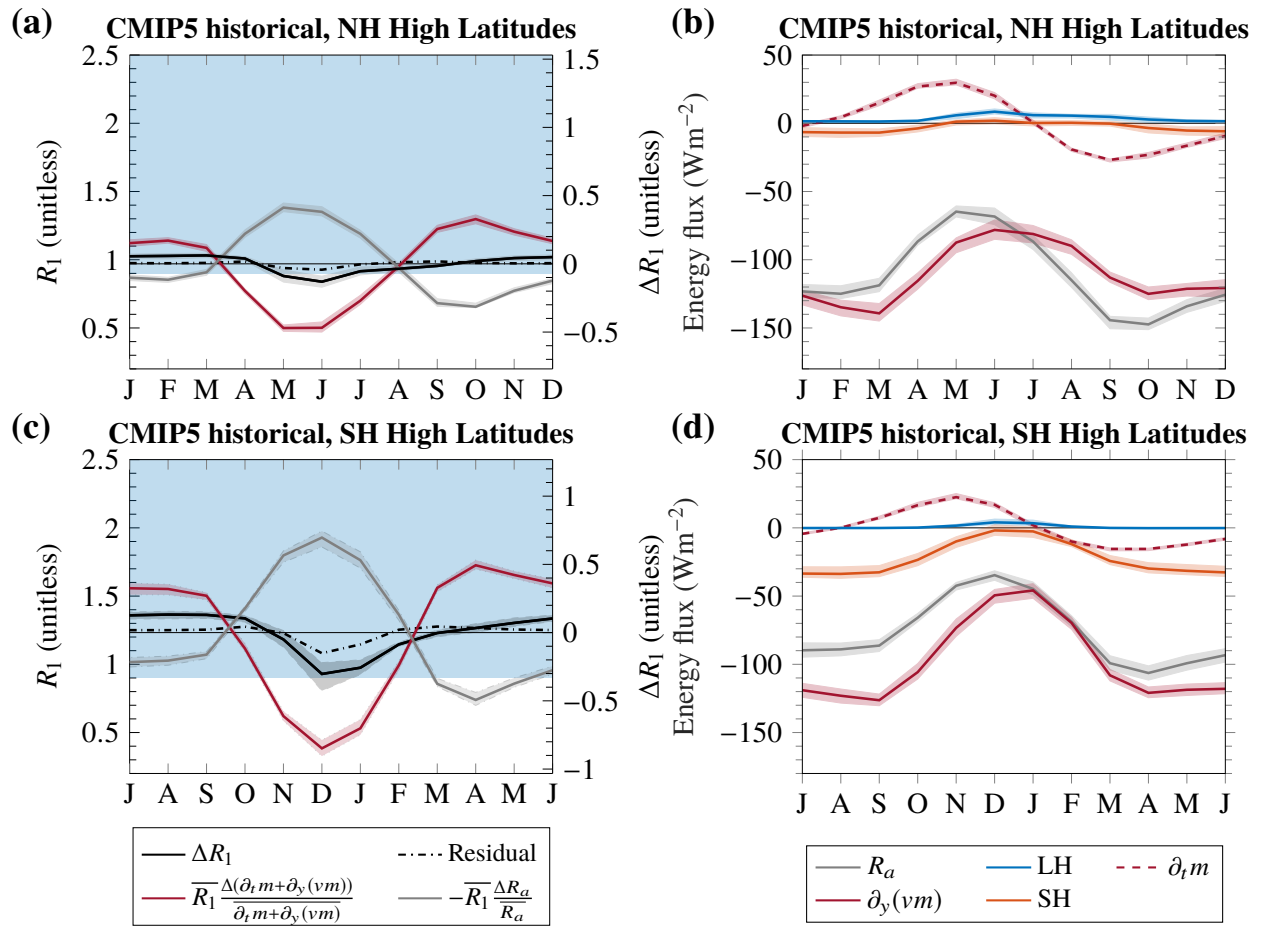
Figure 2.B.19: Same as Fig. 2.6 but for the CMIP5 historical multimodel mean. The shading indicates the interquartile range.

2.C Appendix C: Deriving an analytical expression for ΔR_1 as a function of mixed layer depth

Following the Rose et al. (2017) EBM, I write the seasonality of TOA and SFC fluxes as a Fourier–Legendre series. Here I only consider the first harmonic as it is an order of magnitude larger than the second harmonic in the midlatitudes:

- $\Delta F_{\text{TOA}} \approx a\Delta Q - B\Delta T_s$, where $a\Delta Q = Q^* \cos(\omega t)$. $\omega = 2\pi \text{ yr}^{-1}$, $Q^* = as_{11}Q_gP_1(\phi)$ is the amplitude of net TOA shortwave radiation, $s_{11} = -2\sin\beta$ where β is the obliquity, $P_1(\phi) = \sin\phi$, and $Q_g = 340 \text{ W m}^{-2}$.

- $\Delta T_s = T_s^* \cos(\omega t - \Phi)$, where T_s^* is the amplitude of surface temperature seasonality and Φ is the phase shift of ΔT_s relative to ΔQ. $T_s^* = Q^* \left[(B + 2D)^2 + (\rho c_w d\omega)^2\right]^{-1/2}$ and $\Phi = \arctan\left(\frac{\rho c_w d\omega}{B+2D}\right)$ (see Rose et al. (2017) for the derivation of the analytical expression of surface temperature).

Using the results above, I can write equation (2.10) as

$$\Delta R_1 = \frac{1}{R_a} \left(Q^* \cos(\omega t) - BT_s^* \cos(\omega t - \Phi) + \rho c_w d\omega T_s^* \sin(\omega t - \Phi)\right) . \qquad (2.13)$$

Substituting in T_s^* and Φ and simplifying, I obtain

$$\Delta R_1 = \frac{Q^*}{R_a} \frac{2D}{(B + 2D)^2 + (\rho c_w d\omega)^2} \left[(B + 2D)\cos(\omega t) + \rho c_w d\omega \sin(\omega t)\right] . \qquad (2.14)$$

CHAPTER 3

QUANTIFYING KEY MECHANISMS THAT CONTRIBUTE TO THE DEVIATION OF THE TROPICAL WARMING PROFILE FROM A MOIST ADIABAT

3.1   Introduction

The previous chapter confirmed that convective adjustment to a moist adiabatic lapse rate in RCE qualitatively predicts amplified upper tropospheric warming in response to increased CO_2. In this chapter, I scrutinize the accuracy of moist adiabatic adjustment as a quantitative prediction of amplified warming aloft in the tropics.

Quantitatively, moist adiabatic adjustment together with the Clausius–Clapyeron scaling predicts a 9 K warming aloft in response to a 4 K surface warming assuming a tropical surface temperature of 298 K and a fixed surface relative humidity of 80%. Thus, the moist adiabat predicts the vertical structure of warming in response to surface warming (indirect effect of increased CO_2) and humidity change in regions of deep convection. It does not consider several important additional effects, such as the response outside regions of climatological deep convection, the radiative response that arises in the absence of significant surface warming (direct effect of increased CO_2), and the influence of convective processes such as entrainment.

The moist adiabat predicts the atmospheric temperature of an ascending plume given the surface conditions of the rising air parcel. It does not account for surface heterogeneities that lead to decoupling between the surface and atmosphere in regions of climatological descent. Andrews and Webb (2018) show that localized SST warming in the tropical western Pacific (region of climatological ascent) in HadGEM2-A results in amplified warming aloft whereas warming in the eastern Pacific (region of climatological descent) does not. Previous authors

show that the tropospheric temperature response is more strongly linked to the surface temperature response when it is filtered or weighted by climatological precipitation, which is a proxy for deep convection (Sobel et al., 2002; Flannaghan et al., 2014; Fueglistaler et al., 2015).

While the direct effect of CO_2 does not affect sea surface temperatures, previous work shows that it leads to a nearly uniform warming in the free troposphere (He and Soden, 2015; Wang and Huang, 2020). In the absence of surface warming and humidity change, the moist adiabat would predict no warming aloft and thus underpredict the temperature response to the direct effect of CO_2. However, changes in near-surface air temperature and relative humidity due to the direct effect of CO_2 can also impact overprediction. For example, an increase in surface relative humidity would increase the warming aloft.

We expect convective entrainment will lead to a weaker temperature response aloft than predicted by the moist adiabat because an entraining plume releases less latent heat aloft. Thus, in the presence of climatological entrainment the moist adiabat should overpredict the temperature response aloft. Previous work shows that zero-buoyancy bulk-plume models, which include the effect of climatological convective entrainment, successfully capture the increase of convective available potential energy to warming obtained in CRMs (Singh and O'Gorman, 2013; Seeley and Romps, 2015; Zhou and Xie, 2019). Increasing convective available potential energy with warming is consistent with the overprediction of upper tropospheric warming by the moist adiabatic response since convective available potential energy quantifies the deviation of the temperature profile from a moist adiabat. Furthermore, Po-Chedley et al. (2019) show the moist adiabatic response to multi-model mean surface warming in the RCP8.5 scenario of Coupled Model Intercomparison Project Phase 5 (CMIP5) overpredicts the temperature response aloft in individual models. They show that including the effect of entrainment via the bulk-plume model of Romps (2016) better captures the RCP8.5 temperature response. However, the influence of climatological entrainment on the temperature response to increased CO_2 in GCMs has not been examined

in detail.

Here I quantify the moist adiabatic temperature response to increased CO_2 and show it overpredicts the modeled temperature response across the CMIP5 model hierarchy. I quantify the importance of three mechanisms for the overprediction of the moist adiabat: 1) surface heterogeneity, 2) the direct effect of CO_2, and 3) convective entrainment. I quantify the importance of 1) and 2) using the CMIP5 model hierarchy and 3) by varying the parameterized entrainment rate in idealized aquaplanet simulations.

3.2 Methods

3.2.1 CMIP5 models

I examine the effect of surface heterogeneity and the direct effect of CO_2 on the tropical temperature response to increased CO_2 across the CMIP5 model hierarchy (Taylor et al., 2012). The CMIP5 models used in this study are listed in Table 3.2.1. To set the baseline from which the contributions of surface heterogeneity and the direct effect of CO_2 are quantified, I consider the total response (labeled as 'T') to increased CO_2 as follows.

At the complex end of the CMIP5 model hierarchy, I define the total response in AOGCMs as the response to quadrupling CO_2, which is quantified by

$$\text{abrupt4} \times CO_2 - \text{piControl.} \tag{3.1}$$

I average the last 30 years of the 150-year simulation to study the near-equilibrium response in AOGCMs.

In the mid-range of complexity of the CMIP5 model hierarchy I define the total response in atmospheric GCMs (AGCMs), which prescribe the SST based on observations (Gates, 1992), as the sum of the indirect (increased SST with fixed CO_2) and direct (fixed SSTs with quadrupled CO_2) effects of increased CO_2. The indirect effect is quantified using two different

47

Table 3.2.1: Overprediction in % of the moist adiabat across the CMIP5 hierarchy for individual models used in this study. Overprediction of the moist adiabat associated with the total response to increased CO_2 is denoted as 'T'. Overprediction generally decreases as processes not included in the moist adiabat are removed such as surface-atmosphere decoupling in regions of climatological descent ('T−L') and the direct effect of CO_2 ('T−L−D'). Blank data denote models for which data was not available in the corresponding model configuration.

	AOGCM		AGCMp			AGCMu			AQUA		
	T	T-L	T	T-L	T-L-D	T	T-L	T-L-D	T	T-L	T-L-D
ACCESS1-0	10.6	7.6	−	−	−	−	−	−	−	−	−
ACCESS1-3	27.5	23.2	−	−	−	−	−	−	−	−	−
bcc-csm1-1	23.1	11.6	19.4	5.9	1.4	22.8	12.3	7.4	−	−	−
bcc-csm1-1-m	32.3	29.3	−	−	−	−	−	−	−	−	−
BNU-ESM	27.1	27.9	−	−	−	−	−	−	−	−	−
CanESM2	25.5	10.4	15.8	6.2	5.9	15.6	9.3	9.1	−	−	−
CCSM4	26.4	29.4	22.8	22.2	22.1	23.8	26.7	26.6	23.6	22.8	21.7
CNRM-CM5	46.9	46.2	40.3	39.5	32.1	40.2	39.8	31.4	52.0	51.5	43.0
CNRM-CM5-2	46.4	45.5	−	−	−	−	−	−	−	−	−
CSIRO-Mk3-6-0	28.0	9.6	−	−	−	−	−	−	−	−	−
FGOALS-g2	24.5	22.4	−	−	−	−	−	−	20.5	18.4	16.9
FGOALS-s2	35.5	24.6	−	−	−	−	−	−	−	−	−
GFDL-CM3	22.2	18.4	−	−	−	−	−	−	−	−	−
GFDL-ESM2G	31.4	30.5	−	−	−	−	−	−	−	−	−
GFDL-ESM2M	33.8	31.6	−	−	−	−	−	−	−	−	−
GISS-E2-H	23.8	19.8	−	−	−	−	−	−	−	−	−
GISS-E2-R	21.2	18.2	−	−	−	−	−	−	−	−	−
HadGEM2-ES	12.6	8.1	10.0	8.2	4.5	11.2	10.7	6.5	7.1	6.2	4.7
inmcm4	36.6	24.2	−	−	−	−	−	−	−	−	−
IPSL-CM5A-LR	27.1	21.0	21.0	11.0	8.6	21.1	21.5	19.5	22.4	21.8	21.8
IPSL-CM5A-MR	27.1	19.2	−	−	−	−	−	−	−	−	−
IPSL-CM5B-LR	13.4	6.1	12.3	11.0	−2.0	13.1	3.6	3.4	−	−	−
MIROC-ESM	8.2	−11.3	−	−	−	−	−	−	−	−	−
MIROC5	22.8	10.5	17.8	10.4	8.3	18.0	14.2	11.9	19.4	9.7	11.4
MPI-ESM-LR	16.5	11.1	16.0	9.6	1.8	18.5	13.1	4.4	−11.4	−4.3	−9.9
MPI-ESM-MR	16.9	10.0	19.6	13.0	4.4	21.3	16.2	6.6	−9.3	−4.6	−10.4
MPI-ESM-P	17.0	12.2	−	−	−	−	−	−	−	−	−
MRI-CGCM3	29.8	17.9	26.4	18.2	15.7	26.5	23.4	20.6	24.8	21.1	18.6
NorESM1-M	20.9	23.2	−	−	−	−	−	−	−	−	−
All model mean	25.3	19.2	20.1	13.0	9.3	21.1	17.3	13.4	16.6	15.9	13.1
AGCM-subset mean	23.7	16.6	20.1	13.0	9.3	21.1	17.3	13.4	16.1	15.5	12.6
AQUA-subset mean	24.8	19.5	21.7	16.5	12.2	22.6	20.7	15.9	16.6	15.9	13.1

CMIP5 simulations: 1) the response to patterned SST warming (amipFuture−amip) and 2) the response to uniform 4 K warming (amip4K−amip). Thus, the total AGCM response to patterened warming, hereafter AGCMp, is quantified by

$$(\text{amipFuture} - \text{amip}) + (\text{amip4} \times \text{CO}_2 - \text{amip}), \qquad (3.2)$$

and the total AGCM response to uniform warming, hereafter AGCMu, is quantified by

$$(\text{amip4K} - \text{amip}) + (\text{amip4} \times \text{CO}_2 - \text{amip}). \qquad (3.3)$$

I average over the entire 30 years of each AGCM simulation.

Finally, at the simple end of the CMIP5 model hierarchy I quantify the total response in aquaplanet (AQUA) simulations as the sum of the indirect effect of uniform 4 K warming and the direct effect of quadrupled CO_2, i.e.

$$(\text{aqua4K} - \text{aquaControl}) + (\text{aqua4} \times \text{CO}_2 - \text{aquaControl}). \qquad (3.4)$$

I average over the last 5 years of each AQUA simulation.

I remove the impact of surface-atmosphere decoupling in regions of climatological descent by averaging the response only over regions where ascent at 500 hPa exceeds −35 hPa/d, i.e. $\omega < -35$ hPa/d. Following Sherwood et al. (2014), this corresponds to the 75th percentile value in the multi-model mean climatology of the AOGCM (piControl) and AGCM (amip) simulations. The response after removing regions outside of large-scale climatological ascent is labeled as 'T−L'.

Finally, I remove the impact of the direct effect of CO_2 by subtracting the direct effect from the total response over regions of deep convection. Given the constraints of the CMIP5 archive I can only remove the direct effect from the AGCM and AQUA simulations [see equations (3.2)–(3.4)]. The response after removing regions outside of large-scale climatological

ascent and the direct CO_2 effect is labeled as 'T−L−D'.

3.2.2   GFDL AM2.1 aquaplanet GCM

In order to understand the importance of convective entrainment for the tropical tropospheric temperature response to surface warming I configure the GFDL AM2.1 aquaplanet GCM (hereafter GFDL) with the Relaxed Arakawa-Schubert (RAS) convection scheme (Moorthi and Suarez, 1992). In the RAS scheme, the Tokioka parameter (α) controls the minimum entrainment rate ($\epsilon_{\min}$) as follows:

$$\epsilon_{\min} = \frac{\alpha}{D}, \tag{3.5}$$

where D is the depth of the planetary boundary layer. This constraint only affects plumes that detrain above 500 hPa. Thus the Tokioka parameter controls the entrainment rate of deep convection only. In previous studies, α was varied to study the influence of convective entrainment on the Madden–Julian Oscillation (Tokioka et al., 1988), the Intertropical Convergence Zone (Kang et al., 2008), the El Niño–Southern Oscillation (Kim et al., 2011; Jang et al., 2013; Ham et al., 2013), and tropical clouds and precipitation (Lin et al., 2013). The default climatological value is $\alpha = 0.025$ in GFDL. To investigate the role of entrainment on the tropical temperature response, I perturb α from its default climatological value as follows: $\alpha = 0, 0.00625, 0.0125, 0.05,$ and 0.1. Increasing the Tokioka parameter beyond 0.1 does not further increase the entrainment rate. Thus, the range of bulk entrainment rates obtained here represent nearly the full extent of the entrainment rate regime that can be studied by perturbing the Tokioka parameter in GFDL.

I vary the Tokioka parameter in two configurations of the GFDL model: 1) the standard aquaplanet, hereafter GFDLaqua, configured with the same SST profile used in the CMIP5 AQUA simulations (specifically the Qobs SST profile as defined in Neale and Hoskins, 2000) and 2) rotating radiative-convective equilibrium (RCE) configured with a spatially uniform SST of 300 K, hereafter GFDLrce. The RCE configuration allows us to test the robustness

of the results in the absence of surface heterogeneity, which is a common idealized model configuration for the tropics (Wing et al., 2018a). For both configurations I investigate the response to a uniform SST warming of 4 K (GFDLaqua4K and GFDLrce4K) with fixed α. Following Tan et al. (2019) the GFDL aquaplanet uses RRTMG radiation and does not include the radiative effects of ozone and clouds.

Zero-buoyancy bulk-plume and spectral-plume models

I compare the relationship between overprediction of the moist adiabat and climatological entrainment in GFDLrce and GFDLaqua to zero-buoyancy bulk-plume and spectral plume models. The zero-buoyancy bulk-plume model is a simple 1-D model of a temperature profile that includes the effect of a single entraining plume in RCE. To compare the predictions of the zero-buoyancy bulk-plume models to GFDL, I diagnose the bulk-plume fractional entrainment rate ϵ using the bulk-plume continuity equation (see equation (7) in Romps, 2014):

$$\epsilon = \frac{1}{M}\left(\frac{\partial M}{\partial z} + d\right),\tag{3.6}$$

where z is height, M is the convective mass flux (kg m^{-2} s^{-1}) and d is the detrainment mass flux per unit height (kg m^{-3} s^{-1}). M and d are directly output from the RAS convection scheme. I vertically average ϵ over pressure from 850–300 hPa to quantify the mean strength of entrainment in the free troposphere. Here I compare the GFDL output to three different bulk-plume models. For Singh and O'Gorman (2013) I set the relative humidity to 85% to fit the relationship between overprediction and entrainment in GFDLrce and 80% to fit GFDLaqua. I vary $\hat{\epsilon}$ (where $\epsilon = \hat{\epsilon}/z$) to study how the strength of entrainment influences overprediction. For Romps (2014), I set the ratio of gross evaporation to gross condensation $\alpha = 0.80$ to fit GFDLrce and $\alpha = 0.75$ to fit GFDLaqua, and vary ϵ directly, which is constant with height. Finally, for Romps (2016), $\epsilon = a\gamma/\mathrm{PE}$ where γ is the fractional lapse rate of saturation specific humidity, a is a constant, and PE is precipitation efficiency. I set

PE = 1 for both GFDLrce and GFDLaqua and vary ϵ by varying a. Alternatively, when ϵ is varied directly, the Romps (2016) model behaves nearly identically to Romps (2014).

The spectral plume model of Zhou and Xie (2019), assumes a one-to-one relationship between the entrainment rate of a plume and its level of neutral buoyancy (z_d), i.e. $\epsilon[z_d]$. $\epsilon[z_d]$ depends on the tropopause height z_t and two fitting parameters ϵ_0 and k. As $\epsilon[z_d]$ is not directly output from the RAS scheme, I infer $\epsilon[z_d]$ in GFDL such that the following criterion is satisfied:

$$\overline{h}^*(z_d) = h_{\epsilon[z_d]}(z_d), \tag{3.7}$$

where $\overline{h}^*$ is the saturation moist static energy (MSE) in GFDL and $h_{\epsilon[z_d]}$ is the MSE of a plume with entrainment rate $\epsilon[z_d]$ according to the Zhou and Xie (2019) model. I convert $\epsilon[z_d]$ to pressure coordinates (i.e. $\epsilon[p_d]$) and average the entrainment rates of plumes that detrain between 850–300 hPa to quantify the mean strength of spectral entrainment rate in the free troposphere. I fit the GFDLrce climatology by setting $z_t = 14.61$ km, $k = 1.00$, and $\epsilon_0 = 0.33$ km^{-1} in the Zhou and Xie (2019) model. I fit the GFDLaqua climatology by setting $z_t = 16.02$ km, $k = 0.60$, and $\epsilon_0 = 0.20$ km^{-1}. To mimic the effect of varying the Tokioka parameter in the Zhou and Xie (2019) model, I vary the mean $\epsilon[z_d]$ by varying k while holding z_t and ϵ_0 fixed, which produces the best fit to the GFDL results (see Fig. 3.2.1).

3.2.3   Calculating the moist adiabat and its overprediction

I calculate the moist adiabatic temperature at each latitude and longitude by setting the initial condition of the rising parcel as the annual mean 2 m temperature, relative humidity, and surface pressure. For models where the 2 m fields are not available, I interpolate the three dimensional temperature and humidity fields to the surface pressure. Where the surface pressure is greater than the lowest pressure level of the vertical grid (1000 hPa), I linearly extrapolate from the 1000 hPa value. Similar results are obtained if the moist adiabat is computed using 950 hPa instead of 2 m fields (see Tables 3.2.2 and 3.2.3).
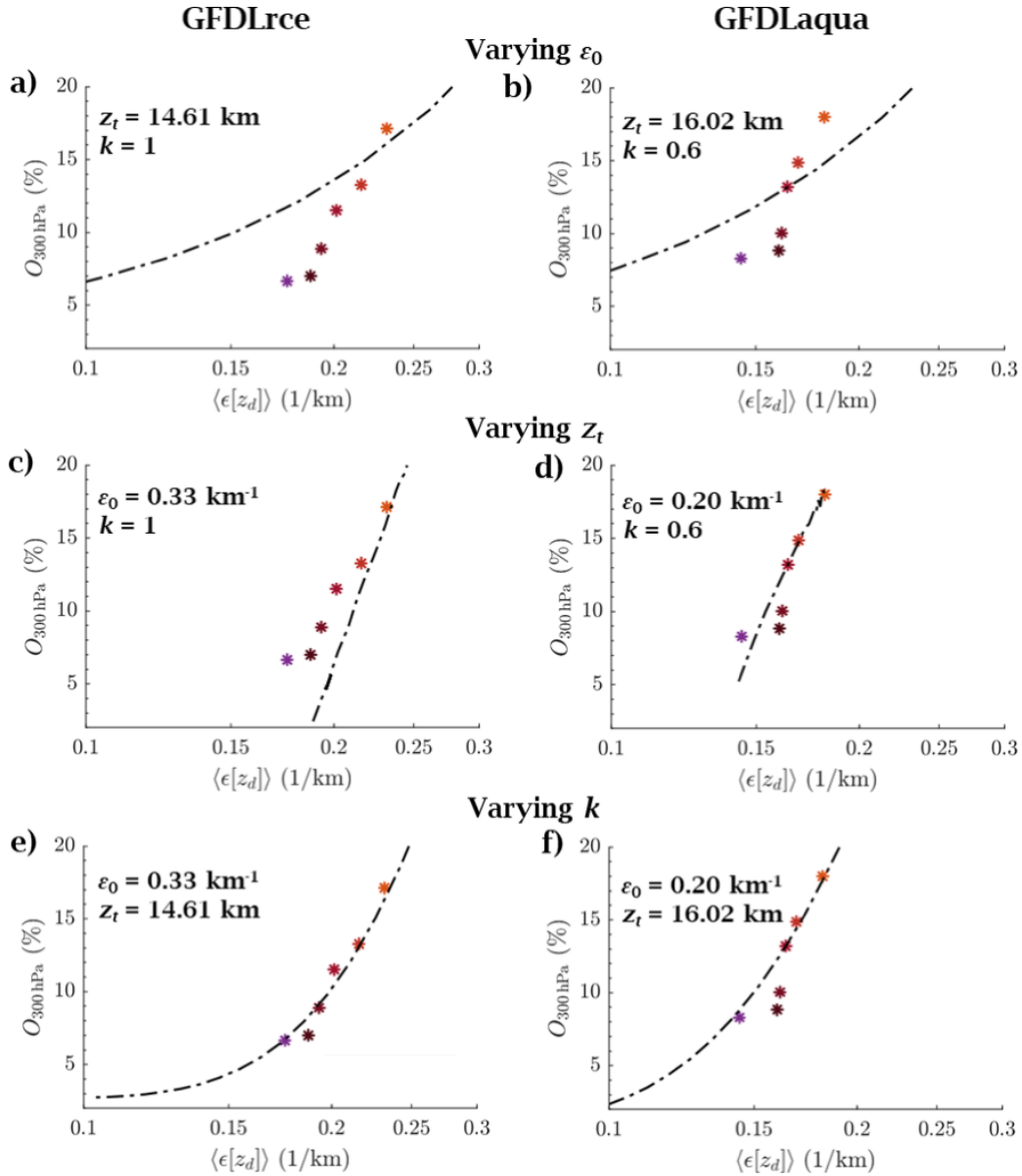
Figure 3.2.1: The relationship between spectral entrainment rate $\epsilon[z_d]$ and overprediction obtained by the Zhou and Xie (2019) model are shown as dash-dot lines compared to the a) GFDLrce and b) GFDLaqua results where $\epsilon[z_d]$ in the Zhou and Xie (2019) model is varied by varying ϵ_0 while holding z_t and k fixed. c) and d) are the same except $\epsilon[z_d]$ is varied by varying z_t while holding ϵ_0 and k fixed. For e) and f), $\epsilon[z_d]$ is varied by varying k while holding z_t and ϵ_0 fixed.

Table 3.2.2: Overprediction in % of the moist adiabat across the model hierarchy for various types of the moist adiabat. Three types of moist adiabatic lapse rates are shown here following the definitions in the AMS glossary. *Standard*: The limit of a moist pseudoadiabat when $r_v \ll 1$ (AMS, cited 2022: Moist-adiabatic lapse rate). *Pseudoadiabat*: Moist pseudoadiabat, which assumes that all condensates precipitate immediately (AMS, cited 2022: pseudoadiabatic lapse rate). *Reversible*: Reversible moist-adiabat, which assumes that all condensates remain in the parcel (AMS, cited 2022: reversible moist-adiabatic process). Furthermore, I test the sensitivity of overprediction to the boundary condition of the moist adiabat by using the temperature, relative humidity, and pressure at 2 m and at 950 hPa. Finally, I show overprediction for the default adiabat where latent heat of sublimation from freezing is ignored (NF), and a modified adiabat where freezing is included (F) following the European Centre for Medium-Range Weather Forecasts Integrated Forecast System Documentation Cycle 40 as in Flannaghan et al. (2014).

	AOGCM		AGCMp			AGCMu			AQUA		
	T	T-L	T	T-L	T-L-D	T	T-L	T-L-D	T	T-L	T-L-D
Standard											
2 m											
NF	25.3	19.2	20.1	13.0	9.3	21.1	17.3	13.4	16.6	15.9	13.1
F	25.5	18.2	18.6	9.9	6.2	20.1	14.6	10.6	16.0	14.8	12.0
950 hPa											
NF	20.6	14.7	17.4	11.4	8.1	17.5	16.8	13.2	15.9	16.2	12.9
F	22.5	15.9	18.2	11.1	7.7	18.7	16.8	13.1	17.6	17.6	14.1
Pseudoadiabat											
2 m											
NF	30.5	24.6	25.2	18.1	14.4	26.3	22.6	18.6	22.4	21.7	18.8
F	30.1	22.9	23.1	14.3	10.5	24.7	19.3	15.1	21.2	20.0	17.0
950 hPa											
NF	25.3	19.6	22.0	16.2	12.8	22.2	21.7	18.1	21.1	21.6	18.1
F	26.9	20.4	22.5	15.4	11.9	23.1	21.3	17.6	22.6	22.6	19.0
Reversible											
2 m											
NF	24.7	18.3	19.0	11.5	7.7	20.1	15.9	11.9	15.7	14.8	11.9
F	28.4	20.9	21.0	11.9	8.0	22.7	16.8	12.7	19.2	17.8	14.8
950 hPa											
NF	21.1	14.7	17.3	10.7	7.3	17.5	16.2	12.6	16.3	16.4	12.9
F	26.2	19.3	21.4	13.7	10.3	22.1	19.8	16.1	21.6	21.4	17.8

Table 3.2.3: Same as Table 3.2.2 but for GFDLrce and GFDLaqua configured with varying Tokioka parameters (α). The default Tokioka parameter used in the GFDL models is $\alpha = 0.025$. In general, overprediction decreases with decreasing α.

	GFDLrce						GFDLaqua					
α	0	0.00625	0.0125	0.025	0.05	0.1	0	0.00625	0.0125	0.025	0.05	0.1
Standard												
2 m												
NF	6.7	7.0	8.9	11.6	13.3	17.1	8.3	8.8	10.0	13.2	14.8	17.9
F	8.3	8.1	9.9	12.3	13.9	17.3	8.3	8.7	9.9	13.0	14.2	16.4
950 hPa												
NF	5.8	7.0	8.2	10.2	13.6	15.6	8.2	6.1	9.9	11.6	15.7	22.6
F	7.9	8.9	10.0	11.7	14.6	16.2	8.7	6.7	10.5	12.0	15.9	22.5
Pseudoadiabat												
2 m												
NF	11.9	12.3	14.2	16.8	18.7	22.7	13.8	14.3	15.5	18.7	20.5	23.7
F	13.1	13.1	15.0	17.3	18.9	22.3	13.2	13.7	14.9	17.9	19.1	21.9
950 hPa												
NF	10.9	12.1	13.3	15.3	18.8	21.0	13.5	11.5	15.3	16.9	21.2	28.3
F	12.7	13.8	14.9	16.4	19.5	21.3	13.7	11.7	15.5	17.0	21.0	27.7
Reversible												
2 m												
NF	6.8	6.9	8.7	11.1	12.7	16.4	7.5	8.1	9.3	12.4	13.9	16.9
F	12.0	11.8	13.6	15.8	17.2	20.3	11.3	11.8	13.0	15.8	16.9	19.7
950 hPa												
NF	6.4	7.4	8.5	10.3	13.6	15.4	8.0	6.1	9.8	11.4	15.4	22.1
F	11.9	12.8	13.9	15.2	18.6	19.9	12.3	10.3	14.1	15.5	19.3	25.9

I integrate the dry adiabatic lapse rate $\Gamma_d = \frac{g}{c_{pd}}$ up to the lifted condensation level (LCL). During this dry ascent, I assume that the water vapor mixing ratio is conserved. Above the LCL, I calculate temperature by integrating the moist-adiabatic lapse rate Γ_m following the definition in the American Meteorological Society glossary (American Meteorological Society, 2022).

$$\Gamma_m = \Gamma_d \frac{1 + \frac{L_v r_v}{RT}}{1 + \frac{L_v^2 r_v}{c_{pd} R_v T^2}}, \tag{3.8}$$

where L_v is the latent heat of vaporization, r_v is the vapor mixing ratio, R is the specific gas constant of dry air, R_v is the specific gas constant of water vapor, T is temperature, and c_{pd} is the isobaric specific heat capacity of dry air. This moist adiabat is a simplified form of a moist pseudoadiabat where it is assumed that all condensates precipitate out immediately and $r_v \ll 1$. Furthermore, I do not consider the effect of freezing (latent heat of fusion). Calculating the moist adiabat using alternative definitions such as the pseudoadiabatic and reversible adiabatic lapse rates, and including the ice phase does not significantly change the results (see Tables 3.2.2 and 3.2.3).

I quantify the overprediction O_p of the moist adiabatic response at a pressure level p as follows:

$$O_p = \frac{\Delta T_m(p) - \Delta T(p)}{\Delta T(p_s)} \tag{3.9}$$

where Δ denotes the difference between the warmer and control climates, $T(p)$ is the GCM temperature at pressure p, $T_m(p)$ is the moist adiabatic temperature at pressure p, and $T(p_s)$ is the surface temperature. I evaluate overprediction at 300 hPa following Fueglistaler et al. (2015). The tropical-mean overprediction is obtained by horizontally-averaging between 10°S and 10°N.

56

3.3 Results

3.3.1 Overprediction across the CMIP5 model hierarchy

When considering the total response to increased CO_2 (indirect plus direct effects), moist adiabatic warming systematically overpredicts the upper tropospheric warming across the CMIP5 model hierarchy (black symbols in Fig. 3.3.2). The multi-model mean overprediction of the total response is comparable across the model hierarchy, ranging from 25.3% for AOGCM to 20.1%, 21.1%, and 16.6% for AGCMp, AGCMu, and AQUA, respectively. The overprediction is largest in the upper troposphere (Fig. 3.3.1).

In what follows I focus on quantifying the impact of the following mechanisms on overprediction: 1) surface heterogeneity, 2) direct effect of CO_2, and 3) convective entrainment.

3.3.2 Surface heterogeneity

Overprediction is smaller in regions of climatological deep convection such as the western Pacific warm pool (see region inside red contour in Fig. 3.3.3a–c). Conversely, overprediction is large over the eastern Pacific, which is characterized by climatological descent (see region outside red contour in Fig. 3.3.3a–c). Overprediction over the eastern Pacific is smaller in AGCMu compared to AGCMp, suggesting that enhanced future surface warming in the eastern Pacific contributes to overprediction. Overprediction is zonally uniform in AQUA (Fig. 3.3.3d) and nearly meridionally uniform as most of 10°N/S is a region of climatological deep convection. Similar results are obtained when regions of climatological deep convection are defined using a precipitation threshold of 8 mm/d (see Fig. 3.3.4).

When averaged only over regions of deep convection, multi-model mean overprediction decreases by 6.1%, 7.2%, and 3.8% for AOGCM, AGCMp, and AGCMu, respectively (compare blue to black horizontal lines in Fig. 3.3.2 and see Fig. 3.3.5). This decrease is statistically significant at the 5% level when comparing changes among individual models (Table 3.3.1). The multi-model mean overprediction over regions of deep convection for AQUA decreases
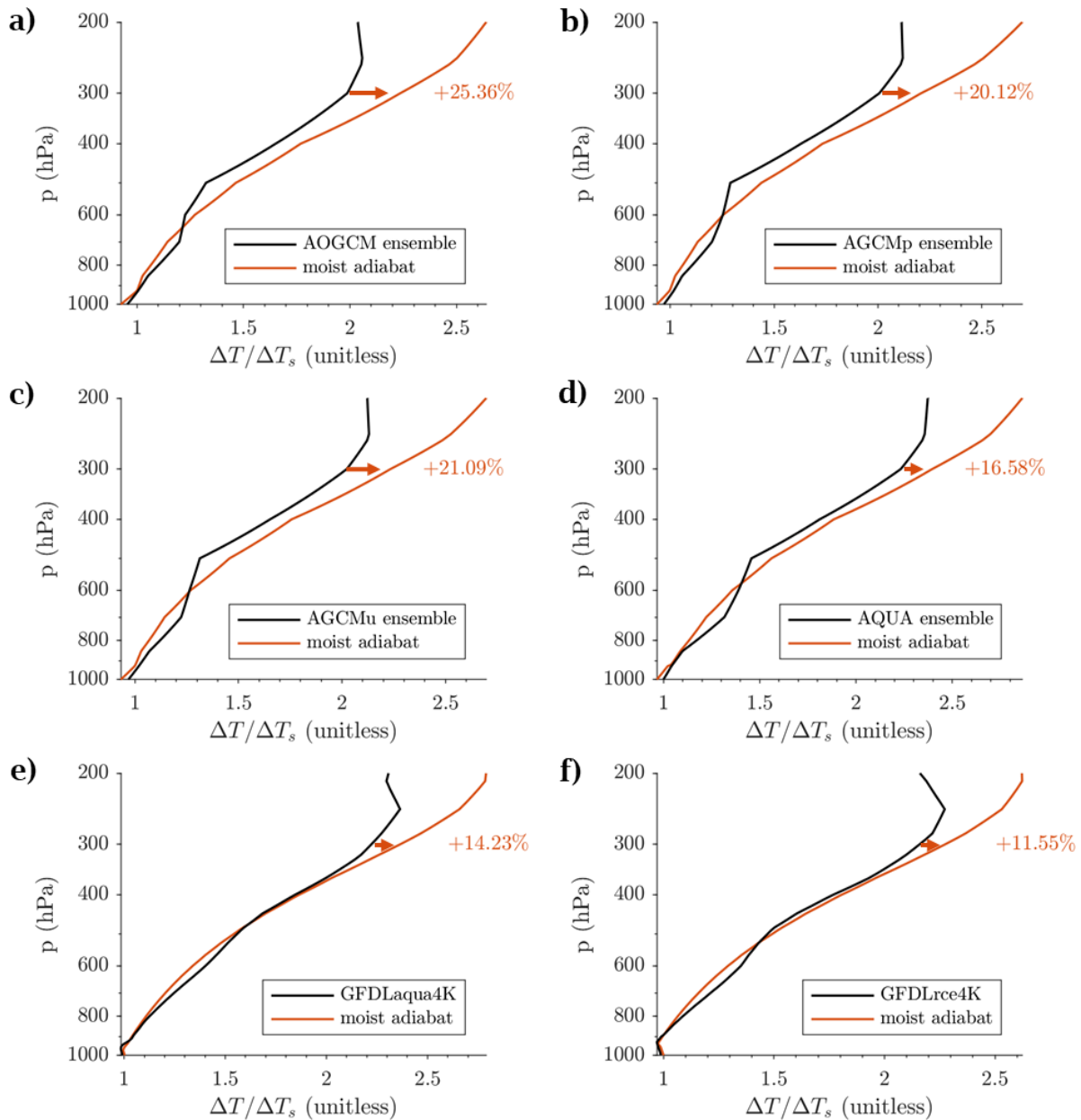
Figure 3.3.1: a) Vertical structure of the temperature response over the tropics (defined as 10°N/S) for the AOGCM multi-model mean (black) and the prediction based on a moist adiabat (orange). The moist adiabat overpredicts the AOGCM response by 25.34% at 300 hPa. b)–d) are the same for the AGCMp, AGCMu, and AQUA multi-model mean responses, respectively. e) and f) are the same for GFDLaqua4K and GFDLrce4K responses.
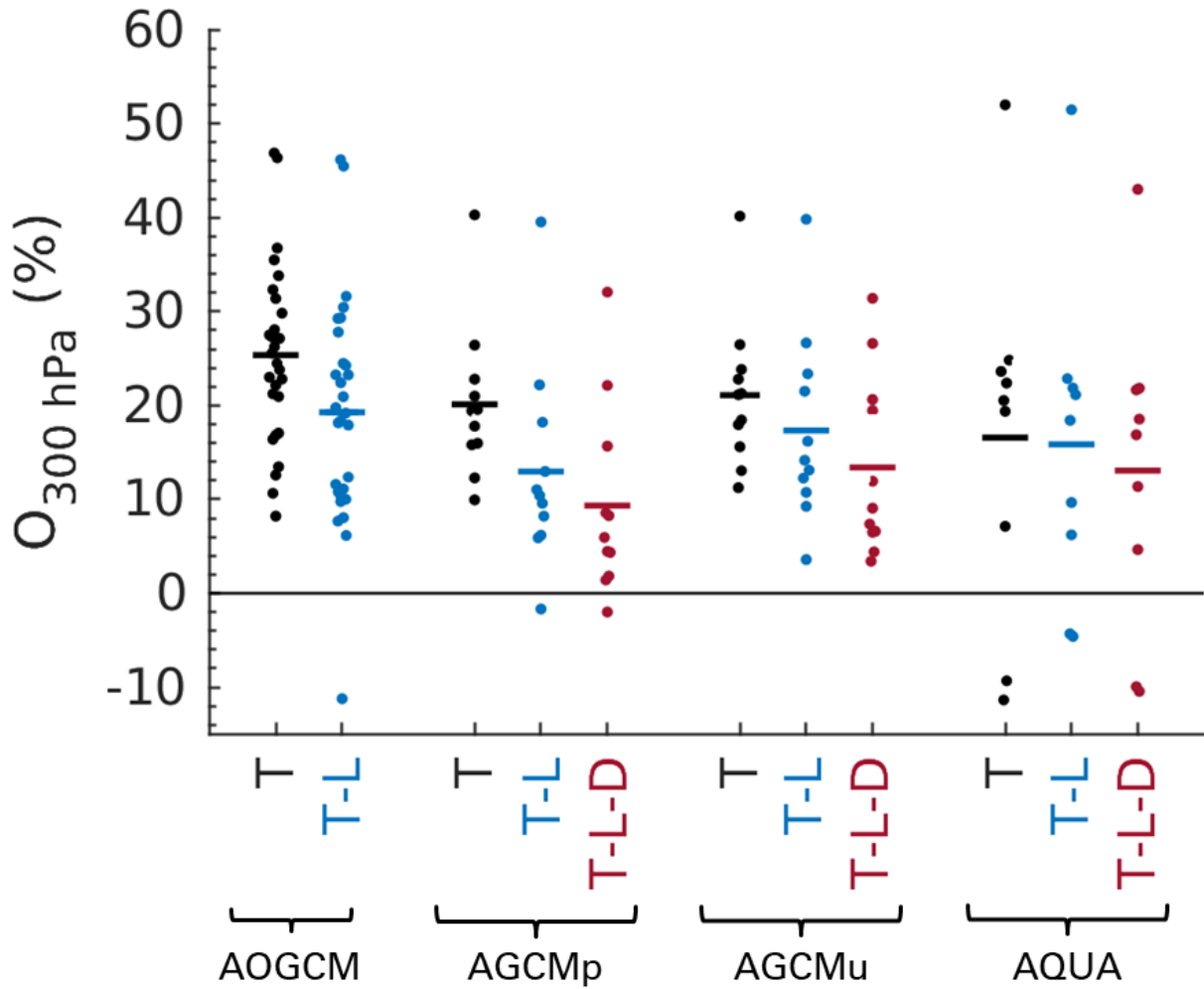
Figure 3.3.2: Overprediction across the CMIP5 model hierarchy. For each model configuration, black dots denote overprediction for the total response to increased CO_2 (labeled T) of individual models and the black horizontal line is the mean. Overprediction averaged only over regions of climatological deep convection (where $\omega < -35$ hPa/d at 500 hPa and labeled T-L) are shown in blue. Overprediction averaged over regions of deep convection and without the direct CO_2 effect are shown in red (labeled T-L-D).
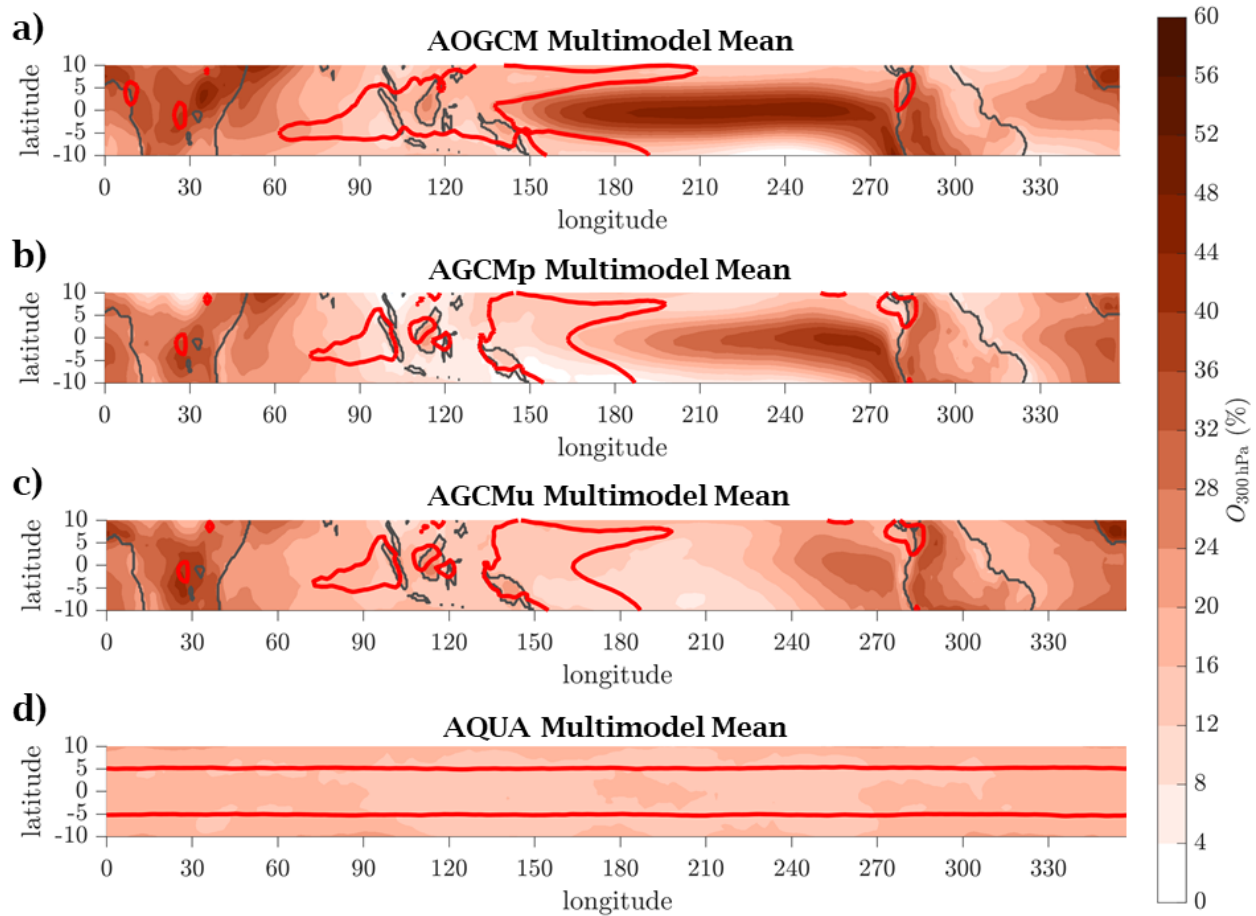
Figure 3.3.3: a) Spatial structure of the overprediction of the moist adiabat at 300 hPa in response to warming for the AOGCM multi-model mean. The red contour denotes the boundary of the multi-model mean climatological deep convection (where $\omega < -35$ hPa/d at 500 hPa). b)–d) are the same for AGCMp, AGCMu, and AQUA, respectively.

by 0.7%, and is not statistically significant because the 10°N/S region is dominated by deep convection (see Fig. 3.3.3d). Clearly, surface-atmosphere decoupling in regions of climatological descent has an influence on the tropical temperature response to increased CO_2, but accounting for this does not eliminate overprediction.

3.3.3 Direct effect of CO_2

When the response to the direct effect of CO_2 is removed, the multi-model mean overprediction over regions of deep convection further decreases by 3.6%, 3.9%, and 2.8% for AGCMp, AGCMu, and AQUA, respectively (compare red to blue horizontal lines in Fig. 3.3.2 and see
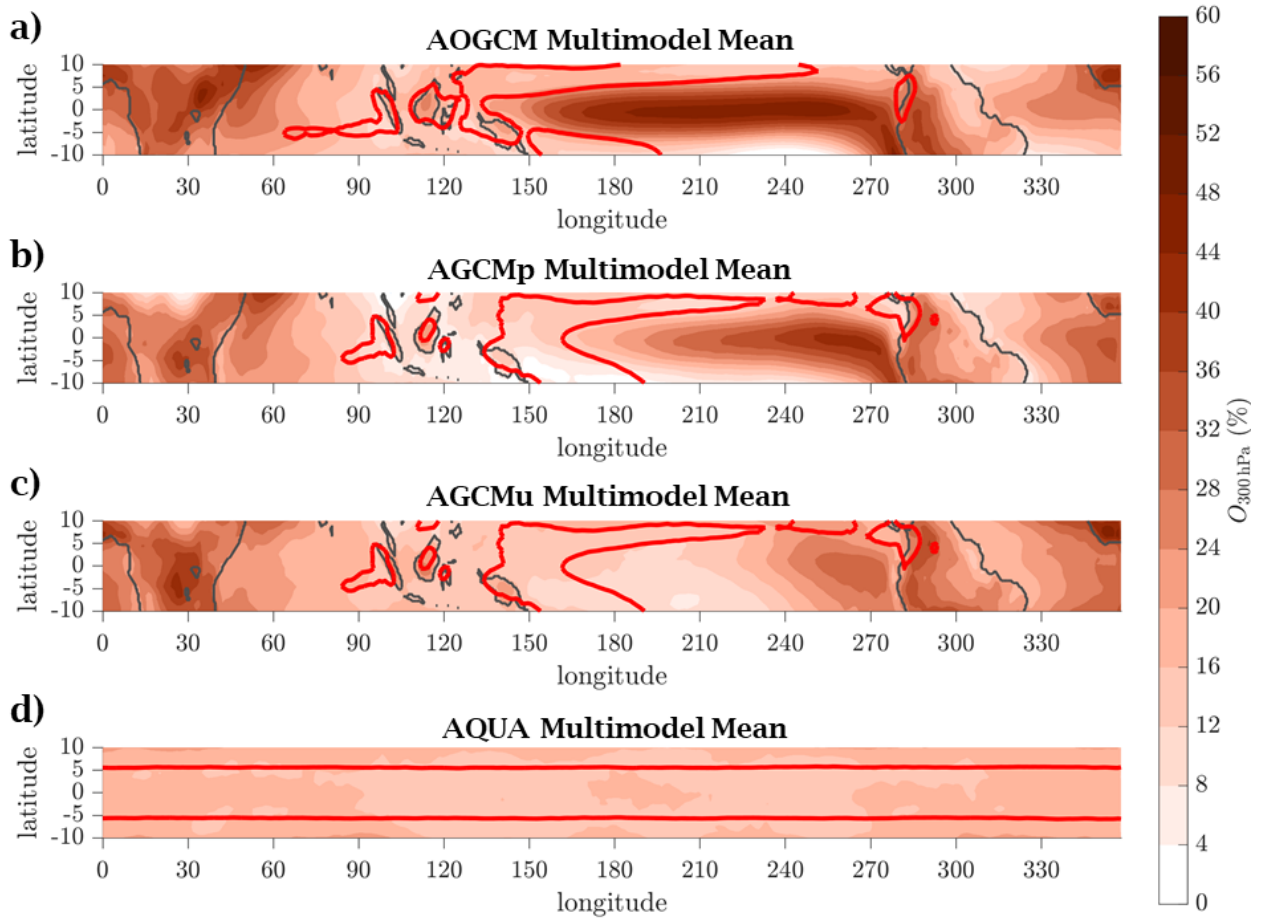
Figure 3.3.4: a) Spatial structure of the overprediction of the moist adiabat at 300 hPa in response to warming for the AOGCM multi-model mean. The red contour denotes the boundary of the multi-model mean climatological deep convection using precipitation of 8 mm/d as the criterion. b)–d) are the same for AGCMp, AGCMu, and AQUA, respectively.

Table 3.3.1: P-values of the T-test for the null hypothesis that the difference in mean overprediction averaged over $10°$N/S and averaged only over regions of strong mean ascent ($\omega < -35$ hPa/d) are indistinguishable from zero. The mean difference and the 5–95% confidence interval are also shown. The difference is statistically significant for model configurations that have zonally-asymmetric circulations. (p-value $< 5\%$, indicated in bold).

T - (T-L)	Lower Bound	Mean	Upper Bound	p-value
AOGCM	3.89	6.10	8.28	**0.0000**
AGCMp	4.03	7.15	10.28	**0.0005**
AGCMu	0.96	3.75	6.55	**0.0134**
AQUA	-2.94	0.72	4.38	0.6627

61
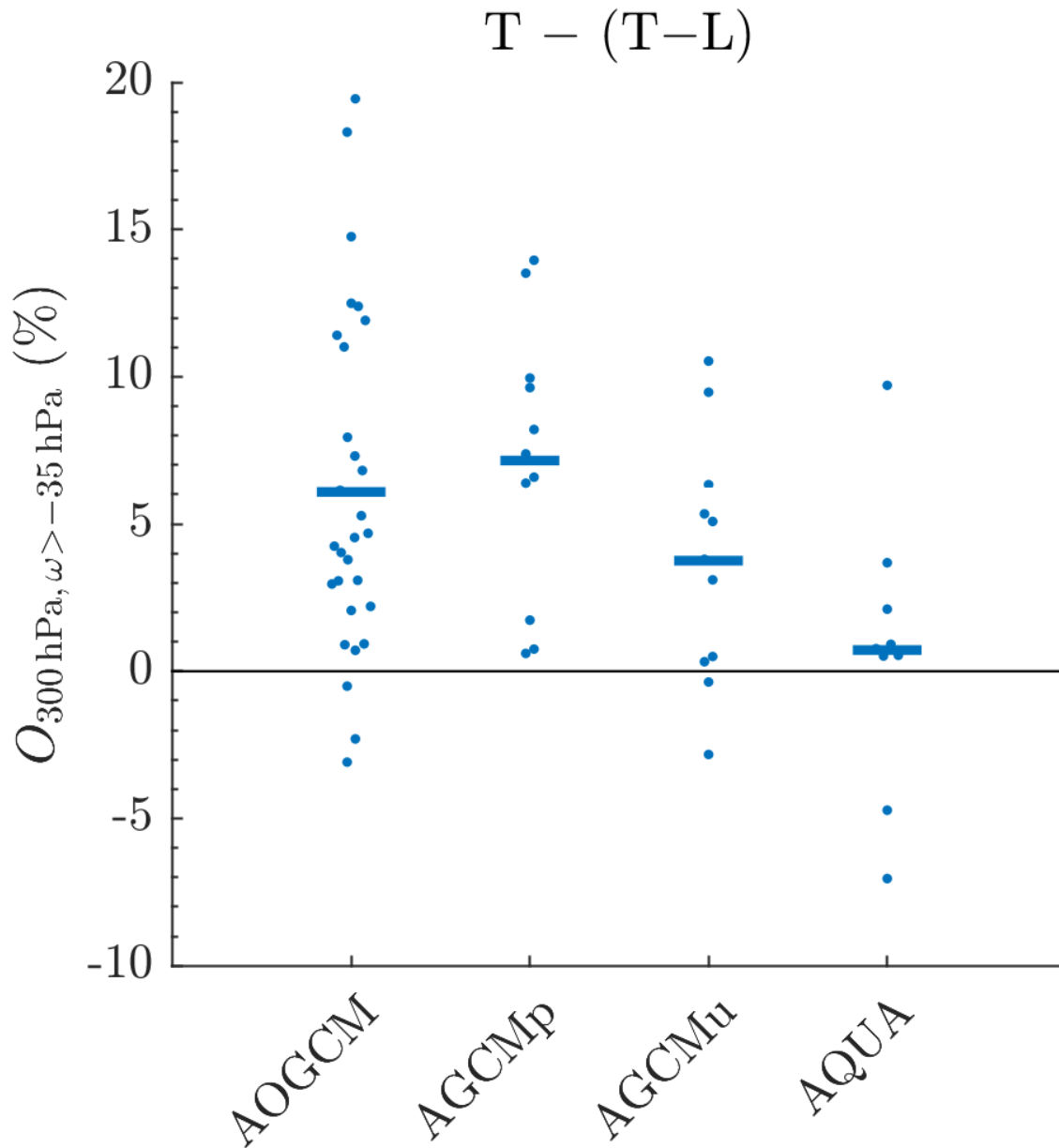
Figure 3.3.5: The difference between overprediction averaged over 10°N/S and overprediction averaged only over regions of climatological deep convection ($\omega < -35$ hPa/d) for each model across the model hierarchy (dots). The mean difference in overprediction is denoted by the horizontal line.

Table 3.3.2: P-values of the T-test for the null hypothesis that the difference in mean over-prediction between the combined indirect plus the direct CO_2 response and only the indirect CO_2 response are indistinguishable from zero. The mean difference and the 5–95% confidence interval are also shown. The difference is statistically significant for all model configurations (p-value < 5%, indicated in bold).

(T-L) - (T-L-D)	Lower Bound	Mean	Upper Bound	p-value
AGCMp	1.53	3.63	5.72	**0.0032**
AGCMu	1.54	3.94	6.33	**0.0043**
AQUA	0.31	2.80	5.28	**0.0317**

Fig. 3.3.6). A t-test shows that this decrease is statistically significant at the 5% level for all three model configurations (Table 3.3.2). As shown in previous work, the temperature response to the direct effect of CO_2 is vertically uniform in the free troposphere (compare vertical structure of black and orange lines in Fig. 3.3.7) and hence does not follow a moist adiabat. The overprediction associated with the direct CO_2 effect is driven by a small but significant warming of 2 m air temperature and is further amplified by an increase in the 2 m relative humidity (compare dashed to solid orange lines in Fig. 3.3.7).

3.3.4   Convective entrainment

With the default Tokioka parameter ($\alpha = 0.025$), the moist adiabat overpredicts the $\mathrm{T-L-D}$ response in GFDLrce4K and GFDLaqua4K by 11.6% and 13.2%, respectively (see Fig. 3.3.8 and Table 3.2.3). The magnitude of overprediction in GFDL is similar to that of the CMIP5 aqua4K multi-model mean.

When the Tokioka parameter is decreased, warming is enhanced aloft and approaches the moist adiabatic response in both GFDLrce (Fig. 3.3.9a) and GFDLaqua (Fig. 3.3.9b) configurations. When the Tokioka parameter is decreased from 0.1 to 0, overprediction decreases from 17.1% to 6.7% in GFDLrce and 17.9% to 8.3% in GFDLaqua. Overprediction in the GFDL model is significantly correlated with the logarithm of the diagnosed bulk plume (Fig. 3.3.9c,d) and the spectral plume fractional entrainment rate (Fig. 3.3.9e,f). The bulk plume models mostly capture this relationship for GFDLrce (see lines in Fig. 3.3.9c). Singh
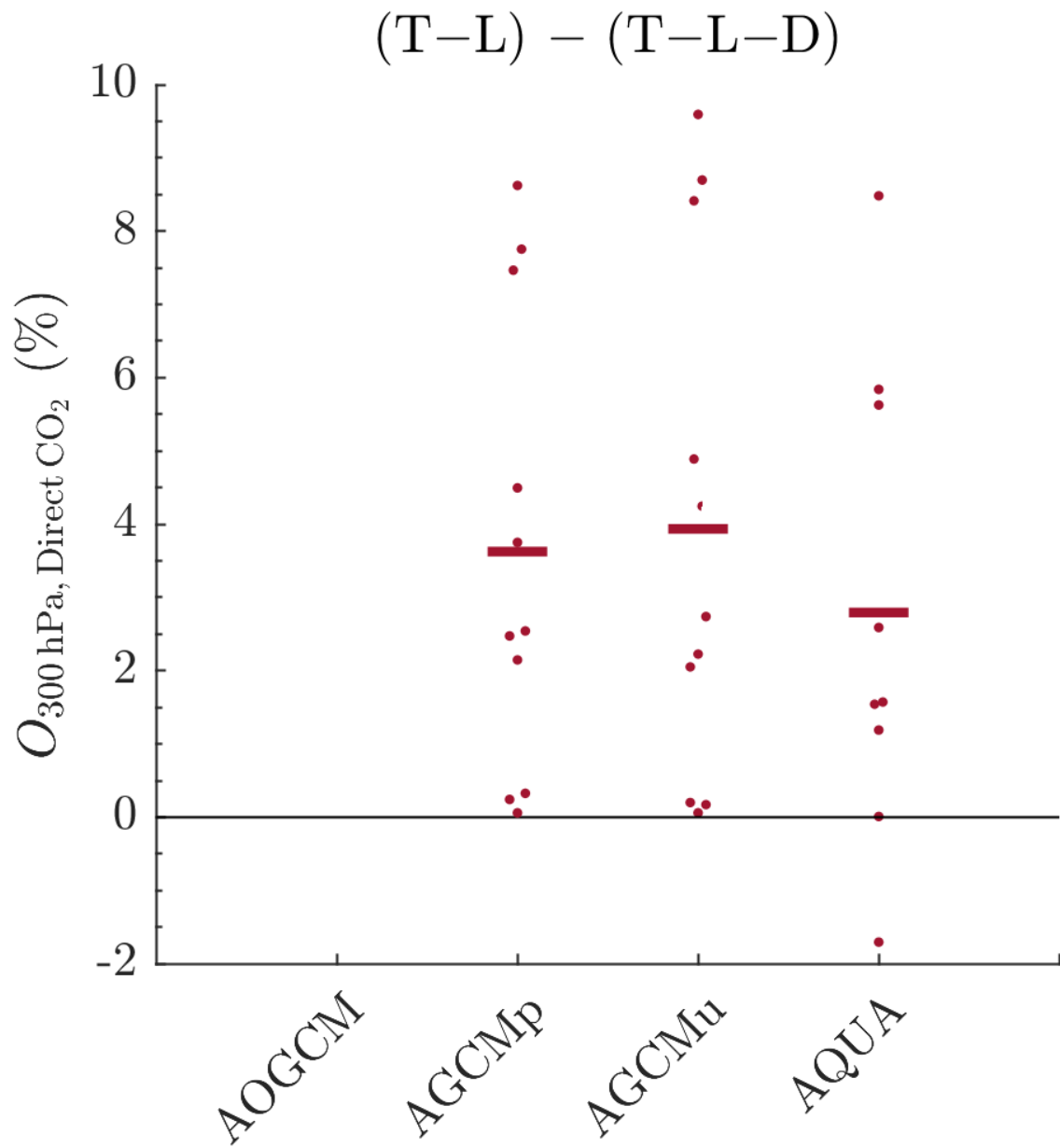
Figure 3.3.6: The difference in overprediction between the combined indirect plus the direct CO_2 response and only the indirect CO_2 response for each model across the model hierarchy (dots). The mean difference in overprediction is denoted by the horizontal line.
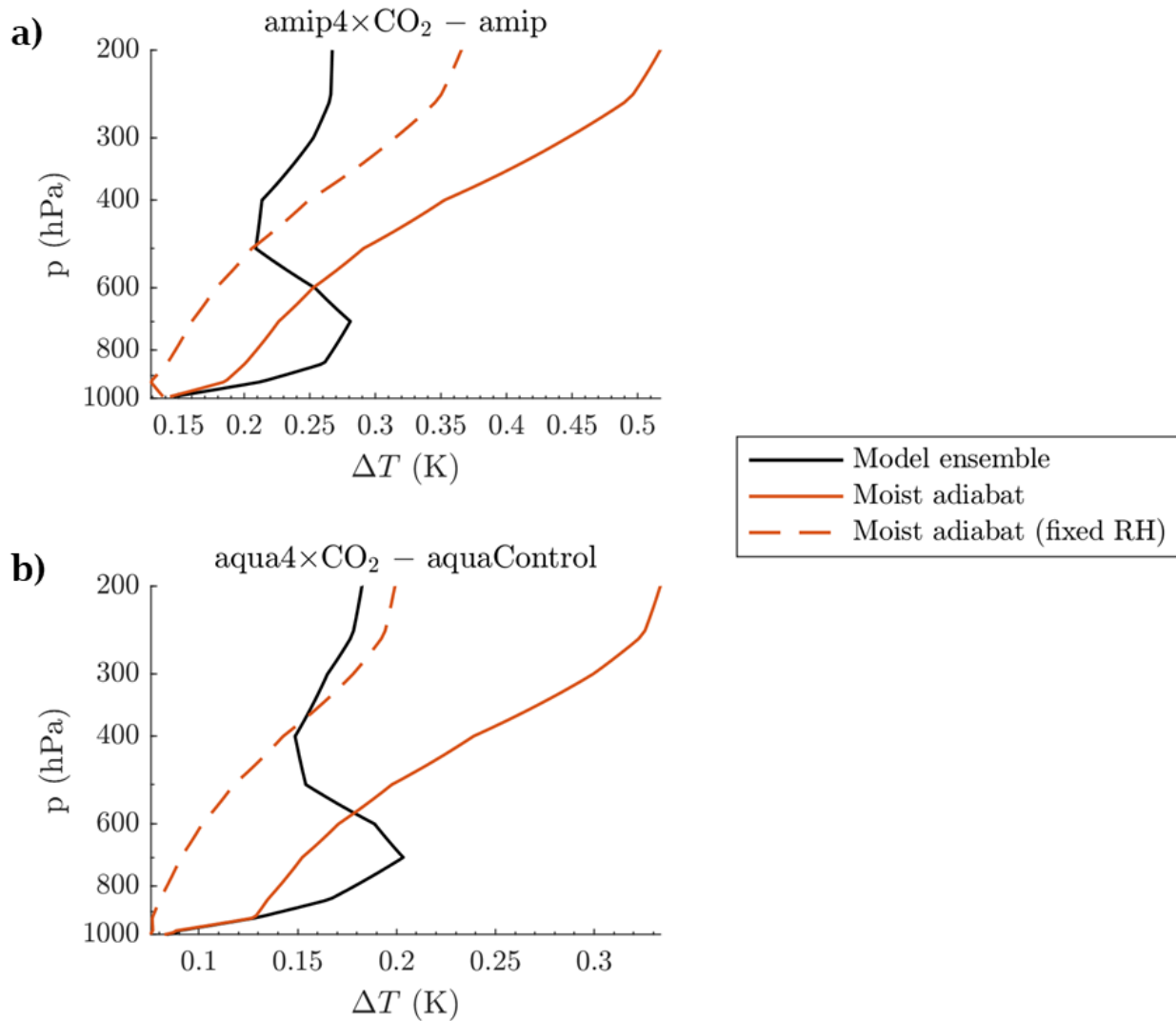
Figure 3.3.7: a) Vertical structure of the AGCM multi-model mean temperature response to the direct effect of CO_2 (black), the corresponding moist adiabatic prediction (solid orange), and the moist adiabatic prediction holding the 2 m relative humidity fixed at the climatological value (dashed orange). While the warming due to the direct effect of CO_2 is approximately uniform with height above the boundary layer in the multi-model mean, the moist adiabat predicts amplified warming aloft. b) is the same for AQUA.
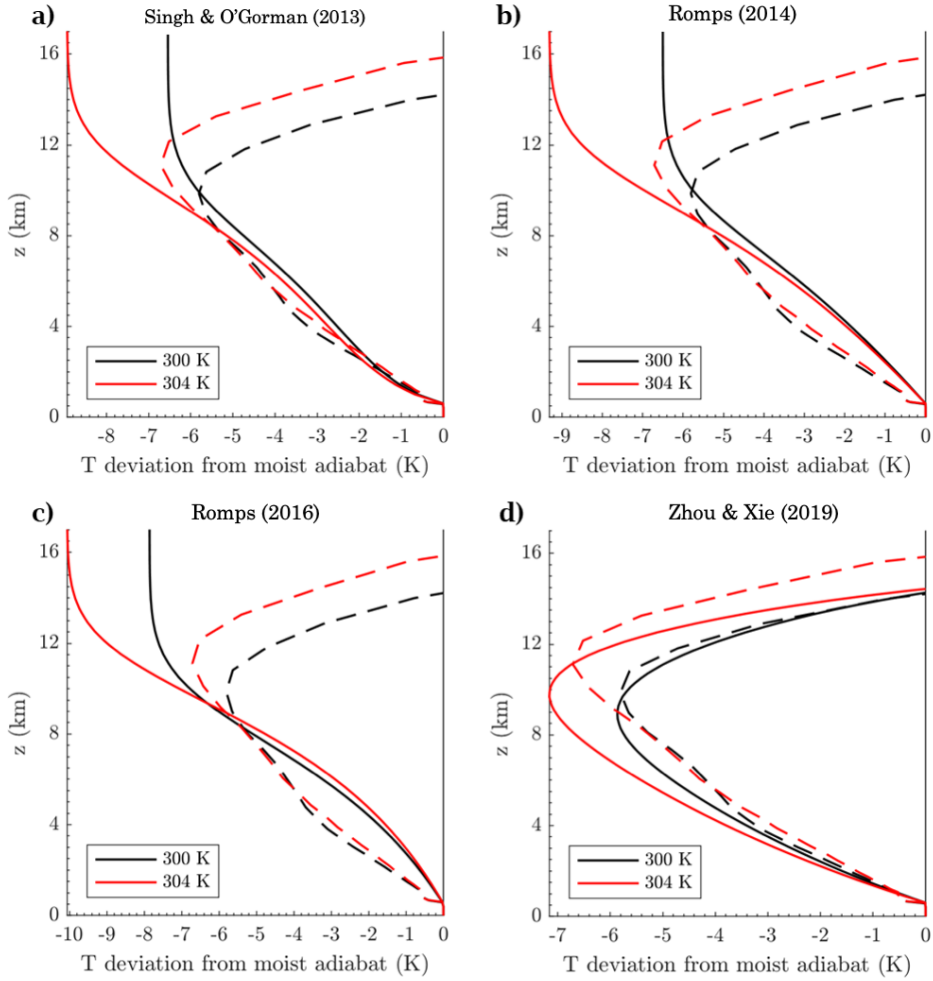
Figure 3.3.8: Temperature deviation from a moist adiabat in GFDLrce for a prescribed SST of 300 K (black dashed) and 304 K (red dashed). The corresponding predictions of the temperature deviations are shown for a) the Singh and O'Gorman (2013) zero-buoyancy bulk-plume model (solid) for $\hat{\epsilon} = 0.7$ and RH = 85%, b) the Romps (2014) zero-buoyancy bulk-plume model for $\epsilon = 0.3$ km^{-1} and $\alpha = 0.8$, c) the Romps (2016) zero-buoyancy bulk-plume model for $a = 0.25$ and PE = 1, and d) the Zhou and Xie (2019) spectral-plume model for RH = 65%, $z_t = 14.61$ km, $\epsilon_0 = 0.33$ km^{-1}, and $k = 1.00$.

and O'Gorman (2013) and Romps (2014) also capture this relationship for GFDLaqua (see lines in Fig. 3.3.9d), but Romps (2016) does not. The fit of the Romps (2016) model cannot be improved by tuning the PE parameter, which is already set to its maximum value of 1. The Zhou and Xie (2019) spectral plume model captures the relationship for both GFDLrce (see line in Fig. 3.3.9e) and GFDLaqua (see line in Fig. 3.3.9f).

3.4   Summary and Discussion

3.4.1   Summary

Here I investigated the accuracy of the moist adiabatic prediction of the tropical upper tropospheric temperature response to increased CO_2. I found that the moist adiabat over-predicts the multi-model mean tropical upper tropospheric warming at 300 hPa to increased CO_2 by 16.6–25.3% across the CMIP5 model hierarchy (black symbols in Fig. 3.4.1). I quantified the importance of three mechanisms, not included in the moist adiabat theory, to the overprediction: 1) surface heterogeneity, 2) the direct effect of CO_2, and 3) convective entrainment. Surface heterogeneity and the direct effect of CO_2 were quantified using the CMIP5 archive. The importance of climatological convective entrainment was quantified by varying the Tokioka parameter in idealized aquaplanet simulations. The conclusions are:

1. Surface-atmosphere decoupling in regions of climatological descent has a significant impact on overprediction. Overprediction is largest outside tropical regions of cli-matological deep convection defined by $\omega > -35$ hPa/d. Overprediction is smaller but non-zero in tropical regions of deep convection defined by $\omega < -35$ hPa/d. The contribution of surface-atmosphere decoupling in regions of climatological descent to overprediction ranges from 0.7–7.2% (difference between black and blue symbols in Fig. 3.4.1).

2. The direct effect of increased CO_2, which impacts the surface relative humidity and tropospheric temperature response through changes in radiative energy balance, trop-
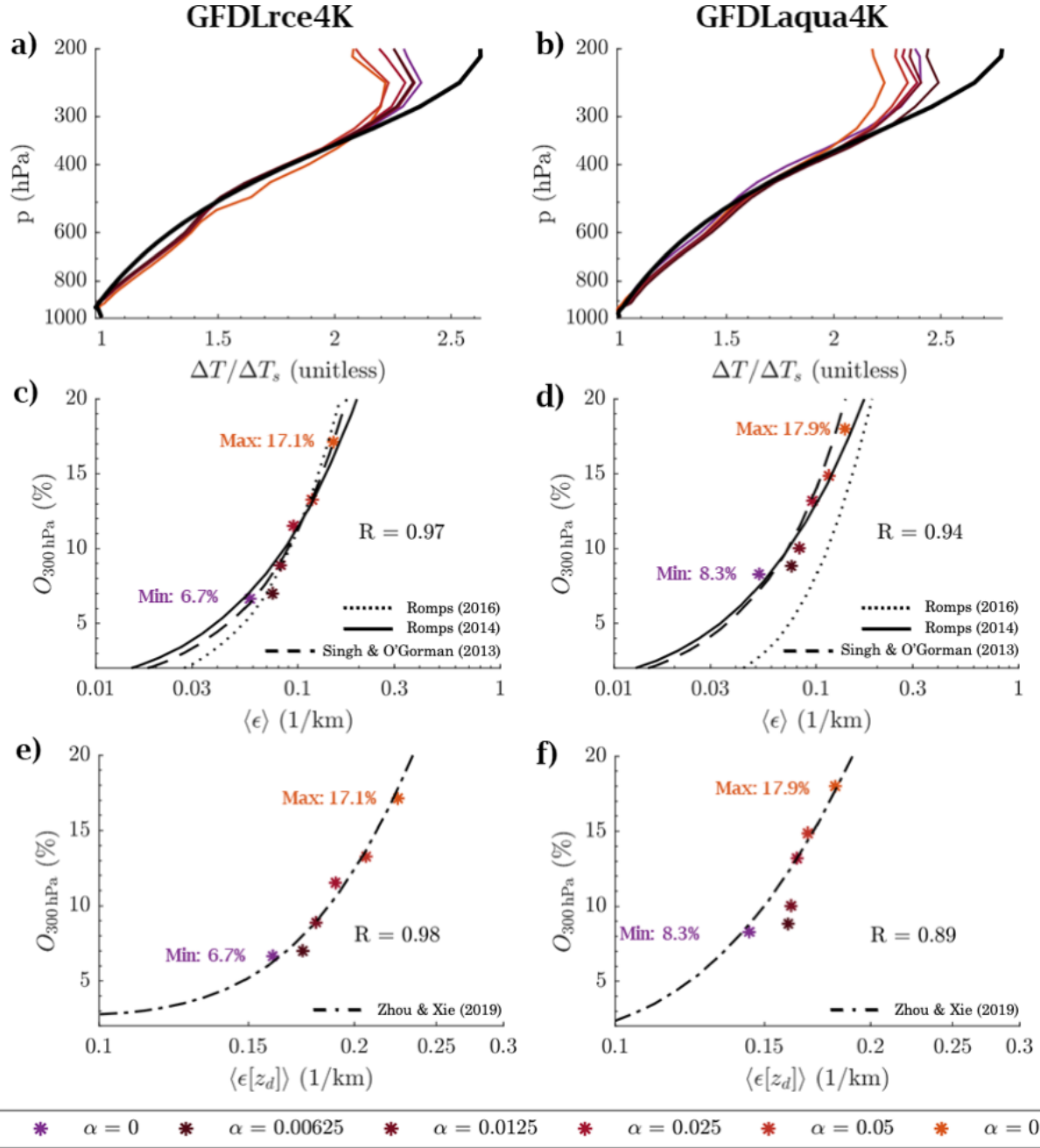
Figure 3.3.9: Temperature response in the GFDL aquaplanet when varying the Tokioka parameter α for the a) RCE (GFDLrce4K) and b) aquaplanet (GFDLaqua4K) configurations. The moist adiabatic response is shown as a thick black line for reference. Overprediction of the moist adiabat decreases with decreasing strength of the climatological vertically-averaged bulk-plume entrainment $\langle \epsilon \rangle$ for c) GFDLrce4K and d) GFDLaqua4K. e) and f) are similar except the x-axis shows the climatological spectral entrainment rates averaged within the free troposphere, $\langle \epsilon[z_d] \rangle$. The relationship between overprediction and entrainment predicted by zero-buoyancy bulk-plume models from Singh and O'Gorman (2013), Romps (2014), and Romps (2016), and the spectral-plume model from Zhou and Xie (2019) are shown as black lines in panels c–f.
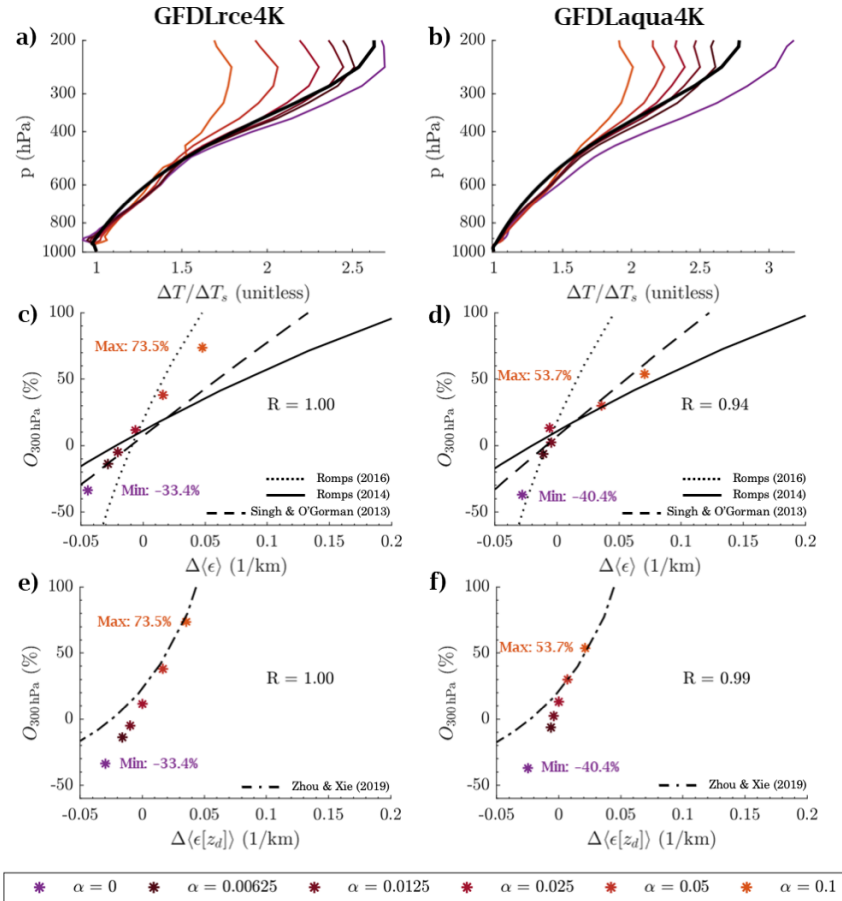
Figure 3.3.10: Temperature responses simulated in GFDL where the Tokioka parameter α is held fixed at 0.025 for the control climate and varied as shown only for the warm climate. The amplified warming in the upper troposphere strengthens when the entrainment weakens with warming in a) GFDLrce4K and b) GFDLaqua4K. The moist adiabatic response is shown as a thick black line for reference. Overprediction of the moist adiabat decreases with a weakening response of the vertically-averaged bulk-plume entrainment $\langle \epsilon \rangle$ with warming in both c) GFDLrce4K and d) GFDLaqua4K. e) and f) are similar except the x-axis is the vertically-averaged spectral entrainment rate $\langle \epsilon[z_d] \rangle$. The deviation as predicted by zero-buoyancy bulk-plume models of Singh and O'Gorman (2013), Romps (2014), Romps (2016), and the spectral plume model of W. Zhou and Xie (2019) are shown as black lines in panels c–f.

ical circulation, and precipitation, contributes to overprediction. The contribution of the direct CO_2 effect to overprediction ranges from 2.8–3.9% (difference between blue and red symbols in Fig. 3.4.1).

3. Parameterized convective entrainment contributes significantly to overprediction in the GFDL aquaplanet model configured with various Tokioka parameters. As the Tokioka parameter is decreased from 0.1 to 0, overprediction decreases by 10.4% for GFDLrce and 9.6% for GFDLaqua (difference between orange and purple symbols in Fig. 3.4.1). Overprediction is significantly correlated with the logarithm of the climatological entrainment rate in the GFDL model. The relationship between overprediction and the climatological entrainment rate in the GFDL model mostly follows the prediction of zero-buoyancy bulk-plume models of Singh and O'Gorman (2013), Romps (2014), and Romps (2016), and the spectral plume model of Zhou and Xie (2019).

3.4.2   Discussion

I showed that climatological convective entrainment contributes significantly to the overprediction of the moist adiabatic response to warming. The results are in agreement with Tripati et al. (2014) and Po-Chedley et al. (2019) who previously argued that overprediction of the moist adiabat of the temperature change since the LGM and to the RCP8.5 climates could be attributed to convective entrainment.

In this study, perturbing the Tokioka parameter in an aquaplanet model by an order of magnitude did not capture the full intermodel spread of overprediction in the AQUA CMIP5 model response. Some possible reasons that this experiment failed to capture the full spread of overprediction include: 1) the RAS convection scheme is not used by all CMIP5 aquaplanet models and other convection schemes may show greater sensitivity to entrainment, 2) the entrainment response to warming (rather than the climatological entrainment) may influence overprediction, and 3) convective processes other than entrainment may influence
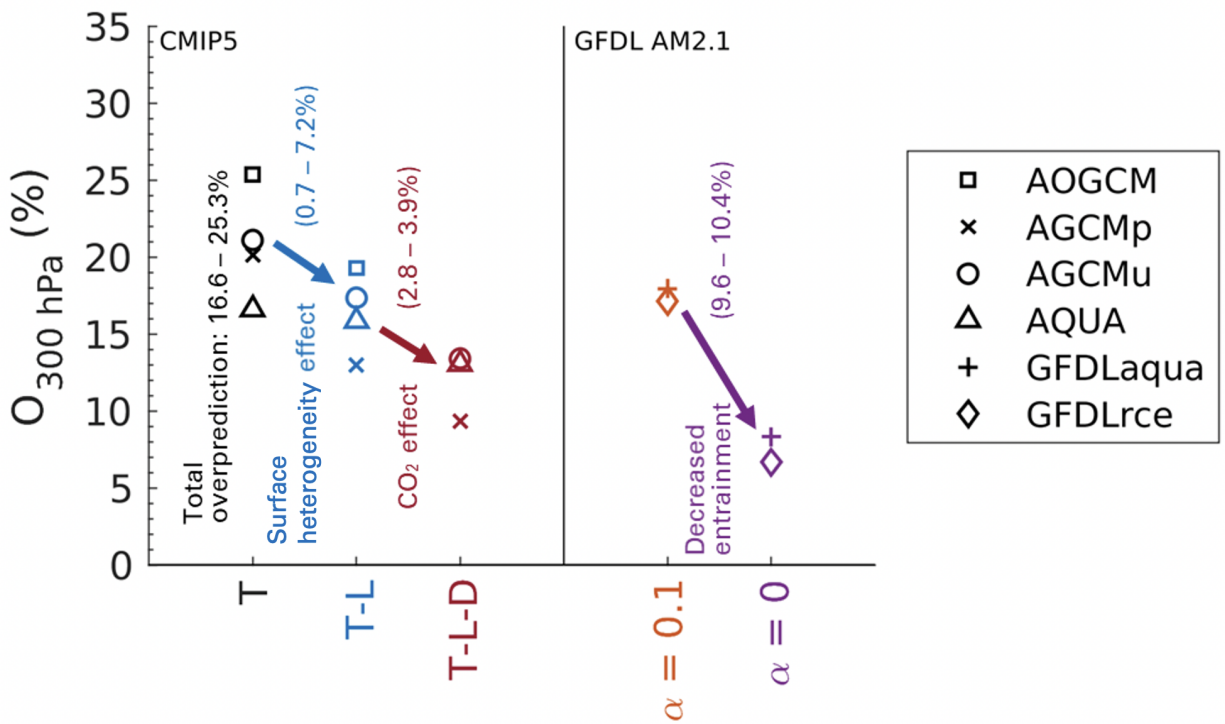
Figure 3.4.1: Summary of the contributions of surface heterogeneity, direct CO_2 effect, and convective entrainment on the overprediction of the moist adiabat response to increased CO_2. The surface heterogeneity effect is obtained from the difference in the CMIP5 multi-model mean overprediction averaged over the tropics ($\pm 10°$) and averaged only over regions of deep convection with the range indicating results across the model hierarchy. The CO_2 effect is quantified by removing the direct effect of CO_2 over regions of deep convection while retaining the indirect effect of CO_2 (SST increase). The range of the entrainment effect is obtained from decreasing the Tokioka parameter (α) from 0.1 to 0 in GFDLaqua and GFDLrce.

overprediction. The importance of 1) may be addressed by running experiments using a different convection scheme. The importance of 2) may be quantified by prescribing different entrainment rates in a warmer climate. Prescribing different Tokioka parameters in the control and warm climates of the GFDL aquaplanet leads to a large range of overprediction (-40.4%–73.5%, see Fig. 3.3.10). However, parameterized entrainment must be compared to more direct measures of entrainment such as those diagnosed from CRM simulations (Romps, 2010). Future work could also explore 3) by quantifying the influence of precipitation efficiency and cloud radiative effects. Fully understanding the relationship between entrainment and overprediction using theory and CRMs is an important area of future work.

This work highlights that while moist adiabatic adjustment provides a useful qualitative understanding of the tropical temperature response to increased CO_2, it has limitations as a quantitative theory. Incorporating the mechanisms identified here is important for improving the accuracy of the prediction. A full understanding of tropical lapse rate changes is critical to provide confidence in tropical climate predictions of the response to increased CO_2.

CHAPTER 4

THE TRANSIENT EMERGENCE OF A NEW WINTERTIME ARCTIC ENERGY BALANCE REGIME

4.1 Introduction

Quantifying the spatio-temporal structure of energy balance regimes is important to precisely define where and when the insights of RCE and RAE are expected to hold. In Chapter 2, I investigated mechanisms that control the existence of seasonal energy balance regime transitions. Here, I consider regime transitions that emerge on longer timescales, namely in response to anthropogenic forcing.

The modern Arctic climate in wintertime is characterized by sea ice cover, a strong surface temperature inversion, and the absence of deep convective activity (e.g., Hartmann, 2016). The modern Arctic is also characterized by a state of RAE (see Chapter 2 and Nakamura and Oort, 1988).

The wintertime Arctic is projected to undergo significant changes in response to anthropogenic forcing by the end of the century. Climate models project reduced sea ice concentration (Dai et al., 2019; Hankel and Tziperman, 2021), amplified surface warming (Manabe and Wetherald, 1975; Bintanja et al., 2011; Vallis et al., 2015), enhanced hydrologic cycle (Bengtsson et al., 2011; Bintanja and Selten, 2014; Pithan and Jung, 2021), vanishing surface inversion (Bintanja et al., 2011; Ruman et al., 2022), and emergence of deep convection (Huber and Sloan, 1999; Abbot and Tziperman, 2008b,a; Abbot et al., 2009; Arnold et al., 2014; Hankel and Tziperman, 2021). In Chapter 2, I showed that the wintertime Arctic climate transitions to the RCAE regime by the end of the century. Consistently, Arctic climate change has been previously described as an emergence of a new climate regime (Landrum and Holland, 2020).

The mechanisms that control the Arctic energy balance response to anthropogenic forcing

Tiffany A. Shaw and Malte F. Jansen contributed as co-authors of this chapter.

have been investigated in the literature. A key mechanism is reduced sea-ice concentration, which controls both the sea-ice albedo and lapse rate feedback. These positive feedbacks amplify surface warming and induce further sea-ice melting (Pithan and Mauritsen, 2014; Feldl et al., 2020). Sea-ice melting is closely coupled to energy balance regimes as melting leads to enhanced surface latent and sensible heating of the Arctic atmosphere (Taylor et al., 2018; Feldl et al., 2020; Shaw and Smith, 2022). The associated amplification of surface warming and the decrease in the meridional gradient of MSE is consistent with the projected decrease in advective heating into the Arctic (Armour et al., 2019; Feldl and Merlis, 2021; Shaw and Smith, 2022). Last, radiative cooling is projected to increase in the Arctic (Bintanja et al., 2011), and the rate of change of radiative cooling has been hypothesized to energetically constrain the Arctic precipitation response (Pithan and Jung, 2021). However, we currently lack a quantitative comparison of the mechanisms and their transient evolution.

Diagnosing energy balance regimes (using the metric R_1 defined in Chapter 2) is a new framework that can quantify the relative importance of different mechanisms (e.g., radiative cooling and advective heating responses) for both equilibrium and transient climate change. Energy balance regimes were previously shown to be useful for understanding the seasonal and latitudinal structure of tropospheric lapse rates including their equilibrium warming response. Thus, it may be a promising way to understand the mechanisms controlling the emergence of a new Arctic regime.

Here I investigate the mechanisms controlling transient Arctic climate change in CMIP5 models using the energy balance framework (Section 4.2.2). I first assess the usefulness of the energy balance framework as a way to quantify and understand Arctic climate change (Section 4.3.1). I then decompose changes in energy balance into contributions from radiative cooling and advective heating (Section 4.3.2). I use idealized models to further understand the mechanisms that influence the radiative cooling and advective heating responses (Section 4.3.3 and 4.3.4). Last, I summarize and discuss the results (Section 4.4).

74

Table 4.2.1: List of the 7 CMIP5 models that are used for the multimodel mean of the extended RCP8.5 run. Following Hankel and Tziperman (2021), GISS-E2-H and GISS-E2-R are omitted as outliers from the CMIP5 mean (deemed outliers because wintertime sea ice does not melt during the extended RCP8.5 run).

CMIP5
bcc-csm1-1
CCSM4
CNRM-CM5
CSIRO-Mk3-6-0
HadGEM2-ES
IPSL-CM5A-LR
MPI-ESM-LR

4.2 Methods

4.2.1 CMIP5 data

I quantify the transient response of wintertime (DJF) Arctic climate change using the extended RCP8.5 runs of Coupled Model Intercomparison Project Phase 5 (CMIP5, Taylor et al., 2012). The extended RCP8.5 run is an extension of the standard RCP8.5 high emissions scenario to the year 2300 (Meinshausen et al., 2011). I focus on the multimodel mean response of 7 models (Table 4.2.1) following Hankel and Tziperman (2021). I quantify relative changes $[\Delta(\cdot)]$ as the difference between the RCP8.5 run and the 1975–2005 climatology of the historical run $[\overline{(\cdot)}]$.

4.2.2 Energy balance regimes

I quantify energy balance regimes using the nondimensional number R_1 as defined in equation (2.3). I focus on R_1 in the Arctic, which I define as the area-weighted average of R_1 from 80° to 90°N. I choose 80°N as the lower bound of the Arctic domain as it corresponds to the equatorward extent of the zonal-mean RAE regime in the modern climate (see Fig. 2.3a).

4.2.3 Decomposing the radiative cooling response using an offline radiative transfer model

I quantify the mechanisms that control the transient radiative cooling response using the Rapid Radiative Transfer Model for General Circulation Models (RRTMG, Mlawer et al., 1997; Price et al., 2014). Specifically, I use RRTMG included in the Climlab Python package (Rose, 2018). RRTMG is configured with zero insolation consistent with polar night in the wintertime Arctic. Ozone and well-mixed radiatively active gases aside from CO_2 are prescribed according to the Aquaplanet Experiment protocol (Blackburn and Hoskins, 2013). I focus on the clear-sky radiative cooling response in RRTMG because the sign of its response is robust across all models (see Appendix 4.A) and dominates the full radiative cooling response in the multimodel mean (Fig. 4.3.3).

Clear-sky radiative cooling in RRTMG is computed as a function of three variables:

$$R_a = R_a(CO_2, T, q),$$
(4.1)

where $CO_2(t)$ is CO_2 concentration, $T(t, p)$ is the vertical temperature profile, and $q(t, p) = RHq^*$ is the vertical specific humidity profile, where RH is relative humidity, q^* is saturation specific humidity, t is time (in yearly DJF mean increments) and p is pressure. Both T and q are area-averaged from 80° to 90°N.

The total radiative cooling response in RRTMG $[\Delta R_a(\text{All})]$ is decomposed into contributions from 1) the direct CO_2 effect, 2) warming effect, and 3) relative humidity effect as follows:

$$\Delta R_a(\text{All}) = \underbrace{\Delta R_a(\Delta CO_2, 0, 0)}_{\text{Direct } CO_2 \text{ effect}} + \underbrace{\Delta R_a(0, \Delta T, \overline{RH}\Delta q^*)}_{\text{Warming effect}} + \underbrace{\Delta R_a(0, 0, \Delta RH\overline{q^*})}_{\text{Relative humidity effect}} + \text{Residual}.$$
(4.2)

The residual quantifies the contribution of higher-order interactions across changes in CO_2, T, and q.

To quantify the direct effect of increased CO_2, I vary CO_2 following the RCP8.5 protocol while holding T and q fixed at the historical climatology:

$$\Delta R_{\mathrm{a}}(\Delta CO_2, 0, 0) = R_{\mathrm{a}}(CO_2, \overline{T}, \overline{q}) - R_{\mathrm{a}}(\overline{CO_2}, \overline{T}, \overline{q}),\qquad (4.3)$$

where CO_2, T, and q correspond to the yearly CMIP5 DJF mean quantities from the RCP8.5 run and $\overline{(\cdot)}$ denote the 1975-2005 DJF climatology.

I quantify the warming contribution by varying temperature and specific humidity expected from holding relative humidity fixed:

$$\Delta R_{\mathrm{a}}(0, \Delta T, \overline{RH}\Delta q) = R_{\mathrm{a}}(\overline{CO_2}, T, \overline{RH}q^*) - R_{\mathrm{a}}(\overline{CO_2}, \overline{T}, \overline{q}).\qquad (4.4)$$

Finally, I quantify the specific humidity changes due to changes in relative humidity as follows:

$$\Delta R_{\mathrm{a}}(0, 0, \Delta RH\overline{q^*}) = R_{\mathrm{a}}(\overline{CO_2}, \overline{T}, RH\overline{q^*}) - R_{\mathrm{a}}(\overline{CO_2}, \overline{T}, \overline{q}).\qquad (4.5)$$

In summary, I use RRTMG to quantify the contribution of independent changes in 1) CO_2 concentration, 2) temperature and specific humidity holding relative humidity fixed, and 3) relative humidity on the clear-sky radiative cooling response. The discrepancy between the sum of 1)–3) and the total RRTMG clear-sky radiative cooling response is the residual, which is small (Fig. 4.3.3b).

4.2.4   Aquaplanet experiments

I configure the ECHAM6 aquaplanet (AQUA) with and without thermodynamic sea ice to test the importance of sea-ice melting on the transient response of Arctic energy balance regimes (Stevens et al., 2013; Shaw and Graham, 2020; Shaw and Smith, 2022). The zero-layer Semtner model (Semtner, 1976) is used for AQUA with thermodynamic sea ice (hereafter AQUAice). Grid cells are either completely ice free or ice covered (Giorgetta

et al., 2013; Salameh et al., 2018). I showed in Chapter 2 that AQUAice with a 40 m mixed layer depth captures the observed wintertime Arctic sea-ice thickness, energy balance regime, and inversion strength. Here, I initialize AQUAice from its control climate equilibrium ($pCO_2 = 348$ ppmv) and prescribe a transient evolution of CO_2 concentration following the RCP8.5 protocol starting in 1987 (when $pCO_2 = 348.6$ ppmv).

To test the role of sea-ice melting on the transient response of the Arctic to increased CO_2, I configure AQUA with a 40 m mixed layer and Q flux but no sea ice. The Q flux is imposed to reproduce the climatology (the last 20 years of a 40 year spin up run) of the AQUAice control climate. AQUA with an imposed Q flux (hereafter AQUAnoice, see Appendix 4.B for the derivation of the Q flux) reproduces the climatology of AQUAice in both the annual mean and seasonal cycle (compare blue and purple lines in Fig. 4.B.1 and 4.B.2).

4.3   Results

4.3.1   The transient energy balance response to anthropogenic forcing in the wintertime Arctic

The wintertime Arctic atmosphere in the modern climate is in the RAE regime ($R_1 = 1.06 \pm 0.06$, spread is quantified as the interquartile range across the CMIP5 models) and undergoes a regime transition to RCAE on year 2095 ± 54 (black line crosses to white region in Fig. 4.3.1a). R_1 decreases until year 2198 ± 29 (quantified as when R_1 is within 5% of the future stable value based on a logistic regression) and stabilizes in the RCAE regime corresponding to $R_1 = 0.70 \pm 0.07$.

The timing of the energy balance regime transition coincides closely with the disappearance of the surface temperature inversion as measured by the near surface lapse rate deviation from a moist adiabat (blue line, Fig. 4.3.1a). The modern Arctic is characterized by the existence of a strong inversion (near surface lapse rate deviation from a moist adiabat

exceeds 100%). The near surface lapse rate weakens until year 2186 ± 21 and stabilizes to the moist adiabatic lapse rate.

The R_1 response also coincides with the emergence of Arctic convection as measured by the convective precipitation fraction (blue line, Fig. 4.3.1b). The modern Arctic is characterized by the absence of convection (convective precipitation fraction is 0). Convective precipitation fraction increases until year 2180 ± 24 and stabilizes to 35%. Thus, the transient response of energy balance regimes is useful for understanding the disappearing inversion and the emerging convection in the Arctic.

4.3.2   The radiative and advective phases of the Arctic regime transition

To diagnose the physical mechanisms that control the transient R_1 response to anthropogenic forcing, I decompose $\Delta R_1(t) = R_1(t) - \overline{R_1}$ into radiative and advective components following the method used in Section 2.3.3:

$$\Delta R_1 = \overline{R_1} \left(\underbrace{\frac{\Delta(\partial_t m + \partial_y(vm))}{\partial_t m + \partial_y(vm)}}_{\text{advective}} - \underbrace{\frac{\Delta R_a}{R_a}}_{\text{radiative}} \right) + \text{Residual}. \tag{4.6}$$

The advective component [first term in equation (4.6)] quantifies the importance of the advective heating response and the radiative component [second term in equation (4.6)] quantifies the importance of the radiative cooling response. The residual quantifies the contribution of higher order terms.

The decomposition shows that there are two stages to the transient response of R_1: 1) the radiative phase prior to 2100 when enhanced radiative cooling dominates and 2) the advective phase after 2100 when reduced advective heating dominates (Fig. 4.3.2). The timing that separates the two phases is similar to when the RAE to RCAE regime transition occurs (i.e., the maroon line begins to change when black line crosses into white region in Fig. 4.3.2).

(a)

(b)
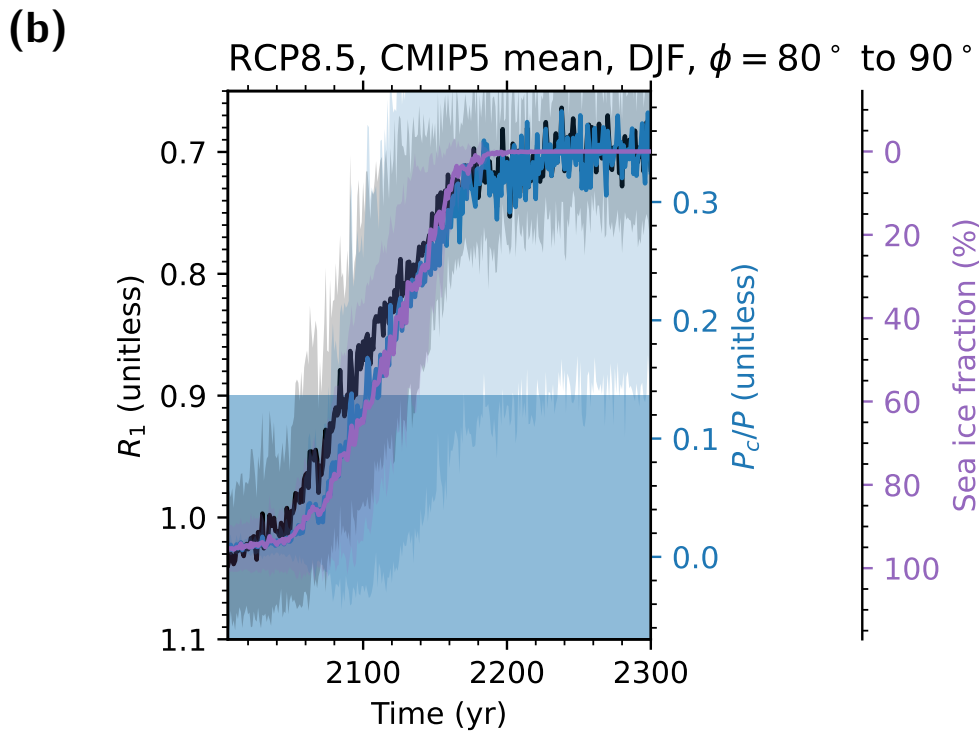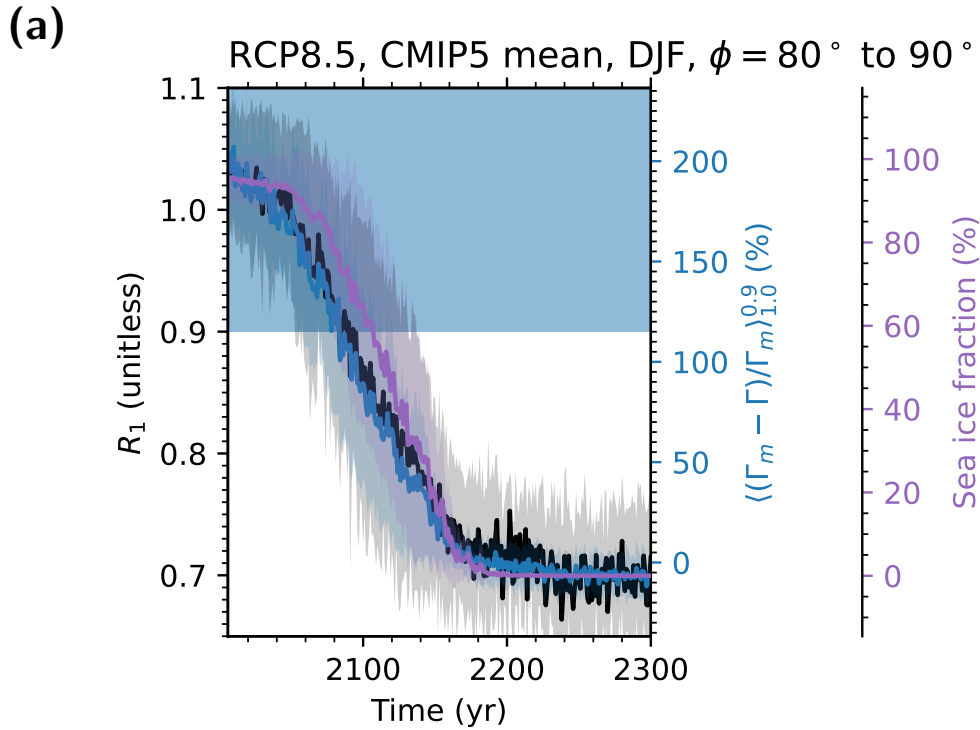
Figure 4.3.1: The response of wintertime (DJF) R_1 (a,b, black, left axis), sea ice fraction (a,b, purple, right axis), near-surface lapse rate deviation from a moist adiabat (a, blue, right axis), and convective precipitation fraction (b, blue, right axis) for the CMIP5 multimodel mean of the extended RCP8.5 run. The shading indicates the multimodel standard deviation.
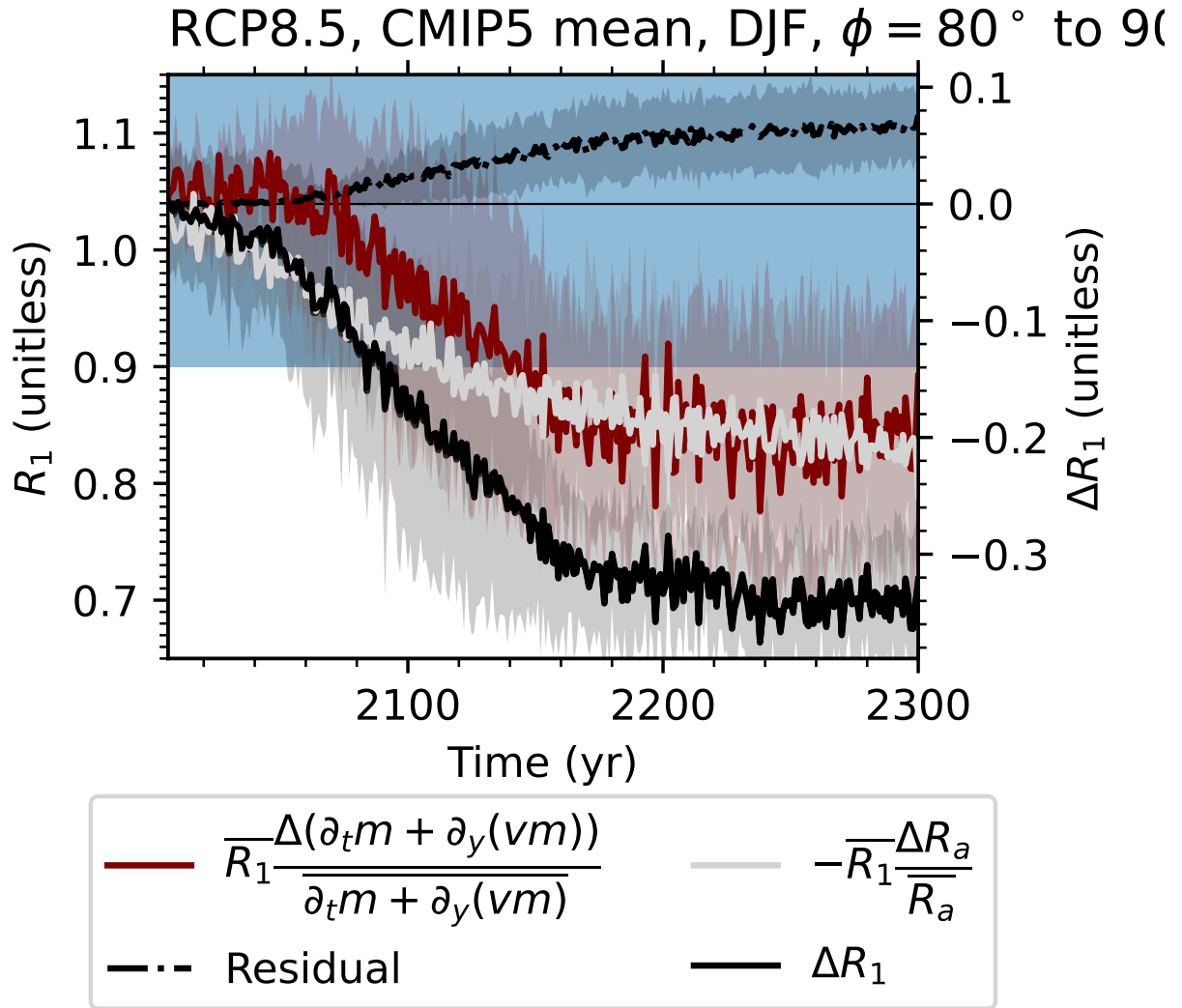
Figure 4.3.2: The wintertime (DJF) transient response (relative to the 1975–2005 historical mean) of R_1 (solid black) decomposed into the advective (red) and radiative (gray) components and the residual (dash-dot black) for the CMIP5 multimodel mean of the extended RCP8.5 runs. The shading indicates the multimodel standard deviation.

4.3.3 Decomposing the atmospheric radiative cooling response

Next, I focus on understanding the mechanisms controlling the atmospheric radiative cooling response. The wintertime radiative cooling response in the Arctic (gray line in Fig. 4.3.3) is entirely associated with the longwave cooling component (the greenhouse effect) as there is zero shortwave absorption during polar night (cyan line in Fig. 4.3.3). Enhanced longwave cooling is predominantly a clear-sky feature (dashed red line in Fig. 4.3.3). In the multimodel mean, the enhanced greenhouse effect from clouds (dotted red line in Fig. 4.3.3) also contributes to the total radiative cooling response. However the magnitude and the sign of the cloud contribution varies significantly across models (Fig. 4.A.4). As the cloud response is not robust, I focus on understanding the clear-sky longwave cooling response.

RRTMG captures the multimodel mean clear-sky longwave cooling response (compare the black and dashed red lines in Fig. 4.3.3) as well as in individual models (Fig. 4.A.4). I use RRTMG to decompose the radiative cooling response following equation (4.2)–(4.5). The direct effect of CO_2 [equation (4.3)] contributes to a small enhancement of radiative cooling (green line in Fig. 4.3.3b). GCMs project wintertime Arctic relative humidity decreases in response to anthropogenic forcing and this drying effect [equation (4.5)] contributes to a small reduction in radiative cooling (blue line in Fig. 4.3.3b). Enhanced radiative cooling is thus dominated by warming and the associated increase in water vapor holding relative humidity fixed [equation (4.4), compare orange and black lines in Fig. 4.3.3b]. Specifically, it is the greenhouse effect of water vapor that enhances radiative cooling (blue line in Fig. 4.3.4a). Warming in the absence of moistening reduces radiative cooling (orange line in Fig. 4.3.4a). While vertically uniform warming (Planck effect) enhances radiative cooling, the steepening of the lapse rate due to the bottom-heavy warming response (lapse rate effect) reduces radiative cooling (Pierrehumbert, 2011). The net effect of warming in the absence of moistening is a reduction in radiative cooling because the lapse rate effect is narrowly stronger than the Planck effect (compare dotted and dashed lines in Fig. 4.3.4b).
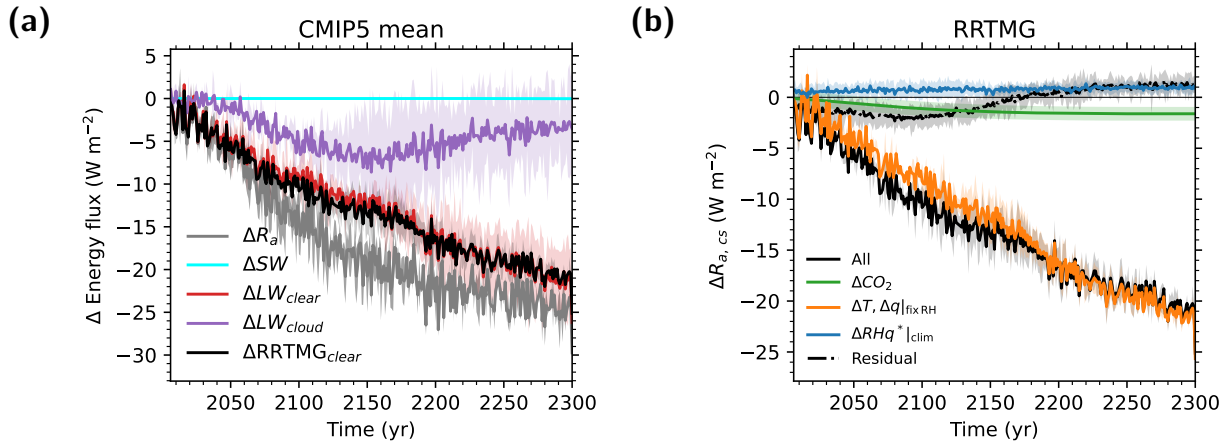
Figure 4.3.3: (a) Wintertime (DJF) radiative cooling response (gray) decomposed into short-wave (cyan) and longwave clear- (red) and cloudy-sky (purple) fluxes for the CMIP5 multimodel mean and the RRTMG clear-sky response (black). (b) The RRTMG clear-sky radiative cooling response is further decomposed into changes associated with the direct CO_2 effect (i.e. holding temperature and specific humidity fixed, green line), the warming effect including the associated moistening assuming fixed relative humidity (orange line), and the drying effect from a decrease in relative humidity (blue line). Shading denotes the multimodel standard deviation.
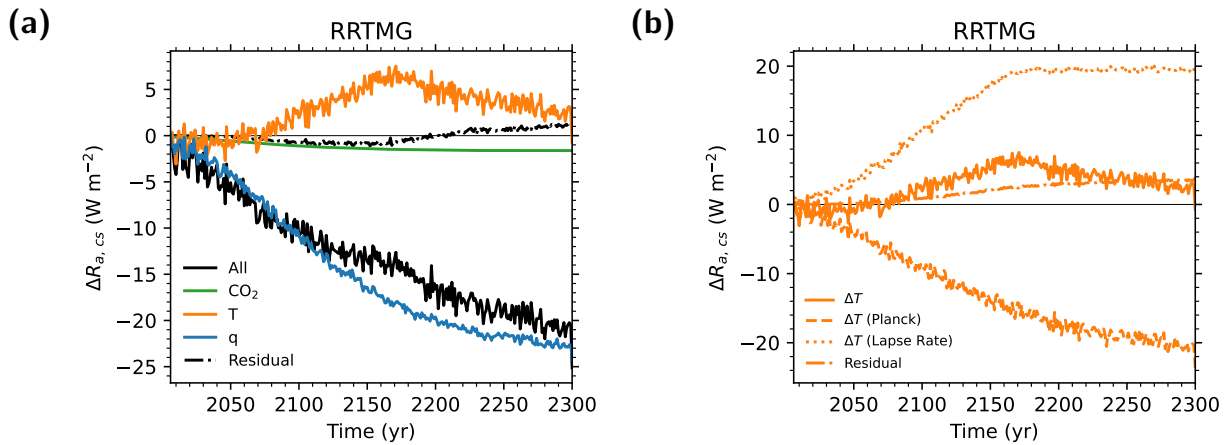
Figure 4.3.4: (a) Similar to Fig. 4.3.3b but showing an alternative decomposition that separates the contribution of warming (i.e. holding CO_2 and specific humidity fixed, orange line) and moistening (i.e. holding CO_2 and temperature fixed, blue line). (b) The warming contribution in the absence of moistening is further decomposed into contributions from vertically uniform warming (Planck effect, dashed orange) and deviations therefrom (lapse rate effect, dotted orange).

4.3.4 Testing the importance of sea-ice melting on the regime transition

I test the role of sea-ice melting by performing mechanism-denial experiments in an aquaplanet with and without sea-ice melting (see Section 4.2.4). Specifically, I quantify the transient response to RCP8.5 forcing in AQUAice (includes sea-ice melting) and AQUAnoice (no sea-ice melting).

In AQUAice, the wintertime climatology in the Arctic is in the RAE regime ($R_1 = 1.08$) and R_1 decreases in response to anthropogenic forcing. AQUAice captures the two-phased response of R_1 where R_1 initially follows the radiative contribution (gray line, Fig. 4.3.5a) then the advective contribution thereafter (marooon line, Fig. 4.3.5a) as seen in the CMIP5 response. The Arctic stabilizes in the RCAE regime ($R_1 = 0.80$). The RAE to RCAE regime transition in AQUAice coincides with the vanishing surface inversion and emergence of convective precipitation (Fig. 4.3.6). The regime transition occurs earlier than the CMIP multimodel mean consistent with an earlier onset of reduced sea-ice concentration (compare Fig. 4.3.6 and 4.3.1).

In AQUAnoice, the wintertime climatology in the Arctic is comparable to that in AQUAice (see Appendix 4.B) but there is no robust change in the Arctic energy balance (Fig. 4.3.5b). The Arctic energy balance remains in the RAE regime ($R_1 \approx 1$), the surface inversion persists (Fig. 4.3.7a), and convective precipitation remains absent (Fig. 4.3.7b). The lack of an R_1 response is a result of negligible long-term change in both radiative and advective contributions. The small radiative and advective responses in AQUAnoice and the fact that there is no Arctic amplification of surface warming (Arctic surface warming is 3.4 K in AQUAnoice compared to 32.1 K in AQUAice, compare Fig. 4.3.8a and b) suggest sea-ice melting plays a fundamental role in controlling the response of the Arctic energy balance to anthropogenic forcing. Sea-ice melting strongly influences the magnitude of Arctic surface warming which controls both the radiative cooling response (via the enhanced greenhouse effect from moistening associated with warming) and the advective heating response (via a decrease in meridional MSE gradient).

(a) AQUAice 40 m, DJF, $\phi = 80°$ to $90°$

(b) AQUAnoice 40 m, DJF, $\phi = 80°$ to $90°$

Legend (b):
- $\overline{R_1} \dfrac{\Delta(\partial_t m + \partial_y(vm))}{\overline{\partial_t m + \partial_y(vm)}}$ (dark red)
- $-\overline{R_1}\dfrac{\Delta \overline{R_a}}{\overline{R_a}}$ (gray)
- Residual (black dash-dot)
- ΔR_1 (black)

Legend (a):
- ΔR_1 (black)
- Residual (black dash-dot)
- $\overline{R_1} \dfrac{\Delta(\partial_t m + \partial_y(vm))}{\overline{\partial_t m + \partial_y(vm)}}$ (dark red)
- $-\overline{R_1}\dfrac{\Delta \overline{R_a}}{\overline{R_a}}$ (gray)
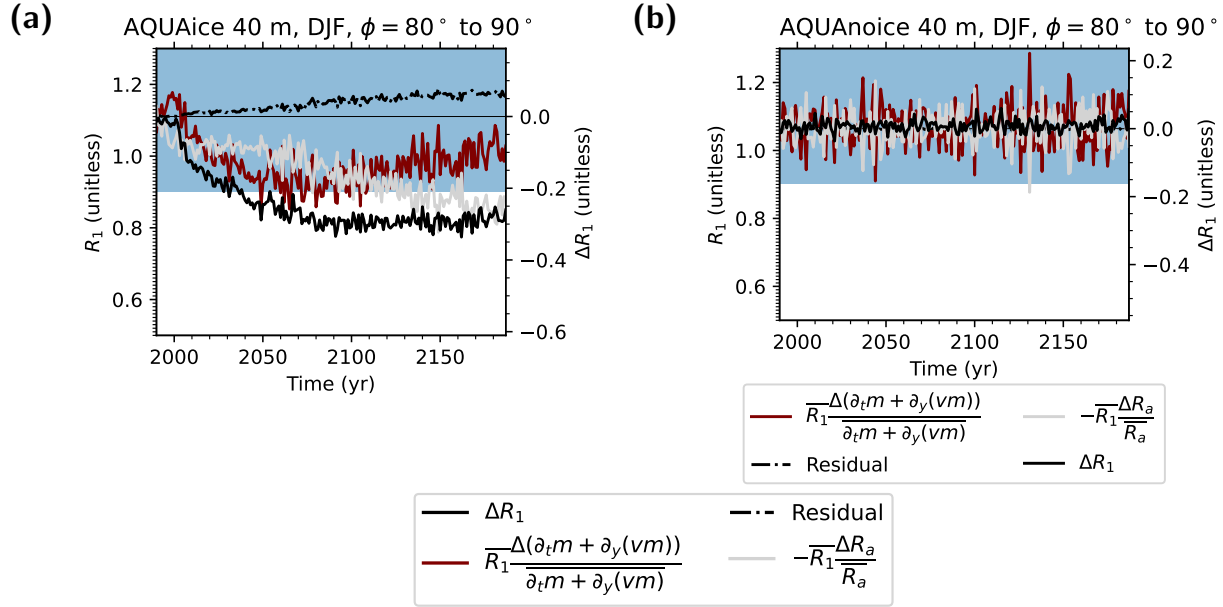
Figure 4.3.5: Same as Fig. 4.3.2 but for (a) AQUAice and (b) AQUAnoice.

4.4 Summary and Discussion

4.4.1 Summary

The wintertime Arctic (poleward of 80°N) in the modern climate is characterized by a strong near-surface inversion, the absence of convection, and complete sea-ice cover. The Arctic equilibrium response to anthropogenic forcing involves the vanishing of the inversion, emergence of convection, and reduced sea-ice concentration. These changes are coincident with a shift in the wintertime Arctic energy balance regime from RAE in the modern Arctic to RCAE in the future Arctic.

Here, I investigated the transient response of the wintertime Arctic climate in response to anthropogenic forcing using the energy balance regime framework. In this framework, Arctic energy balance regimes are quantified by the nondimensional number R_1, which measures the fraction of radiative cooling that is balanced by advective heating. I found the transient response of R_1 is quantitatively linked to the transient response of the vanishing surface temperature inversion, emergence of convective precipitation, and reduced sea-ice cover in

(a)
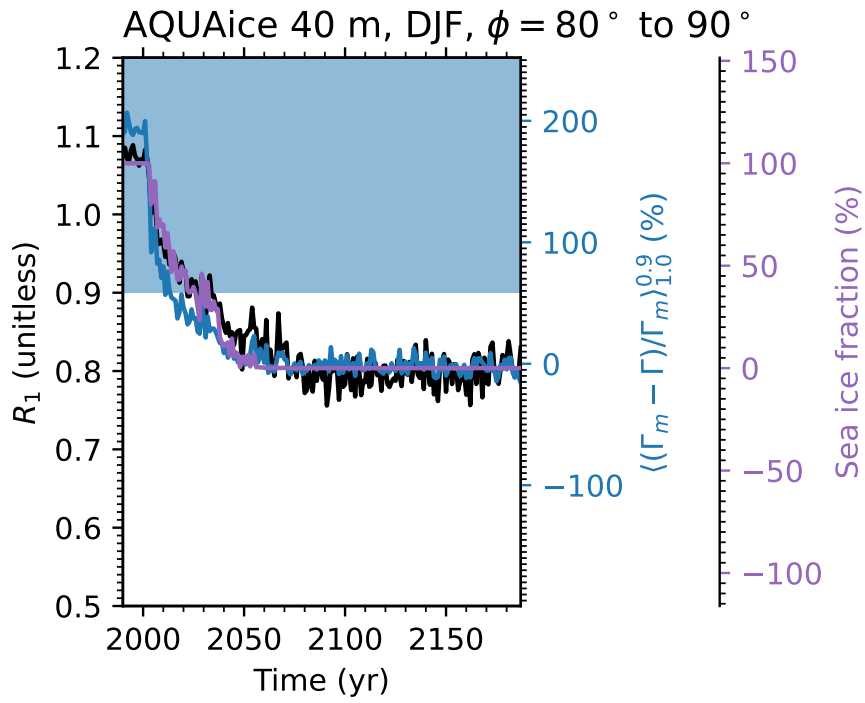
(b)
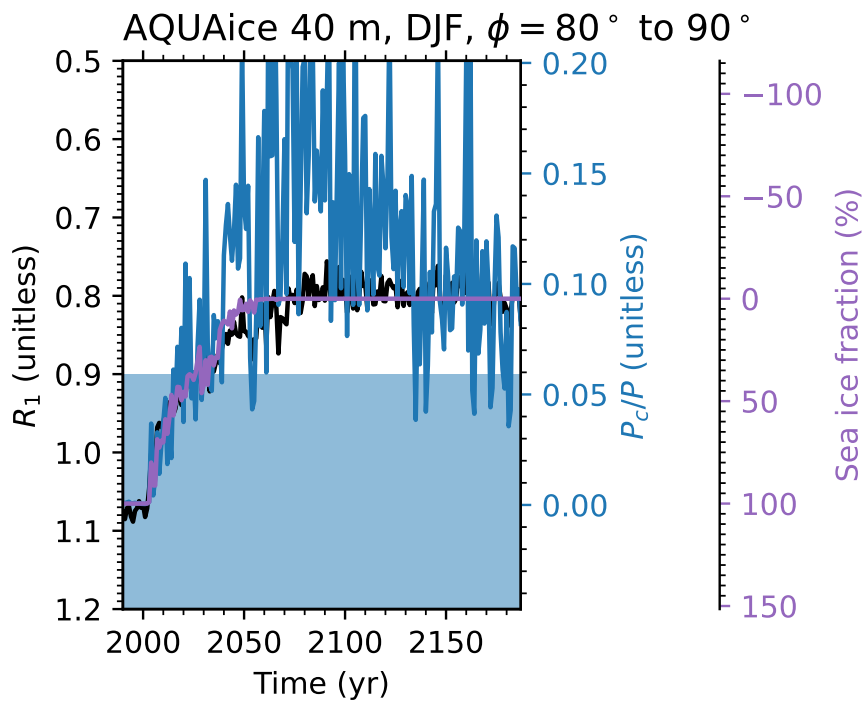
Figure 4.3.6: Same as Fig. 4.3.1 but for AQUAice.

86

(a)
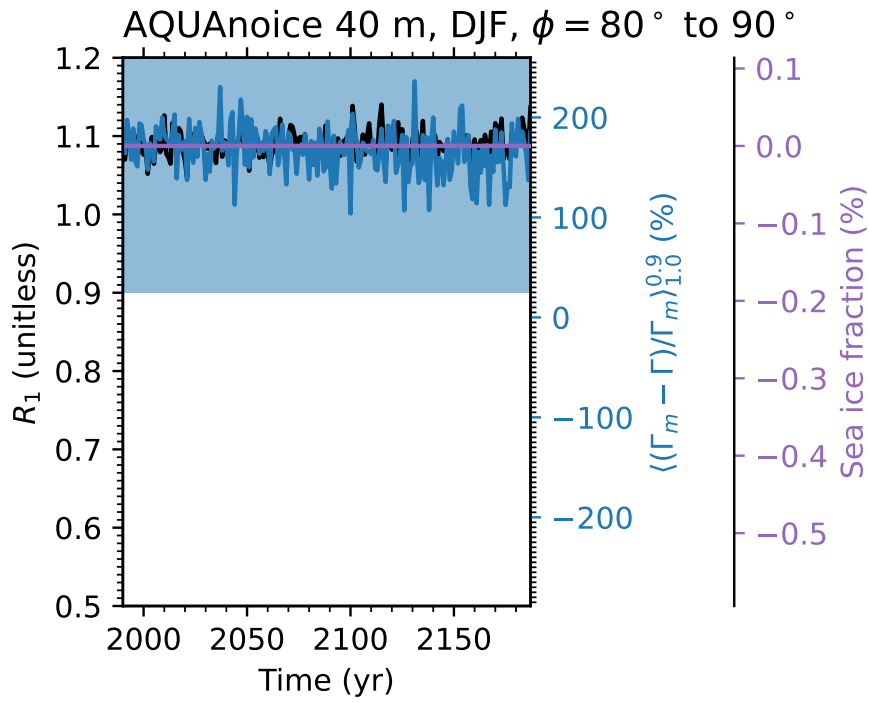
(b)
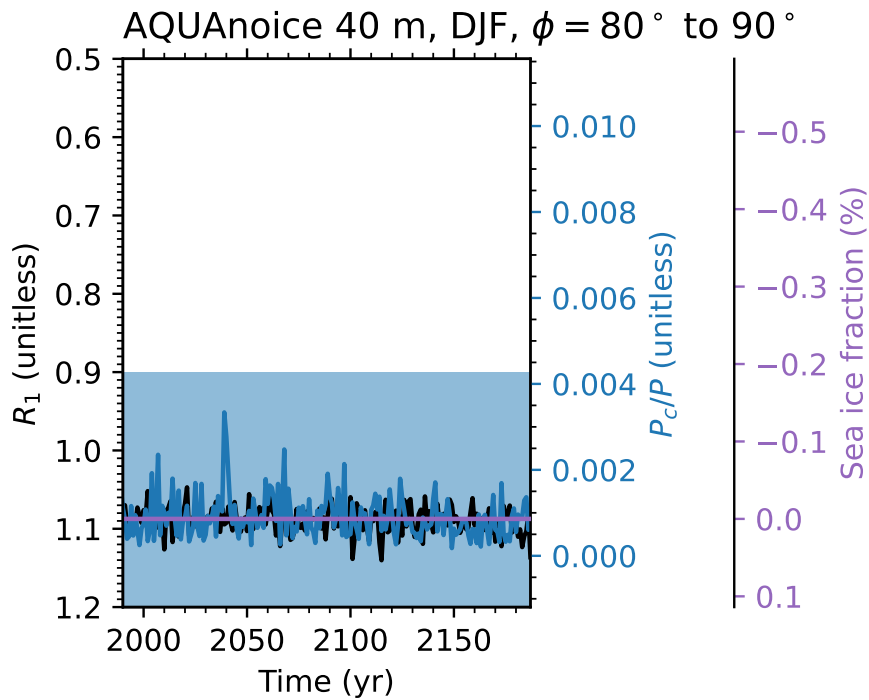
Figure 4.3.7: Same as Fig. 4.3.1 but for AQUAnoice.
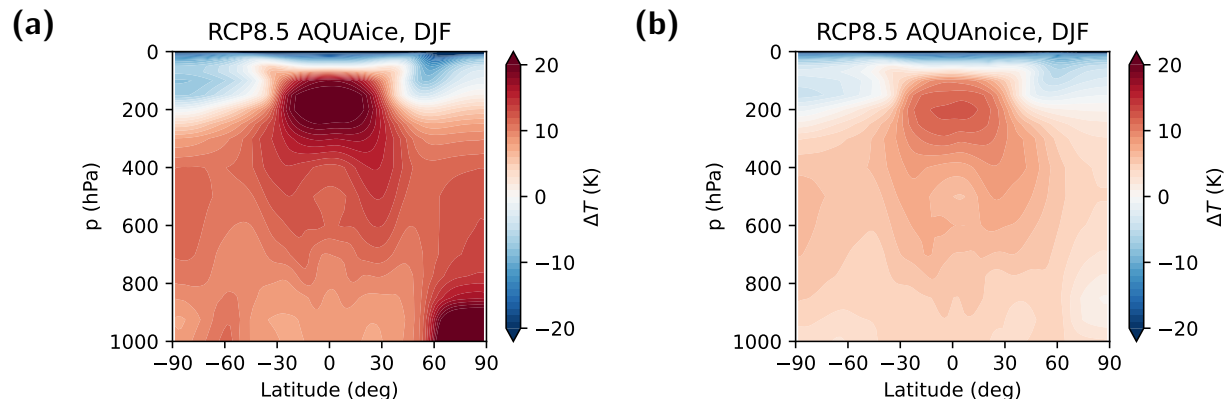
Figure 4.3.8: (a) The latitudinal and vertical warming response for the Northern Hemisphere winter season (DJF) for (a) AQUAice and (b) AQUAnoice. The warming response is computed as the difference between the temperature averaged over the last 20 years of the 200-year RCP8.5 run and the last 20 years of the control run. The contour interval is 1 K. Note that the climate is hemispherically symmetric in the aquaplanets: the asymmetry shown here is a seasonal asymmetry (surface-amplified polar warming is weak in the summer hemisphere).

response to the extended RCP8.5 emission scenario.

I used the energy balance framework to quantify the importance of two previously proposed mechanisms (enhanced radiative cooling and reduced advective heating) on the transient response to anthropogenic forcing. I linearly decomposed the R_1 response into contributions from changes in radiative cooling and advective heating. The decomposition showed that the regime transition is characterized by two phases. In the first phase (before 2100), the R_1 response is dominated by enhanced radiative cooling. Offline radiative transfer calculations showed enhanced radiative cooling largely follows from the clear-sky greenhouse effect of increased water vapor from warming assuming fixed relative humidity. In the second phase (after 2100), the R_1 response is dominated by reduced advective heating into the Arctic. The two-phased transition suggests that different mechanisms are important at different times, highlighting the importance of investigating the transient response of wintertime Arctic climate change.

I tested the hypothesis that sea-ice melting is a necessary condition for the regime transition using an aquaplanet configured with and without sea-ice melting. The aquaplanet with

sea-ice melting exhibits an Arctic regime transition including a time dependent response of radiative cooling and advective heating. The aquaplanet without sea-ice melting exhibits no change in R_1 and the wintertime Arctic remains in RAE. The absence of significant energy flux changes in the case without sea-ice melting is consistent with the key role that sea ice plays in the surface warming response.

4.4.2 Discussion

The results demonstrate that the response of the Arctic to anthropogenic forcing is a transient phenomenon involving time dependent mechanisms. This implies that historical records and near-term (up to 2100) projections of wintertime Arctic change do not reveal the full picture of the long-term (beyond 2100) response.

Quantifying the transient emergence of the new Arctic regime clarifies when assumptions applicable for the modern Arctic regime will break down. For example, I expect the temperature response predicted by the RAE model (Payne et al., 2015; Cronin and Jansen, 2016) to be valid for the Arctic prior to 2100 but fail thereafter when convective heating becomes important. The emergence of convective heating will also have implications on the energy hypothesis of the Arctic precipitation response (Pithan and Jung, 2021). A key ingredient of the energy hypothesis is that Arctic precipitation is constrained by free tropospheric radiative cooling only in the absence of surface turbulent fluxes. This assumption is a good one for the modern Arctic, which is in RAE and convective heating is negligibly small. However, the energy hypothesis will likely break down once the Arctic transitions to RCAE and wintertime convection emerges around the year 2100.

The mechanism-denial experiments support previous studies that show sea-ice melting plays an essential role in Arctic climate change (Screen and Simmonds, 2010; Boeke and Taylor, 2018; Dai et al., 2019; Shaw and Smith, 2022). However previous studies have also shown that Arctic Amplification occurs in the absence of sea-ice melting (Alexeev et al., 2005; Merlis and Henry, 2018; Previdi et al., 2020). Arctic Amplification can occur in

the absence of sea-ice melting because of an increase in poleward latent energy transport associated with moist air intrusions (Woods et al., 2013; Woods and Caballero, 2016; Pithan et al., 2018) and the nonlinear temperature depedence of the Clausius-Clapeyron relation (Manabe and Stouffer, 1980; Hwang et al., 2011; Shaw and Voigt, 2016; Graversen and Burtu, 2016; Yoshimori et al., 2017; Merlis and Henry, 2018; Feldl and Merlis, 2021). While the results do not preclude the importance of the latent energy transport on the Arctic warming response (latent energy transport increases but is shadowed by a decrease in dry static energy transport), I do not find Arctic Amplification in the absence of sea-ice melting here.

While the mechanism-denial experiment demonstrates that sea-ice melting is essential for both radiative and advective responses, additional experiments are necessary to understand the two-phased nature of the transient response. A fruitful avenue for future work may be to quantify the effect of sea-ice melting into 1) reduced sea-ice coverage (i.e., surface type changes from sea-ice covered to open ocean) and 2) reduced sea-ice thickness (i.e., surface remains covered in sea ice) due to their difference in modulating surface turbulent heat exchange (Taylor et al., 2022). The advective response emerges concurrently with the sea-ice fraction response, so one plausible hypothesis is that the advective response is connected to ice retreat (a change in surface type to open ocean) whereas the radiative response is connected to ice thinning (no change in surface type).

The Q-flux method introduced here isolates the effect of sea-ice melting without the effect of a time-varying surface forcing term (sea ice melts in AQUAice from radiative forcing alone). This has the advantage over methods used to control sea-ice melting such as the ghost flux (Alexeev et al., 2005) and nudging methods (Deser et al., 2015; McCusker et al., 2017; Sun et al., 2018), where a time varying surface forcing introduces spurious warming that overestimates the true warming contribution of sea-ice melting in response to radiative forcing (England et al., 2022). As imposing a Q flux is a simple and ubiquitous feature in climate models, the method introduced here may be of interest to the broader polar climate change community seeking to configure mechanism-denial experiments to isolate the effect

of sea-ice melting on climate change. For example, the abruptness of sea-ice loss on the transient response of the atmosphere can be tested by imposing a Q flux whose amplitude decreases year over year and controlling the rate of its decline.

4.A   Appendix A: Response in individual CMIP5 models

The RAE to RCAE regime transition occurs in all 7 CMIP5 models analyzed here (black lines in Fig. 4.A.1). Consistently wintertime sea ice melts and the surface inversion vanishes in all models (purple and blue lines in Fig. 4.A.1). Convective precipitation emerges in all models except for IPSL-CM5A-LR (blue lines in Fig. 4.A.2).

5 of the 7 CMIP5 models exhibit the two phases (radiative then advective) of the regime transition. The exceptions are HadGEM2-ES, where reduced advective heating dominates the full R_1 response, and IPSL-CM5A-LR, where enhanced radiative cooling dominates the full response.

The clear-sky longwave cooling response to anthropogenic forcing contributes to the enhanced radiative cooling response in all CMIP5 models (red lines in Fig. 4.A.4). RRTMG captures the clear-sky longwave cooling response in all CMIP5 models (compare black and red lines in Fig. 4.A.4). The enhanced greenhouse effect from warming and the associated moistening holding relative humidity fixed explains the clear-sky response in all CMIP5 models (orange lines in Fig. 4.A.5). Models do not agree on the sign of the cloudy-sky longwave cooling response (purple lines in Fig. 4.A.4).

4.B   Appendix B: Deriving a Q flux to capture the
thermodynamic effect of sea ice

The goal of imposing a Q flux in AQUAnoice is to capture the climatology of AQUAice in the absence of an interactive sea-ice module. To derive a Q flux (Q) that mimics the
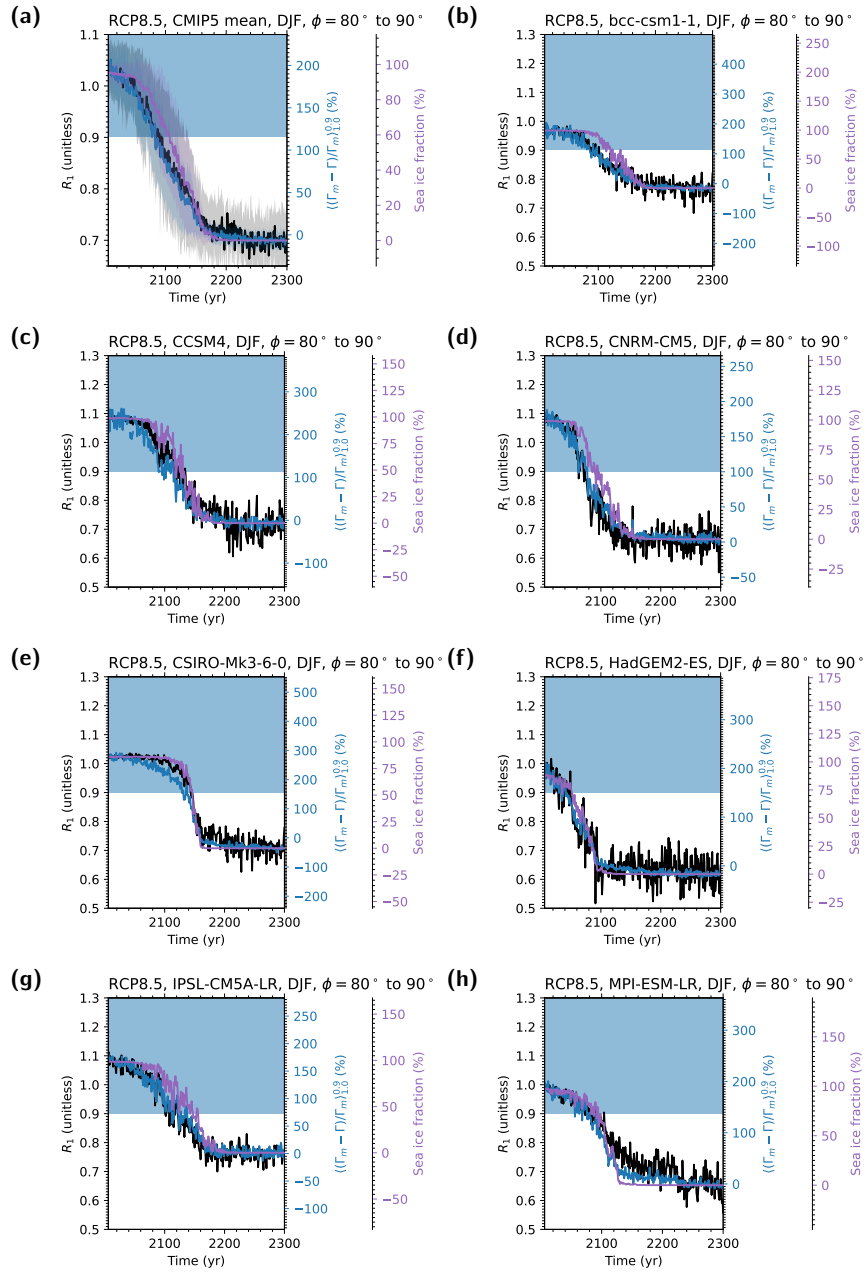
Figure 4.A.1: (a) Same as Fig. 4.3.1a but (b–h) for individual CMIP5 models.
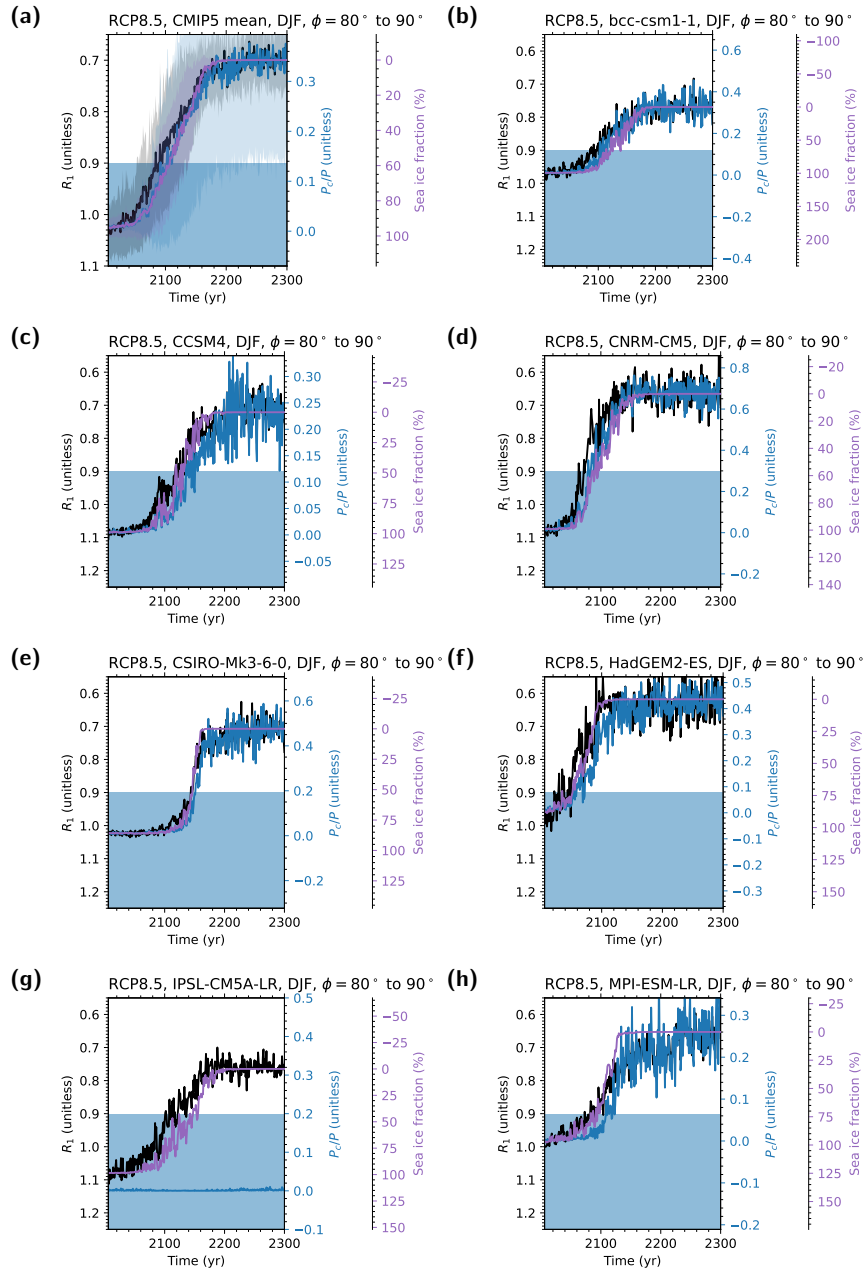
Figure 4.A.2: (a) Same as Fig. 4.3.1b but (b–h) for individual CMIP5 models.
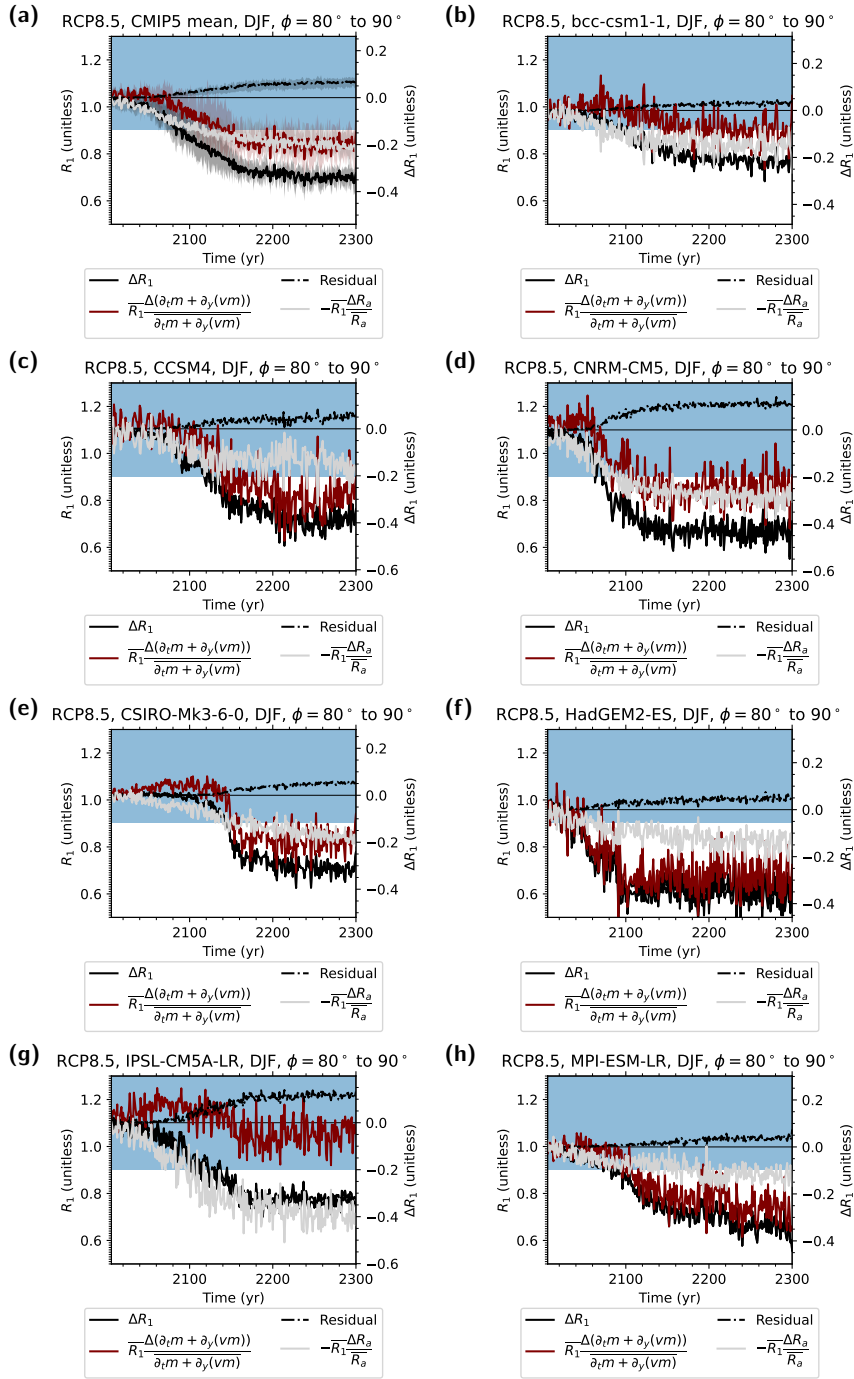
Figure 4.A.3: (a) Same as Fig. 4.3.2 but (b–h) for individual CMIP5 models.
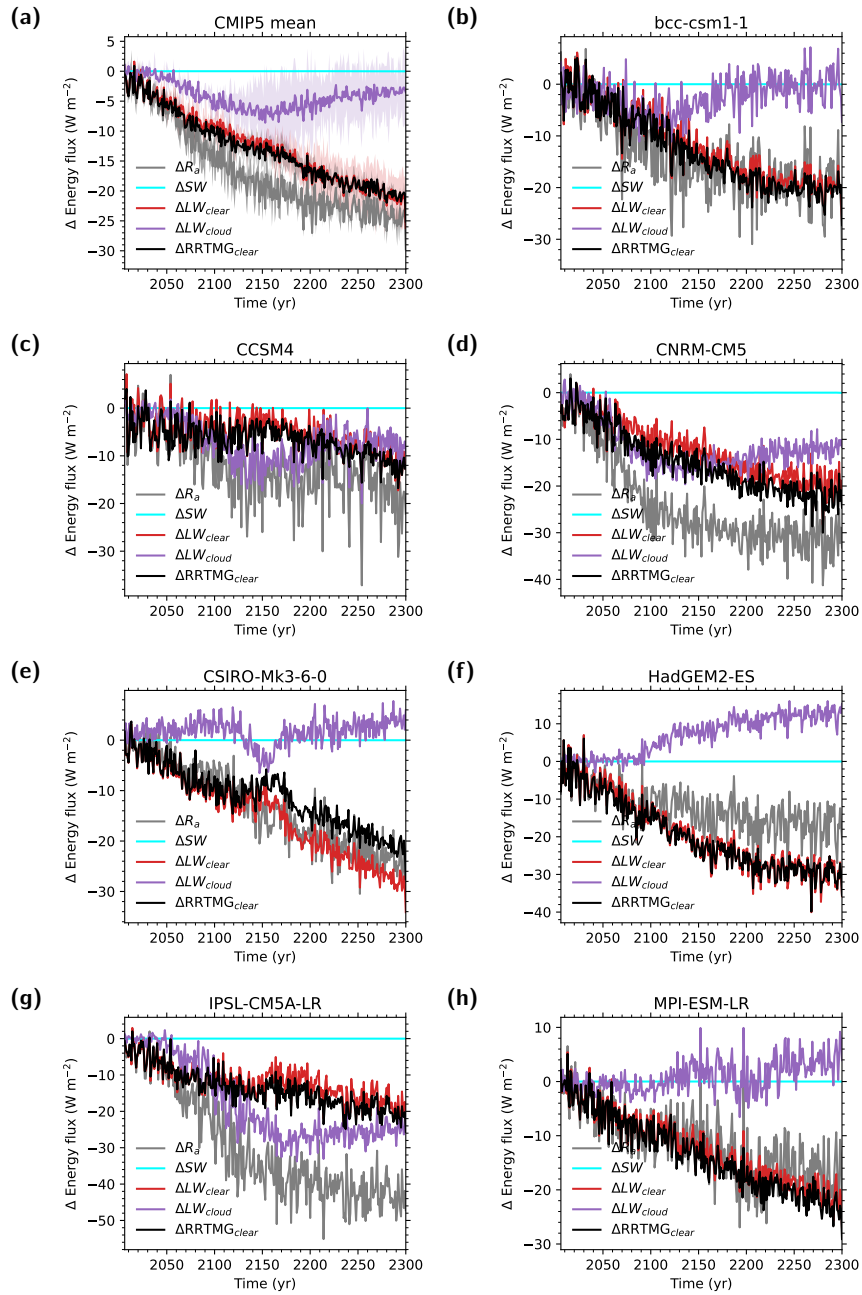
Figure 4.A.4: (a) Same as Fig. 4.3.3a but (b–h) for individual CMIP5 models.
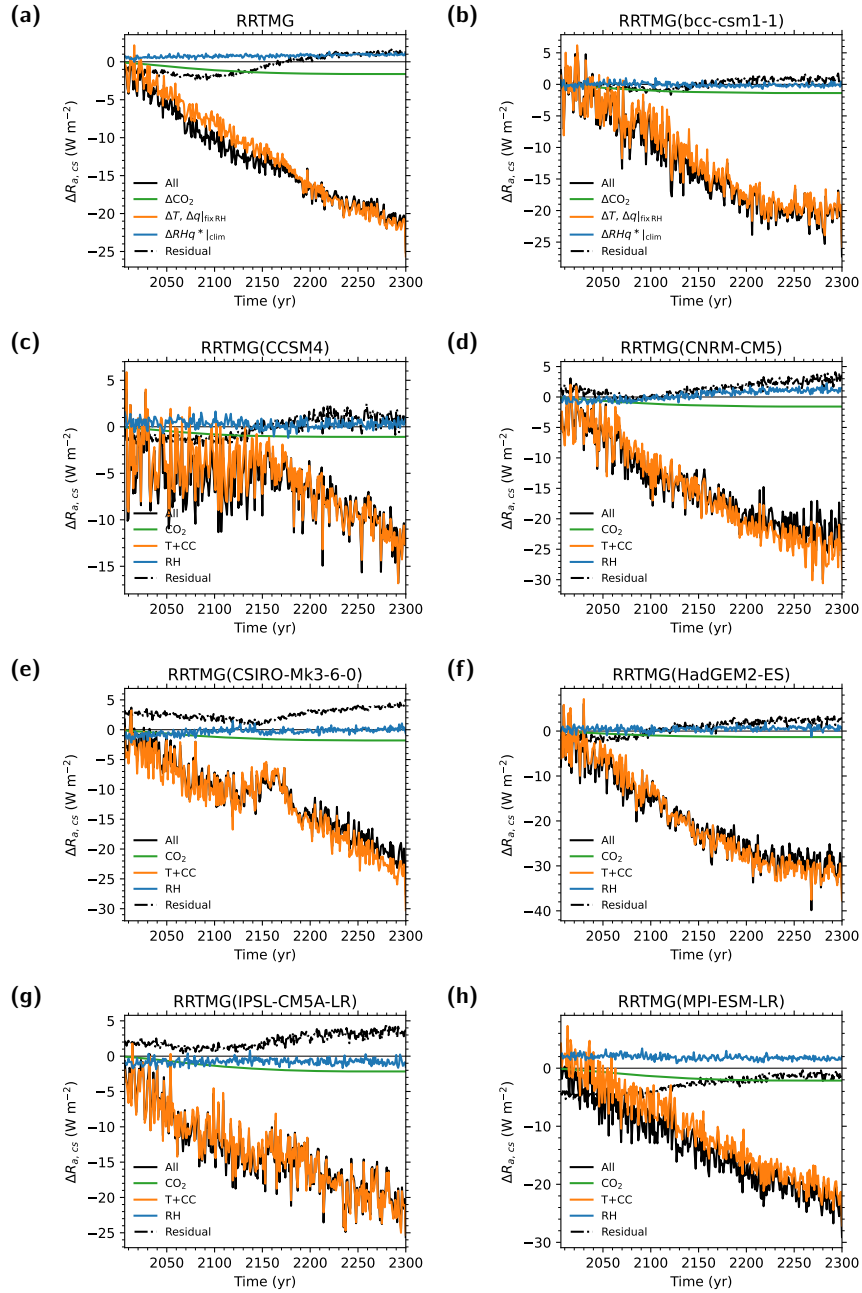
Figure 4.A.5: (a) Same as Fig. 4.3.3b but (b–h) for individual CMIP5 models.

thermodynamic effect of sea ice, consider the surface energy budget for AQUAnoice:

$$C^{ni}\frac{\partial T_s^{ni}}{\partial t} + Q = SW^{ni} + LW^{ni} + LH^{ni} + SH^{ni} = F_{SFC}^{ni}, \qquad (4.7)$$

and for AQUAice:

$$C^i\frac{\partial T_s^i}{\partial t} + F_{melt}^i + F_{cond}^i = SW^i + LW^i + LH^i + SH^i = F_{SFC}^i, \qquad (4.8)$$

where F_{SFC} is the net surface energy flux, F_{melt} is the energy flux associated with surface melting of snow or sea ice, F_{cond} is conductive flux through snow and sea ice, SW is the net surface shortwave flux, LW is the net surface longwave flux, LH is surface latent heat flux, SH is surface sensible heat flux, T_s is the surface temperature, and C is the surface heat capacity. The superscripts ni and i indicate the value is associated with AQUAnoice and AQUAice, respectively.

Subtracting equation (4.8) from (4.7), I obtain:

$$Q = C^i\frac{\partial T_s^i}{\partial t} + F_{melt}^i + F_{cond}^i - C^{ni}\frac{\partial T_s^{ni}}{\partial t} + SW^{ni} - SW^i + LW^{ni} - LW^i + LH^{ni} - LH^i + SH^{ni} - SH^i.$$

$$(4.9)$$

All quantities with a superscript ni are unknown because they emerge only after running the model with the imposed Q. To close this problem, I first express the statement that the climatology in AQUAnoice matches that of AQUAice by imposing variables determined by processes internal to the climate system are equal:

$$T_s^{ni} = T_s^i \qquad (4.10)$$

$$LW^{ni} = LW^i \qquad (4.11)$$

$$LH^{ni} = LH^i \qquad (4.12)$$

$$SH^{ni} = SH^i \qquad (4.13)$$

Substituting equation (4.10)–(4.13) into (4.9),

$$Q = \underbrace{C^i \frac{\partial T_s^i}{\partial t} + F_{melt}^i + F_{cond}^i - C^{ni} \frac{\partial T_s^i}{\partial t}}_{\text{surface heat capacity effect, } Q_C} + \underbrace{SW^{ni} - SW^i}_{\text{shortwave effect, } Q_{SW}} . \qquad (4.14)$$

The Q flux is composed of two distinct thermodynamic effects of sea ice. First, the smaller surface heat capacity of sea ice and the presence of melt and conductive fluxes amplify the seasonal cycle of surface temperature. Second, the higher surface albedo of sea ice compared to open ocean acts to cool the surface temperature year round. If I suppose that the surface albedo effect were the only important shortwave mechanism, equation (4.14) can be closed by setting

$$SW^{ni} = (1 - \alpha_O)SW_\downarrow^i, \qquad (4.15)$$

where $\alpha_O = 0.07$ is the surface albedo of open ocean and $SW_\downarrow^i$ is the downward shortwave flux in AQUAice. However, the surface albedo effect is not the only shortwave mechanism. Imposing Q_C leads to a higher downwelling shortwave flux in AQUAnoice compared to AQUAice. Thus, to determine SW^{ni} that includes both the surface albedo and the Q_C adjustment effect, I first run AQUAnoice with an imposed Q flux of Q_C only.

When AQUAnoice is imposed with a Q flux of Q_C, the resulting surface temperature tendency in AQUAnoice is comparable to that of AQUAice (compare blue and black lines in Fig. 4.B.4a). However, AQUAnoice with an imposed Q flux of Q_C alone is too warm in the annual mean because the shortwave effect of sea ice is not yet included (Fig. 4.B.5).

To account for the remaining difference in the climatology of AQUAice and AQUAnoice, I impose SW^{ni} such that it includes both the surface albedo and Q_C shortwave adjustment effect:

$$SW^{ni} = SW^{Q_C}, \qquad (4.16)$$

where SW^{Q_C} is the net surface shortwave flux for AQUAnoice with an imposed Q flux of Q_C. Since the surface albedo in AQUAnoice is everywhere that of open ocean, the surface
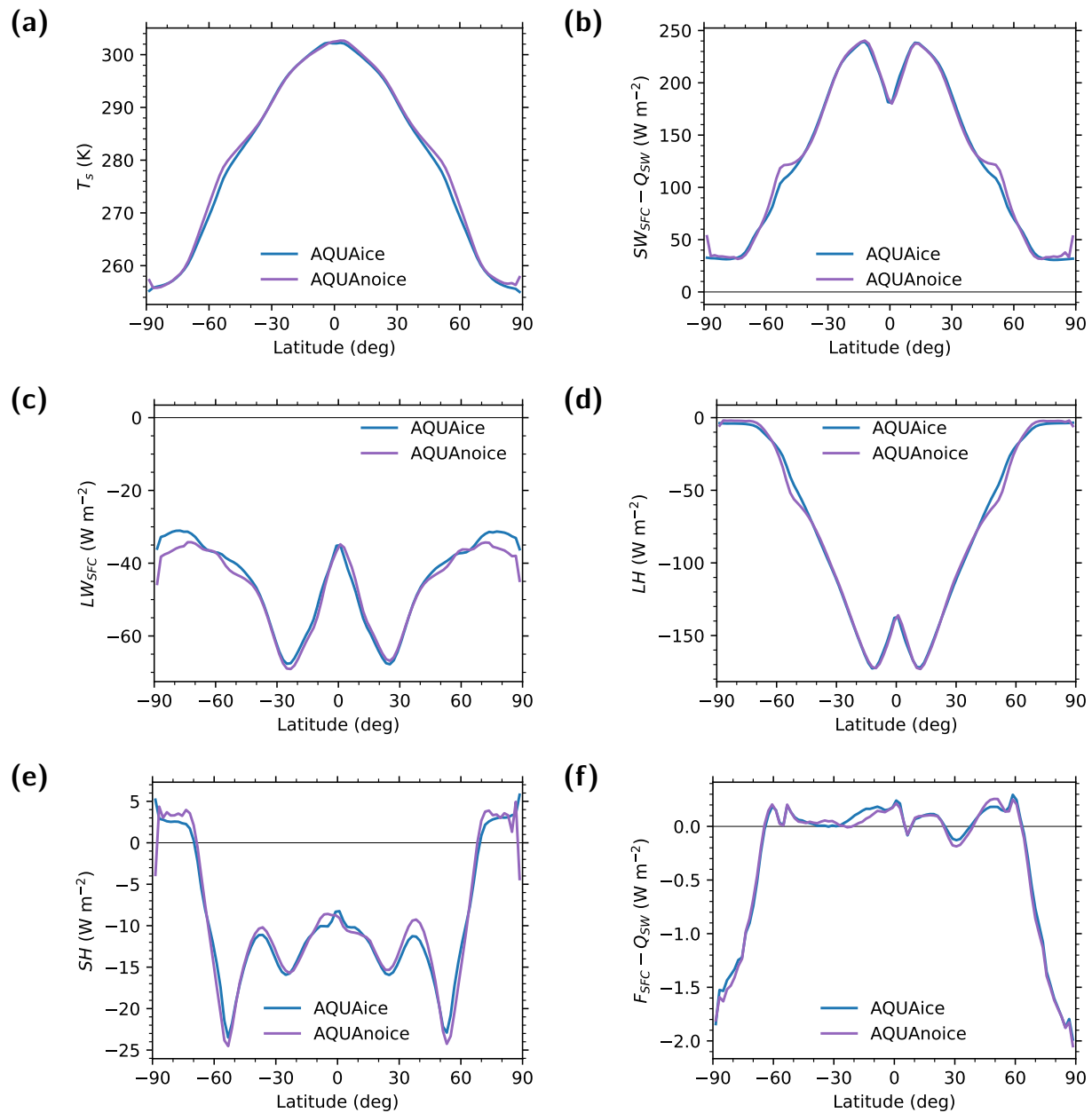
Figure 4.B.1: The annual and zonal mean (a) surface temperature, (b) net surface shortwave flux, (c) net surface longwave flux, (d) surface latent heating, (e) surface sensible heating, and (f) net surface heat flux for AQUAice (blue) and AQUAnoice (purple). A positive (negative) energy flux corresponds to a flux that heats (cools) the surface. Note that Q_{SW} is subtracted from AQUAnoice (b) net shortwave flux and (f) F_{SFC} to highlight the effect that Q_{SW} has in offsetting the difference between AQUAice and AQUAnoice shortwave flux.
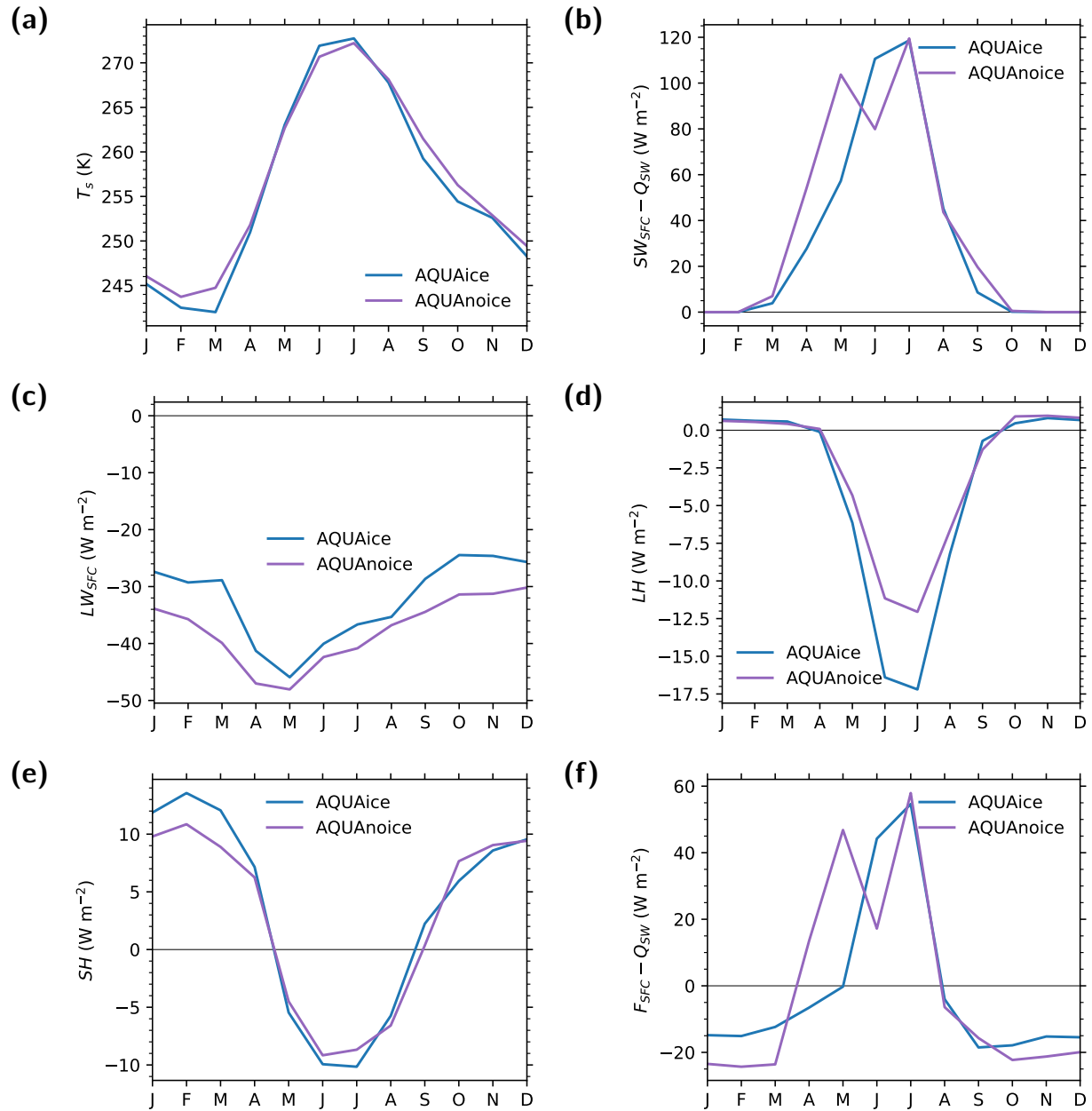
Figure 4.B.2: Same as Fig. 4.B.1 but for the seasonal cycle in the Arctic (80–90°N).
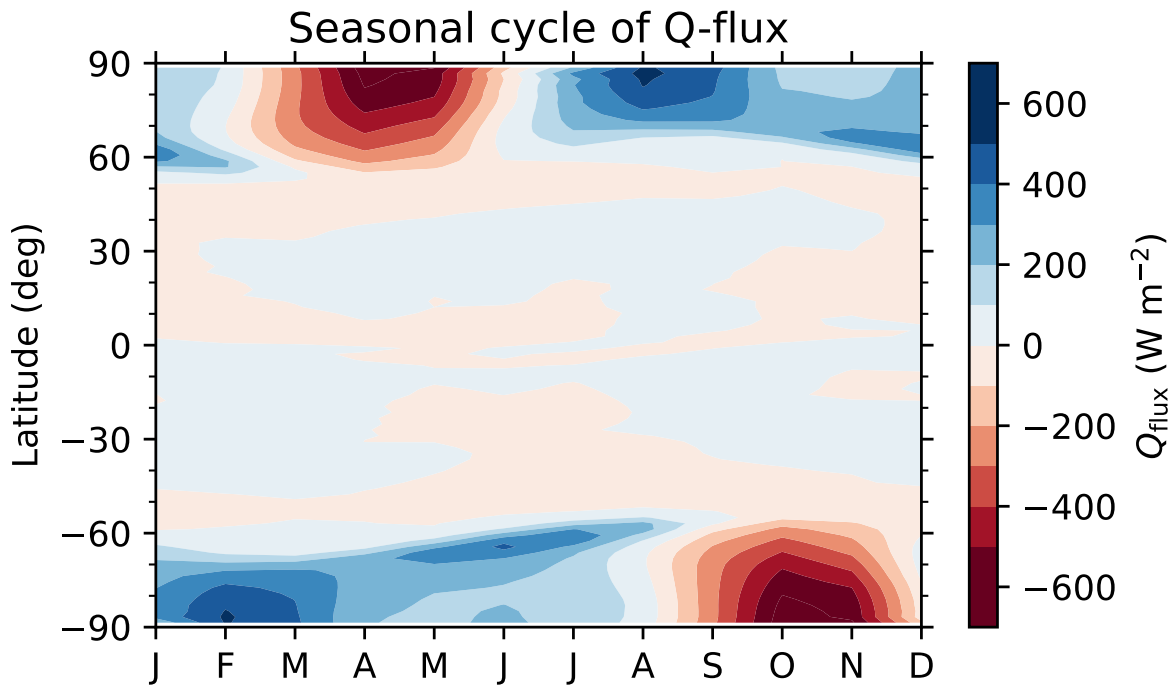
Figure 4.B.3: The latitudinal and seasonal structure of the full Q flux ($Q_C + Q_{SW}$). Positive values correspond to heat flux divergence, a cooling influence on the surface energy budget.

albedo effect is included in equation (4.16). Arctic temperature profiles in AQUAnoice with an imposed Q flux of $Q_C + Q_{SW}$ are consistent with the AQUAice climatology (compare blue and purple lines in Fig. 4.B.5 and 4.B.6).
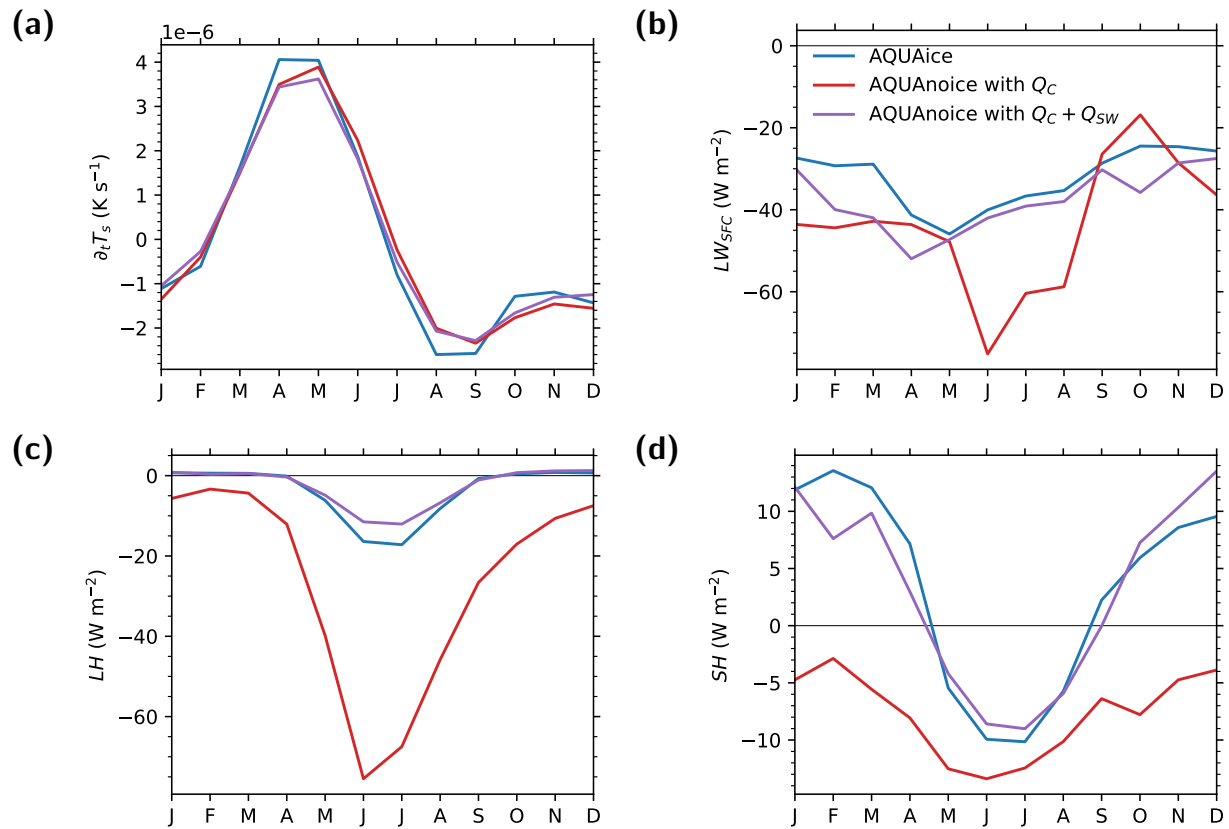
Figure 4.B.4: (a) Surface temperature tendency, (b) surface net longwave radiative flux, (c) surface latent heat flux, and (d) surface sensible heat flux for AQUAice (blue), AQUA with an imposed Q flux of Q_C (red), and AQUA with an imposed Q flux of $Q_C + Q_{SW}$ (purple).
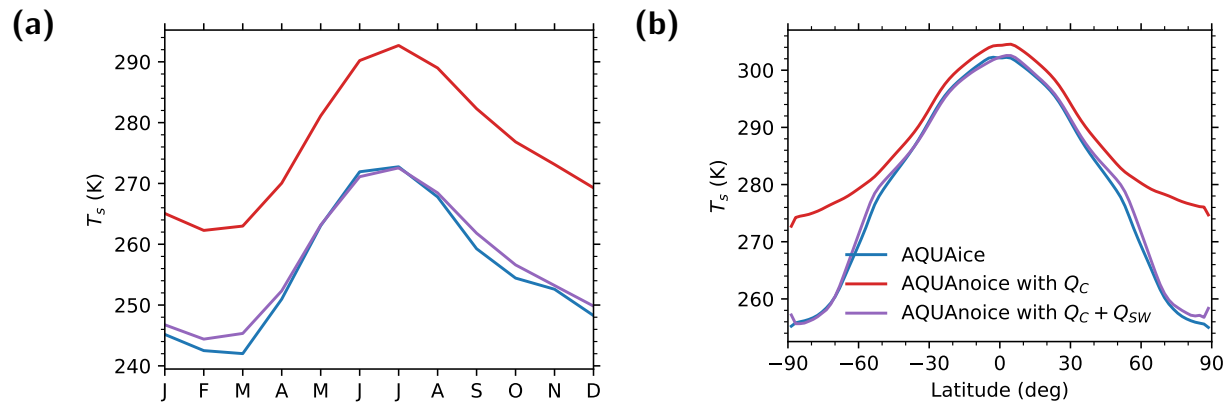
Figure 4.B.5: (a) The seasonal cycle of Arctic surface temperature and (b) the latitudinal structure of annual mean surface temperature for AQUAice (blue), AQUA with an imposed Q flux of Q_C (red), and AQUA with an imposed Q flux of $Q_C + Q_{SW}$ (purple).
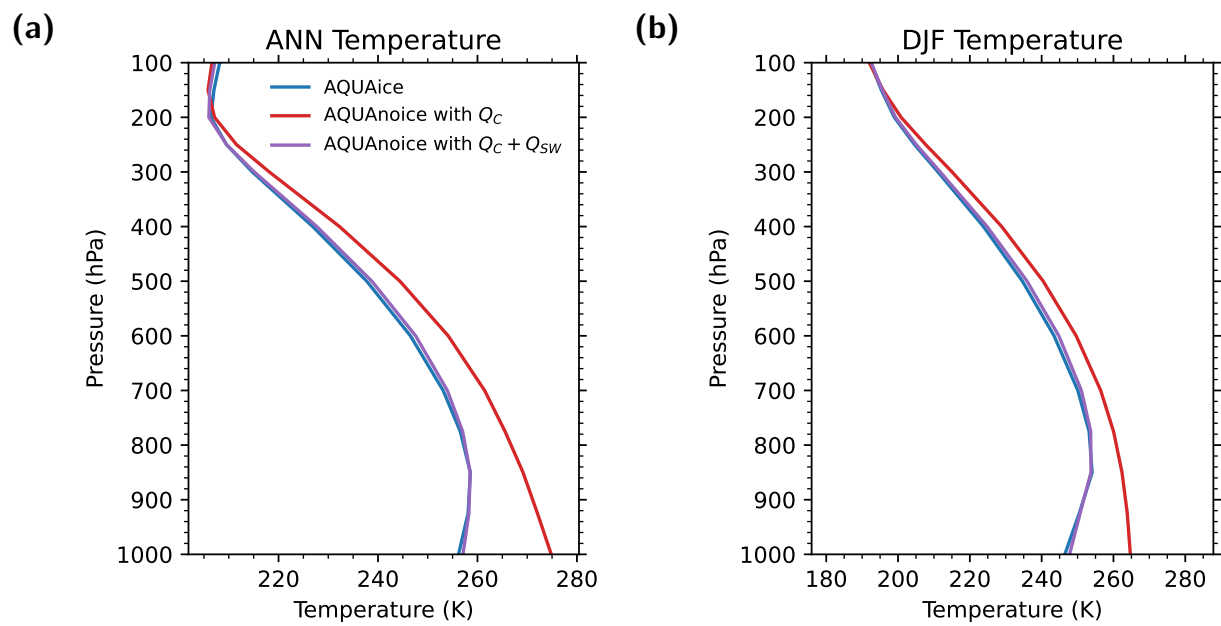
Figure 4.B.6: (a) The (a) annual mean (ANN) and (b) wintertime (DJF) Arctic vertical temperature profile for AQUAice (blue), AQUA with an imposed Q flux of Q_C (red), and AQUA with an imposed Q flux of $Q_C + Q_{SW}$ (purple).

CHAPTER 5

CONCLUSION

State-of-the-art climate models robustly project that the warming response to anthropogenic forcing will be amplified aloft in the tropics and at the surface at the poles. Conceptual models of the temperature profile of an atmospheric column provide the basis of our understanding of this warming response.

Conceptual models of the warming response are derived by making simplifying assumptions about the dominant energy fluxes that maintain the energy balance of an atmospheric column. Amplified warming aloft is predicted from moist convective adjustment, which comes from the assumption that the column energy balance is in Radiative-Convective Equilibrium (RCE). Amplified surface warming is predicted from a stable near-surface stratification, which comes from the assumption that the column energy balance is in Radiative-Advective Equilibrium (RAE).

For the insights obtained from RCE and RAE to be useful, we must verify that their predictions are consistent with state-of-the-art model projections for the right physical reasons. This thesis contributes to our understanding of Earth's temperature response to climate change by combining theory, idealized model simulations, and state-of-the-art model projections.

In Chapter 2, I used the column moist static energy framework to quantitatively diagnose where and when RCE and RAE hold in Earth's modern climate. RCE exists year round in the tropics and in the Northern midlatitudes during summertime. RAE exists year round over Antarctica and in the Arctic with the exception of early summer. The seasonal emergence of RCE in the Northern midlatitudes summertime and the vanishing of RAE in the Arctic early summer season were previously unknown, demonstrating the usefulness of a quantitative framework for diagnosing energy balance regimes. Lapse rates in RCE and RAE are qualitatively consistent with moist adiabatic and surface inversion lapse rates, respectively. To understand the physical mechanisms that control the existence of seasonal regime

transitions, I configured idealized model simulations (energy balance and aquaplanet). The results show the existence of seasonal energy balance and lapse rate regime transitions are controlled by surface heat capacity in the midlatitudes and sea ice in the high latitudes. Finally, I showed energy balance regimes in the modern climate provide a useful guide to the vertical structure of the warming response in the annual mean, and seasonally over the tropics and the Southern high latitudes.

In Chapter 3, I investigated the quantitative accuracy of the simplest convective adjustment scheme in RCE, moist adiabatic adjustment. Moist adiabatic adjustment overpredicts the multi-model mean 300 hPa temperature response in the tropics by 16.6–25.3% across the climate model hierarchy. Three mechanisms influence overprediction: surface heterogeneity, direct effect of increased CO_2, and convective entrainment. Accounting for the surface heterogeneity effect and the direct effect of CO_2 reduces the CMIP5 multi-model mean overprediction by 0.7–7.2% and 2.8–3.9% respectively, but does not eliminate it. To quantify the influence of entrainment, I varied the Tokioka parameter in aquaplanet simulations. When entrainment is decreased by decreasing the Tokioka parameter from 0.1 to 0, overprediction decreases by 9.6% and 10.4% with and without surface heterogeneity, respectively. The sensitivity of overprediction to the climatological entrainment rate in the aquaplanet mostly follows the predictions of simple entraining plume models. The results highlight the usefulness of simple entraining plume models for the tropical warming response because they offer a significant improvement in quantitative accuracy for a marginal increase in complexity over moist adiabatic adjustment.

In Chapter 4, I showed the modern wintertime Arctic climate, which is in a state of RAE, transitions to a new energy balance regime in response to anthropogenic forcing. The future energy balance regime of the wintertime Arctic is characterized by radiative cooling, convective heating, and advective heating, so-called Radiative-Convective-Advective Equilibrium (RCAE). The regime transition is associated with the following mechanisms: 1) enhanced radiative cooling from the present to 2100 and 2) decreased advective heating from 2100

onward. Decomposing the radiative cooling response in an offline radiative transfer model highlights the predominant importance of the enhanced water vapor greenhouse effect, which dominates over the direct effect of CO_2. Mechanism-denial experiments in an aquaplanet with and without sea-ice melting highlight the essential role of sea-ice melting in both the enhanced radiative cooling and decreased advective heating response. The results show transient Arctic climate change involves multiple mechanisms, suggesting that historical trends likely do not reveal the full picture of the long-term Arctic response.

The energy balance framework developed here has promising applications for climate research beyond the scope of this thesis. As the metric for quantifying energy balance regimes is a nondimensional number, it may be applicable for characterizing the temperature structure for past climates of Earth and exoplanets. Quantifying the zonal structure of energy balance regimes would be useful for exploring regional climate change. While energy balance regimes were linked to the emergence of convective precipitation in the wintertime Arctic, the link has not been investigated as a function of latitude and season more broadly. Last, while I focused on the response of the wintertime Arctic, the R_1 response over the Southern Ocean to anthropogenic forcing is comparable in magnitude but the underlying mechanism for this response is currently unknown. These are all exciting avenues for future research.

The findings of this thesis have improved our understanding of lapse rate regimes, their connection to energy balance regimes, and their response to warming. Thus, the work can be thought of as a synthesis of our understanding across the hierarchy of climate models, following the spirit of climate research advocated by Held (2005). Understanding gives us confidence in climate model projections and justifies advising policy makers on the impacts of climate change. This work also provides a useful framework for communicating climate change to the broader public because box models of energy balance are simple and intuitive to understand. Thus, the quantitative framework of energy balance regimes introduced in this thesis is an important addition to the toolkit for climate research and pedagogy.

References

Abbot, D. S., Huber, M., Bousquet, G., and Walker, C. C. (2009). High-CO2 cloud radiative forcing feedback over both land and ocean in a global climate model. *Geophysical Research Letters*, 36(5).

Abbot, D. S. and Tziperman, E. (2008a). A high-latitude convective cloud feedback and equable climates. *Quarterly Journal of the Royal Meteorological Society*, 134(630):165–185.

Abbot, D. S. and Tziperman, E. (2008b). Sea ice, high-latitude convection, and equable climates. *Geophysical Research Letters*, 35(3).

Alexeev, V. A., Langen, P. L., and Bates, J. R. (2005). Polar amplification of surface warming on an aquaplanet in "ghost forcing" experiments without sea ice feedbacks. *Climate Dynamics*, 24(7):655–666.

American Meteorological Society (2022). Moist-adiabatic lapse rate - Glossary of Meteorology. https://glossary.ametsoc.org/wiki/Reversible_moist-adiabatic_process.

Andreas, E. L., Paulson, C. A., William, R. M., Lindsay, R. W., and Businger, J. A. (1979). The turbulent heat flux from Arctic leads. *Boundary-Layer Meteorology*, 17(1):57–91.

Andrews, T. and Webb, M. J. (2018). The dependence of global cloud and lapse rate feedbacks on the spatial structure of tropical pacific warming. *Journal of Climate*, 31(2):641–654.

Armour, K. C., Siler, N., Donohoe, A., and Roe, G. H. (2019). Meridional Atmospheric Heat Transport Constrained by Energetics and Mediated by Large-Scale Diffusion. *Journal of Climate*, 32(12):3655–3680.

Arnold, N. P., Branson, M., Burt, M. A., Abbot, D. S., Kuang, Z., Randall, D. A., and Tziperman, E. (2014). Effects of explicit atmospheric convection at high CO2. *Proceedings of the National Academy of Sciences*, 111(30):10943–10948.

Barpanda, P. and Shaw, T. A. (2020). Surface Fluxes Modulate the Seasonality of Zonal-Mean Storm Tracks. *Journal of the Atmospheric Sciences*, 77(2):753–779.

Bengtsson, L., Hodges, K. I., Koumoutsaris, S., Zahn, M., and Keenlyside, N. (2011). The changing atmospheric water cycle in Polar Regions in a warmer climate. *Tellus A: Dynamic Meteorology and Oceanography*, 63(5):907–920.

Betts, A. K. (1982). Saturation Point Analysis of Moist Convective Overturning. *Journal of the Atmospheric Sciences*, 39(7):1484–1505.

Bintanja, R., Graversen, R. G., and Hazeleger, W. (2011). Arctic winter warming amplified by the thermal inversion and consequent low infrared cooling to space. *Nature Geoscience*, 4(11):758–761.

Bintanja, R. and Selten, F. M. (2014). Future increases in Arctic precipitation linked to local evaporation and sea-ice retreat. *Nature*, 509(7501):479–482.

Blackburn, M. and Hoskins, B. J. (2013). Context and Aims of the Aqua-Planet Experiment. *Journal of the Meteorological Society of Japan. Ser. II*, 91A:1–15.

Boeke, R. C. and Taylor, P. C. (2018). Seasonal energy exchange in sea ice retreat regions contributes to differences in projected Arctic warming. *Nature Communications*, 9(1):5017.

Bordoni, S. and Schneider, T. (2008). Monsoons as eddy-mediated regime transitions of the tropical overturning circulation. *Nature Geoscience*, 1(8):515–519.

Bradley, R. S., Keimig, F. T., and Diaz, H. F. (1992). Climatology of surface-based inversions in the North American Arctic. *Journal of Geophysical Research: Atmospheres*, 97(D14):15699–15712.

Chang, E. K. M., Lee, S., and Swanson, K. L. (2002). Storm Track Dynamics. *Journal of Climate*, 15(16):2163–2183.

Cronin, T. W. and Jansen, M. F. (2016). Analytic radiative-advective equilibrium as a model for high-latitude climate. *Geophysical Research Letters*, 43(1):449–457.

Dai, A., Luo, D., Song, M., and Liu, J. (2019). Arctic amplification is caused by sea-ice loss under increasing CO 2. *Nature Communications*, 10(1):121.

Deser, C., Tomas, R. A., and Sun, L. (2015). The Role of Ocean–Atmosphere Coupling in the Zonal-Mean Atmospheric Response to Arctic Sea Ice Loss. *Journal of Climate*, 28(6):2168–2186.

Devasthale, A., Willén, U., Karlsson, K.-G., and Jones, C. G. (2010). Quantifying the clear-sky temperature inversion frequency and strength over the Arctic Ocean during summer and winter seasons from AIRS profiles. *Atmospheric Chemistry and Physics*, 10(12):5565–5572.

Donohoe, A. and Battisti, D. S. (2013). The Seasonal Cycle of Atmospheric Heating and Temperature. *Journal of Climate*, 26(14):4962–4980.

Donohoe, A., Frierson, D. M. W., and Battisti, D. S. (2014). The effect of ocean mixed layer depth on climate in slab ocean aquaplanet experiments. *Climate Dynamics*, 43(3):1041–1055.

Emanuel, K. A. and Bister, M. (1996). Moist Convective Velocity and Buoyancy Scales. *Journal of the Atmospheric Sciences*, 53(22):3276–3285.

England, M. R., Eisenman, I., and Wagner, T. J. W. (2022). Spurious Climate Impacts in Coupled Sea Ice Loss Simulations. *Journal of Climate*, -1(aop):1–38.

Feldl, N. and Merlis, T. M. (2021). Polar Amplification in Idealized Climates: The Role of Ice, Moisture, and Seasons. *Geophysical Research Letters*, 48(17):e2021GL094130.

Feldl, N., Po-Chedley, S., Singh, H. K. A., Hay, S., and Kushner, P. J. (2020). Sea ice and atmospheric circulation shape the high-latitude lapse rate feedback. *npj Climate and Atmospheric Science*, 3(1):1–9.

Flannaghan, T., Fueglistaler, S., Held, I. M., Po-Chedley, S., Wyman, B., and Zhao, M. (2014). Tropical temperature trends in atmospheric general circulation model simulations and the impact of uncertainties in observed SSTs. *Journal of Geophysical Research: Atmospheres*, 119(23):13–327.

Fueglistaler, S., Radley, C., and Held, I. M. (2015). The distribution of precipitation and the spread in tropical upper tropospheric temperature trends in CMIP5/AMIP simulations. *Geophysical Research Letters*, 42(14):6000–6007.

Gates, W. L. (1992). An AMS continuing series: Global change–AMIP: The atmospheric model intercomparison project. *Bulletin of the American Meteorological Society*, 73(12):1962–1970.

Gelaro, R., McCarty, W., Suárez, M. J., Todling, R., Molod, A., Takacs, L., Randles, C. A., Darmenov, A., Bosilovich, M. G., Reichle, R., Wargan, K., Coy, L., Cullather, R., Draper, C., Akella, S., Buchard, V., Conaty, A., da Silva, A. M., Gu, W., Kim, G.-K., Koster, R., Lucchesi, R., Merkova, D., Nielsen, J. E., Partyka, G., Pawson, S., Putman, W., Rienecker, M., Schubert, S. D., Sienkiewicz, M., and Zhao, B. (2017). The Modern-Era Retrospective Analysis for Research and Applications, Version 2 (MERRA-2). *Journal of Climate*, 30(14):5419–5454.

Giorgetta, M. A., Roeckner, E., Mauritsen, T., Bader, J., Crueger, T., Esch, M., Rast, S., Kornblueh, L., Schmidt, H., Kinne, S., Hohenegger, C., Möbis, B., Krismer, T., Wieners, H., and Stevens, B. (2013). The atmospheric general circulation model ECHAM6: Model description. Reports on Earth System Science 135, Max Planck Institute, Hamburg, Germany.

Graham, R. M., Cohen, L., Ritzhaupt, N., Segger, B., Graversen, R. G., Rinke, A., Walden, V. P., Granskog, M. A., and Hudson, S. R. (2019). Evaluation of Six Atmospheric Reanalyses over Arctic Sea Ice from Winter to Early Summer. *Journal of Climate*, 32(14):4121–4143.

Graversen, R. G. and Burtu, M. (2016). Arctic amplification enhanced by latent energy transport of atmospheric planetary waves. *Quarterly Journal of the Royal Meteorological Society*, 142(698):2046–2054.

Hahn, L. C., Armour, K. C., Battisti, D. S., Donohoe, A., Pauling, A. G., and Bitz, C. M. (2020). Antarctic Elevation Drives Hemispheric Asymmetry in Polar Lapse Rate Climatology and Feedback. *Geophysical Research Letters*, 47(16):e2020GL088965.

Ham, Y.-G., Kug, J.-S., Kim, D., Kim, Y.-H., and Kim, D.-H. (2013). What controls phase-locking of ENSO to boreal winter in coupled GCMs? *Climate Dynamics*, 40(5):1551–1568.

Hankel, C. and Tziperman, E. (2021). The Role of Atmospheric Feedbacks in Abrupt Winter Arctic Sea-Ice Loss in Future Warming Scenarios. *Journal of Climate*, -1(aop):1–38.

Hartmann, D. (2016). *Global Physical Climatology*, volume 103. Elsevier, second edition.

He, J. and Soden, B. J. (2015). Anthropogenic weakening of the tropical circulation: The relative roles of direct CO_2 forcing and sea surface temperature change. *Journal of Climate*, 28(22):8728–8742.

Held, I. M. (1993). Large-Scale Dynamics and Global Warming. *Bulletin of the American Meteorological Society*, 74(2):228–242.

Held, I. M. (2000). The General Circulation of the Atmosphere. Technical report, Woods Hole Oceanographic Institution.

Held, I. M. (2005). The gap between simulation and understanding in climate modeling. *Bulletin of the American Meteorological Society*, 86(11):1609–1614.

Held, I. M. and Hou, A. Y. (1980). Nonlinear Axially Symmetric Circulations in a Nearly Inviscid Atmosphere. *Journal of the Atmospheric Sciences*, 37(3):515–533.

Hersbach, H., Bell, B., Berrisford, P., Hirahara, S., Horányi, A., Muñoz-Sabater, J., Nicolas, J., Peubey, C., Radu, R., Schepers, D., Simmons, A., Soci, C., Abdalla, S., Abellan, X., Balsamo, G., Bechtold, P., Biavati, G., Bidlot, J., Bonavita, M., Chiara, G. D., Dahlgren, P., Dee, D., Diamantakis, M., Dragani, R., Flemming, J., Forbes, R., Fuentes, M., Geer, A., Haimberger, L., Healy, S., Hogan, R. J., Hólm, E., Janisková, M., Keeley, S., Laloyaux, P., Lopez, P., Lupu, C., Radnoti, G., de Rosnay, P., Rozum, I., Vamborg, F., Villaume, S., and Thépaut, J.-N. (2020). The ERA5 global reanalysis. *Quarterly Journal of the Royal Meteorological Society*, 146(730):1999–2049.

Huber, M. and Sloan, L. C. (1999). Warm climate transitions: A general circulation modeling study of the Late Paleocene Thermal Maximum (∼56 Ma). *Journal of Geophysical Research: Atmospheres*, 104(D14):16633–16655.

Hwang, Y.-T., Frierson, D. M. W., and Kay, J. E. (2011). Coupling between Arctic feedbacks and changes in poleward energy transport. *Geophysical Research Letters*, 38(17).

Jakob, C., Singh, M. S., and Jungandreas, L. (2019). Radiative Convective Equilibrium and Organized Convection: An Observational Perspective. *Journal of Geophysical Research: Atmospheres*, 124(10):5418–5430.

Jang, Y.-S., Kim, D., Kim, Y.-H., Kim, D.-H., Watanabe, M., Jin, F.-F., and Kug, J.-S. (2013). Simulation of two types of El Niño from different convective parameters. *Asia-Pacific Journal of Atmospheric Sciences*, 49(2):193–199.

Jeevanjee, N. and Romps, D. M. (2018). Mean precipitation change from a deepening troposphere. *Proceedings of the National Academy of Sciences*, 115(45):11465–11470.

Kang, S. M., Held, I. M., Frierson, D. M. W., and Zhao, M. (2008). The Response of the ITCZ to Extratropical Thermal Forcing: Idealized Slab-Ocean Experiments with a GCM. *Journal of Climate*, 21(14):3521–3532.

Kim, D., Jang, Y.-S., Kim, D.-H., Kim, Y.-H., Watanabe, M., Jin, F.-F., and Kug, J.-S. (2011). El Niño–Southern Oscillation sensitivity to cumulus entrainment in a coupled general circulation model. *Journal of Geophysical Research: Atmospheres*, 116(D22).

Kobayashi, S., Ota, Y., Harada, Y., Ebita, A., Moriya, M., Onoda, H., Onogi, K., Kamahori, H., Kobayashi, C., Endo, H., Miyaoka, K., and Takahashi, K. (2015). The JRA-55 Reanalysis: General Specifications and Basic Characteristics. *Journal of the Meteorological Society of Japan. Ser. II*, 93(1):5–48.

Korty, R. L. and Schneider, T. (2007). A Climatology of the Tropospheric Thermal Stratification Using Saturation Potential Vorticity. *Journal of Climate*, 20(24):5977–5991.

Landrum, L. and Holland, M. M. (2020). Extremes become routine in an emerging new Arctic. *Nature Climate Change*, 10(12):1108–1115.

Lin, Y., Zhao, M., Ming, Y., Golaz, J.-C., Donner, L. J., Klein, S. A., Ramaswamy, V., and Xie, S. (2013). Precipitation Partitioning, Tropical Clouds, and Intraseasonal Variability in GFDL AM2. *Journal of Climate*, 26(15):5453–5466.

Manabe, S. and Stouffer, R. J. (1980). Sensitivity of a global climate model to an increase of CO_2 concentration in the atmosphere. *Journal of Geophysical Research: Oceans*, 85(C10):5529–5554.

Manabe, S. and Strickler, R. F. (1964). Thermal Equilibrium of the Atmosphere with a Convective Adjustment. *Journal of the Atmospheric Sciences*, 21(4):361–385.

Manabe, S. and Wetherald, R. T. (1975). The Effects of Doubling the CO_2 Concentration on the climate of a General Circulation Model. *Journal of the Atmospheric Sciences*, 32(1):3–15.

Maykut, G. A. (1982). Large-scale heat exchange and ice production in the central Arctic. *Journal of Geophysical Research: Oceans*, 87(C10):7971–7984.

McCusker, K. E., Kushner, P. J., Fyfe, J. C., Sigmond, M., Kharin, V. V., and Bitz, C. M. (2017). Remarkable separability of circulation response to Arctic sea ice loss and greenhouse gas forcing. *Geophysical Research Letters*, 44(15):7955–7964.

Meinshausen, M., Smith, S. J., Calvin, K., Daniel, J. S., Kainuma, M. L. T., Lamarque, J.-F., Matsumoto, K., Montzka, S. A., Raper, S. C. B., Riahi, K., Thomson, A., Velders, G. J. M., and van Vuuren, D. P. (2011). The RCP greenhouse gas concentrations and their extensions from 1765 to 2300. *Climatic Change*, 109(1):213.

Merlis, T. M. and Held, I. M. (2019). Aquaplanet Simulations of Tropical Cyclones. *Current Climate Change Reports*, 5(3):185–195.

Merlis, T. M. and Henry, M. (2018). Simple Estimates of Polar Amplification in Moist Diffusive Energy Balance Models. *Journal of Climate*, 31(15):5811–5824.

Miyawaki, O., Shaw, T. A., and Jansen, M. F. (2022). Quantifying Energy Balance Regimes in the Modern Climate, Their Link to Lapse Rate Regimes, and Their Response to Warming. *Journal of Climate*, 35(3):1045–1061.

Miyawaki, O., Tan, Z., Shaw, T. A., and Jansen, M. F. (2020). Quantifying Key Mechanisms That Contribute to the Deviation of the Tropical Warming Profile From a Moist Adiabat. *Geophysical Research Letters*, 47(20):e2020GL089136.

Mlawer, E. J., Taubman, S. J., Brown, P. D., Iacono, M. J., and Clough, S. A. (1997). Radiative transfer for inhomogeneous atmospheres: RRTM, a validated correlated-k model for the longwave. *Journal of Geophysical Research: Atmospheres*, 102(D14):16663–16682.

Moorthi, S. and Suarez, M. J. (1992). Relaxed Arakawa-Schubert. a parameterization of moist convection for general circulation models. *Monthly Weather Review*, 120(6):978–1002.

Nakamura, N. and Oort, A. H. (1988). Atmospheric heat budgets of the polar regions. *Journal of Geophysical Research: Atmospheres*, 93(D8):9510–9524.

Neale, R. B. and Hoskins, B. J. (2000). A standard test for AGCMs including their physical parametrizations: I: The proposal. *Atmospheric Science Letters*, 1(2):101–107.

Neelin, J. D. and Held, I. M. (1987). Modeling Tropical Convergence Based on the Moist Static Energy Budget. *Monthly Weather Review*, 115(1):3–12.

Nilsson, J. and Emanuel, K. A. (1999). Equilibrium atmospheres of a two-column radiative-convective model. *Quarterly Journal of the Royal Meteorological Society*, 125(558):2239–2264.

Payne, A. E., Jansen, M. F., and Cronin, T. W. (2015). Conceptual model analysis of the influence of temperature feedbacks on polar amplification. *Geophysical Research Letters*, 42(21):9561–9570.

Pendergrass, A. G., Reed, K. A., and Medeiros, B. (2016). The link between extreme precipitation and convective organization in a warming climate: Global radiative-convective equilibrium simulations. *Geophysical Research Letters*, 43(21):11,445–11,452.

Pierrehumbert, R. T. (2005). Climate dynamics of a hard snowball Earth. *Journal of Geophysical Research: Atmospheres*, 110(D1).

Pierrehumbert, R. T. (2011). Infrared Radiation and Planetary Temperature. *AIP Conference Proceedings*, 1401(1):232–244.

Pithan, F. and Jung, T. (2021). Arctic Amplification of Precipitation Changes—The Energy Hypothesis. *Geophysical Research Letters*, 48(21):e2021GL094977.

Pithan, F. and Mauritsen, T. (2014). Arctic amplification dominated by temperature feedbacks in contemporary climate models. *Nature Geoscience*, 7(3):181–184.

Pithan, F., Svensson, G., Caballero, R., Chechin, D., Cronin, T. W., Ekman, A. M. L., Neggers, R., Shupe, M. D., Solomon, A., Tjernström, M., and Wendisch, M. (2018). Role of air-mass transformations in exchange between the Arctic and mid-latitudes. *Nature Geoscience*, 11(11):805–812.

Po-Chedley, S., Proistosescu, C., Armour, K. C., and Santer, B. D. (2018). Climate constraint reflects forced signal. *Nature*, 563(7729):E6–E9.

Po-Chedley, S., Zelinka, M. D., Jeevanjee, N., Thorsen, T. J., and Santer, B. D. (2019). Climatology explains intermodel spread in tropical upper tropospheric cloud and relative humidity response to greenhouse warming. *Geophysical Research Letters*, 46(22):13399–13409.

Popke, D., Stevens, B., and Voigt, A. (2013). Climate and climate change in a radiative-convective equilibrium version of ECHAM6. *Journal of Advances in Modeling Earth Systems*, 5(1):1–14.

Porter, D. F., Cassano, J. J., Serreze, M. C., and Kindig, D. N. (2010). New estimates of the large-scale Arctic atmospheric energy budget. *Journal of Geophysical Research: Atmospheres*, 115(D8).

Previdi, M., Janoski, T. P., Chiodo, G., Smith, K. L., and Polvani, L. M. (2020). Arctic Amplification: A Rapid Response to Radiative Forcing. *Geophysical Research Letters*, 47(17):e2020GL089933.

Price, E., Mielikainen, J., Huang, M., Huang, B., Huang, H.-L. A., and Lee, T. (2014). GPU-Accelerated Longwave Radiation Scheme of the Rapid Radiative Transfer Model for General Circulation Models (RRTMG). *IEEE Journal of Selected Topics in Applied Earth Observations and Remote Sensing*, 7(8):3660–3667.

Riehl, H. and Malkus, J. S. (1958). On the heat balance of the equatorial trough zone. *Geophysica*, 6(3-4).

Roberts, C. D., Palmer, M. D., Allan, R. P., Desbruyeres, D. G., Hyder, P., Liu, C., and Smith, D. (2017). Surface flux and ocean heat transport convergence contributions to seasonal and interannual variations of ocean heat content. *Journal of Geophysical Research: Oceans*, 122(1):726–744.

Romps, D. M. (2010). A direct measure of entrainment. *Journal of the Atmospheric Sciences*, 67(6):1908–1927.

Romps, D. M. (2011). Response of Tropical Precipitation to Global Warming. *Journal of the Atmospheric Sciences*, 68(1):123–138.

Romps, D. M. (2014). An analytical model for tropical relative humidity. *Journal of Climate*, 27(19):7432–7449.

Romps, D. M. (2016). Clausius–Clapeyron Scaling of CAPE from Analytical Solutions to RCE. *Journal of the Atmospheric Sciences*, 73(9):3719–3737.

Romps, D. M., Seeley, J. T., Vollaro, D., and Molinari, J. (2014). Projected increase in lightning strikes in the United States due to global warming. *Science*, 346(6211):851–854.

Rose, B. E. J. (2018). CLIMLAB: A Python toolkit for interactive, process-oriented climate modeling. *Journal of Open Source Software*, 3(24):659.

Rose, B. E. J., Cronin, T. W., and Bitz, C. M. (2017). Ice Caps and Ice Belts: The Effects of Obliquity on Ice-Albedo Feedback. *The Astrophysical Journal*, 846(1):28.

Ruman, C. J., Monahan, A. H., and Sushama, L. (2022). Climatology of Arctic temperature inversions in current and future climates. *Theoretical and Applied Climatology*.

Salameh, J., Popp, M., and Marotzke, J. (2018). The role of sea-ice albedo in the climate of slowly rotating aquaplanets. *Climate Dynamics*, 50(7):2395–2410.

Schneider, T. (2006). The General Circulation of the Atmosphere. *Annual Review of Earth and Planetary Sciences*, 34(1):655–688.

Screen, J. A. and Simmonds, I. (2010). Increasing fall-winter energy loss from the Arctic Ocean and its role in Arctic temperature amplification. *Geophysical Research Letters*, 37(16).

Seeley, J. T. and Romps, D. M. (2015). The Effect of Global Warming on Severe Thunderstorms in the United States. *Journal of Climate*, 28(6):2443–2458.

Semtner, A. J. (1976). A Model for the Thermodynamic Growth of Sea Ice in Numerical Investigations of Climate. *Journal of Physical Oceanography*, 6(3):379–389.

Shaw, T. A., Baldwin, M., Barnes, E. A., Caballero, R., Garfinkel, C. I., Hwang, Y.-T., Li, C., O'Gorman, P. A., Rivière, G., Simpson, I. R., and Voigt, A. (2016). Storm track processes and the opposing influences of climate change. *Nature Geoscience*, 9(9):656–664.

Shaw, T. A. and Graham, R. J. (2020). Hydrological Cycle Changes Explain Weak Snowball Earth Storm Track Despite Increased Surface Baroclinicity. *Geophysical Research Letters*, 47(20):e2020GL089866.

Shaw, T. A. and Smith, Z. (2022). The Midlatitude Response to Polar Sea Ice Loss: Idealized Slab-Ocean Aquaplanet Experiments with Thermodynamic Sea Ice. *Journal of Climate*, 35(8):2633–2649.

Shaw, T. A. and Voigt, A. (2016). What can moist thermodynamics tell us about circulation shifts in response to uniform warming? *Geophysical Research Letters*, 43(9):4566–4575.

Sherwood, S. C., Bony, S., and Dufresne, J.-L. (2014). Spread in model climate sensitivity traced to atmospheric convective mixing. *Nature*, 505(7481):37–42.

Singh, M. S. and O'Gorman, P. A. (2013). Influence of entrainment on the thermal stratification in simulations of radiative-convective equilibrium: ENTRAINMENT AND THERMAL STRATIFICATION. *Geophysical Research Letters*, 40(16):4398–4403.

Singh, M. S. and O'Gorman, P. A. (2015). Increases in moist-convective updraught velocities with warming in radiative-convective equilibrium. *Quarterly Journal of the Royal Meteorological Society*, 141(692):2828–2838.

Sobel, A. H., Held, I. M., and Bretherton, C. S. (2002). The ENSO Signal in Tropical Tropospheric Temperature. *Journal of Climate*, 15(18):2702–2706.

Stevens, B., Giorgetta, M., Esch, M., Mauritsen, T., Crueger, T., Rast, S., Salzmann, M., Schmidt, H., Bader, J., Block, K., Brokopf, R., Fast, I., Kinne, S., Kornblueh, L., Lohmann, U., Pincus, R., Reichler, T., and Roeckner, E. (2013). Atmospheric component of the MPI-M Earth System Model: ECHAM6. *Journal of Advances in Modeling Earth Systems*, 5(2):146–172.

Stone, P. H. and Carlson, J. H. (1979). Atmospheric Lapse Rate Regimes and Their Parameterization. *Journal of the Atmospheric Sciences*, 36(3):415–423.

Sun, L., Alexander, M., and Deser, C. (2018). Evolution of the Global Coupled Climate Response to Arctic Sea Ice Loss during 1990–2090 and Its Contribution to Climate Change. *Journal of Climate*, 31(19):7823–7843.

Tan, Z., Lachmy, O., and Shaw, T. A. (2019). The sensitivity of the jet stream response to climate change to radiative assumptions. *Journal of Advances in Modeling Earth Systems*, 11(4):934–956.

Tastula, E.-M., Vihma, T., Andreas, E. L., and Galperin, B. (2013). Validation of the diurnal cycles in atmospheric reanalyses over Antarctic sea ice. *Journal of Geophysical Research: Atmospheres*, 118(10):4194–4204.

Taylor, K. E., Stouffer, R. J., and Meehl, G. A. (2012). An Overview of CMIP5 and the Experiment Design. *Bulletin of the American Meteorological Society*, 93(4):485–498.

Taylor, P. C., Boeke, R. C., Boisvert, L. N., Feldl, N., Henry, M., Huang, Y., Langen, P. L., Liu, W., Pithan, F., Sejas, S. A., and Tan, I. (2022). Process Drivers, Inter-Model Spread, and the Path Forward: A Review of Amplified Arctic Warming. *Frontiers in Earth Science*, 9.

Taylor, P. C., Hegyi, B. M., Boeke, R. C., and Boisvert, L. N. (2018). On the Increasing Importance of Air-Sea Exchanges in a Thawing Arctic: A Review. *Atmosphere*, 9(2):41.

Tjernström, M. and Graversen, R. G. (2009). The vertical structure of the lower Arctic troposphere analysed from observations and the ERA-40 reanalysis. *Quarterly Journal of the Royal Meteorological Society*, 135(639):431–443.

Tokioka, T., Yamazaki, K., Kitoh, A., and Ose, T. (1988). The equatorial 30-60 day oscillation and the Arakawa-Schubert penetrative cumulus parameterization. *Journal of the Meteorological Society of Japan. Ser. II*, 66(6):883–901.

Tripati, A. K. et al. (2014). Modern and glacial tropical snowlines controlled by sea surface temperature and atmospheric mixing. *Nature Geoscience*, 7(3):205.

Vallis, G. K., Zurita-Gotor, P., Cairns, C., and Kidston, J. (2015). Response of the large-scale structure of the atmosphere to global warming. *Quarterly Journal of the Royal Meteorological Society*, 141(690):1479–1501.

Wang, Y. and Huang, Y. (2020). Understanding the atmospheric temperature adjustment to CO_2 perturbation at the process level. *Journal of Climate*, 33(3):787–803.

Warren, R. A., Singh, M. S., and Jakob, C. (2020). Simulations of Radiative-Convective-Dynamical Equilibrium. *Journal of Advances in Modeling Earth Systems*, 12(3):e2019MS001734.

Williams, E. and Renno, N. (1993). An Analysis of the Conditional Instability of the Tropical Atmosphere. *Monthly Weather Review*, 121(1):21–36.

Wing, A. A., Emanuel, K., Holloway, C. E., and Muller, C. (2018a). Convective Self-Aggregation in Numerical Simulations: A Review. In Pincus, R., Winker, D., Bony, S., and Stevens, B., editors, *Shallow Clouds, Water Vapor, Circulation, and Climate Sensitivity*, Space Sciences Series of ISSI, pages 1–25. Springer International Publishing, Cham.

Wing, A. A., Reed, K. A., Satoh, M., Stevens, B., Bony, S., and Ohno, T. (2018b). Radiative–convective equilibrium model intercomparison project. *Geoscientific Model Development*, 11(2):793–813.

Woods, C. and Caballero, R. (2016). The Role of Moist Intrusions in Winter Arctic Warming and Sea Ice Decline. *Journal of Climate*, 29(12):4473–4485.

Woods, C., Caballero, R., and Svensson, G. (2013). Large-scale circulation associated with moisture intrusions into the Arctic during winter. *Geophysical Research Letters*, 40(17):4717–4721.

Xu, K.-M. and Emanuel, K. A. (1989). Is the Tropical Atmosphere Conditionally Unstable? *Monthly Weather Review*, 117(7):1471–1479.

Yoshimori, M., Abe-Ouchi, A., and Laîné, A. (2017). The role of atmospheric heat transport and regional feedbacks in the Arctic warming at equilibrium. *Climate Dynamics*, 49(9):3457–3472.

Zhang, Y. and Stone, P. H. (2011). Baroclinic Adjustment in an Atmosphere–Ocean Thermally Coupled Model: The Role of the Boundary Layer Processes. *Journal of the Atmospheric Sciences*, 68(11):2710–2730.

Zhou, W. and Xie, S. P. (2019). A conceptual spectral plume model for understanding tropical temperature profile and convective updraft velocities. *Journal of the Atmospheric Sciences*, 76(9):2801–2814.